NASA/TP-20240002199

Goldstone Radar Measurements of the Orbital Debris Environment: 2020-2021

Orbital Debris Program Office

Jessica A. Arnold
Jacobs – Jacobs JETS Contract

James Murray, Ph.D.
Tomorrow.io

Melissa Murray
Craig Technologies, KBR IMOC III

Mark Matney, Ph.D.
Timothy Kennedy, Ph.D.
NASA Johnson Space Center

February 2024

NASA STI Program Report Series

The NASA STI Program collects, organizes, provides for archiving, and disseminates NASA's STI. The NASA STI program provides access to the NTRS Registered and its public interface, the NASA Technical Reports Server, thus providing one of the largest collections of aeronautical and space science STI in the world. Results are published in both non-NASA channels and by NASA in the NASA STI Report Series, which includes the following report types:

- TECHNICAL PUBLICATION. Reports of completed research or a major significant phase of research that present the results of NASA Programs and include extensive data or theoretical analysis. Includes compilations of significant scientific and technical data and information deemed to be of continuing reference value. NASA counterpart of peer-reviewed formal professional papers but has less stringent limitations on manuscript length and extent of graphic presentations.

- TECHNICAL MEMORANDUM. Scientific and technical findings that are preliminary or of specialized interest, e.g., quick release reports, working papers, and bibliographies that contain minimal annotation. Does not contain extensive analysis.

- CONTRACTOR REPORT. Scientific and technical findings by NASA-sponsored contractors and grantees.

- CONFERENCE PUBLICATION. Collected papers from scientific and technical conferences, symposia, seminars, or other meetings sponsored or co-sponsored by NASA.

- SPECIAL PUBLICATION. Scientific, technical, or historical information from NASA programs, projects, and missions, often concerned with subjects having substantial public interest.

- TECHNICAL TRANSLATION. English-language translations of foreign scientific and technical material pertinent to NASA's mission.

Specialized services also include organizing and publishing research results, distributing specialized research announcements and feeds, providing information desk and personal search support, and enabling data exchange services.

For more information about the NASA STI program, see the following:

- Access the NASA STI program home page at http://www.sti.nasa.gov

- Help desk contact information:

https://www.sti.nasa.gov/sti-contact-form/
and select the "General" help request type.

NASA/TP-20240002199

Goldstone Radar Measurements of the Orbital Debris Environment: 2020-2021

Orbital Debris Program Office

Jessica A. Arnold
Jacobs – Jacobs JETS Contract

James Murray, Ph.D.
Tomorrow.io

Melissa Murray
Craig Technologies, KBR IMOC III

Mark Matney, Ph.D.
Timothy Kennedy, Ph.D.
NASA Johnson Space Center

National Aeronautics and
Space Administration

Johnson Space Center
Houston, Texas 77058

February 2024

ACKNOWLEDGEMENTS

The authors would like to thank Joseph Jao of the NASA Jet Propulsion Laboratory (JPL) for preliminary processing of the data and efforts towards diagnosing problems with the Goldstone system. Additionally, the authors would like to thank Heather Cowardin and Alyssa Manis for reviewing the technical content of this report. We would like to thank Debra Shoots and Ashley Johnson for their invaluable editing contributions. The cloud modeling, observation planning, and data collection for the Cosmos 1408 anti-satellite test required tremendous effort from everyone in the Radar Measurements and Modeling groups, respectively, at the NASA Orbital Debris Program Office, as well as colleagues at the Massachusetts Institute of Technology's Lincoln Laboratory and the JPL. The authors are thankful to all those involved.

This report is available in electronic form at
http://ntrs.nasa.gov/citations/20240002199

TABLE OF CONTENTS

SECTION **PAGE**

1.0 Introduction 11
1.1 Purpose 11
1.2 Scope 11
1.3 Overview 11
2.0 Radar System Overview 12
2.1 Radar Performance 14
3.0 Data Collection and Radar Processing 16
3.1 JPL Data Collection and Processing 16
3.2 ODPO Processing and Data Quality 17
3.2.1 NASA Beam Gain Correction 17
3.2.2 Range and Range-Rate Residuals 19
3.2.3 Doppler Sign Consistency 21
3.2.4 Radio Frequency Interference Inspection 22
3.2.5 JPL Reported Range, RCS calculation, and Beam Overlap Correction 23
3.2.6 RCS Quantization Correction 25
3.3 Standard Chart Examination 26
3.4 The Size Estimation Model 29
4.0 Results 32
4.1 Radar Measurement Plots 33
4.1.1 Range versus Range-Rate and Altitude versus Doppler Inclination 33
4.1.1 Range versus RCS and Orbit Altitude versus SEM Size 35
4.1.2 Polarization Distribution 36
4.2 Environment Characterization Summary 37
4.2.1 SEM-Size Cumulative Distribution 37
4.2.2 Flux versus Altitude 38
4.2.3 Flux versus Inclination 39
4.2.4 HUSIR Comparisons 40
4.3 Special Datasets 42
4.3.1 DSS-13/DSS-28 Experimental data 42
4.3.1.1 Ad-Hoc Uniform RCS Calibration Estimation 45
4.3.2 Cosmos 1408 ASAT 47
5.0 Summary 52
6.0 References 53

Appendix A: Goldstone Radar Geometries Observation Plan 55
Appendix B: Range and Range-rate Residual Determination 73
Appendix C: CY2020- 2021 Pointing A 74
Appendix D: CY2020–2021, Pointing B 78
Appendix E: CY2020–2021, Pointing C 82
Appendix F: CY2020–2021, Pointing D 86
Appendix G: CY2020–2021, 800 km 90
Appendix H: SNR-Weighted Range Estimator 94

FIGURES

FIGURE **PAGE**

Figure 2-1. System transmit power history for Goldstone DSS-14 from CY2020–2021. 15
Figure 2-2. System temperature history for Goldstone DSS-25 and DSS-26 from CY2020–2021. 15
Figure 2-3. Orbit altitude versus SEM size of CY20-21 data with 99% completeness curve overlaid (black dotted line). 16
Figure 3-1. Geometry of the beam shape correction factor model calculation. 18
Figure 3-2. An example of the beam shape correction factor as a function of range from the transmitter for the DSS-14/DSS-25 transmitter/receiver pair in the D pointing. 19
Figure 3-3. Plot of range residuals to SNR residuals for CY2020–2021 data provided by JPL. 20
Figure 3-4. Plot of range-rate residuals to SNR residuals for CY2020–2021 data provided by JPL. 20
Figure 3-5. Range versus range-rate of a CY2021 observation overlaid on CY2016 data, illustrating the mirroring effect of the Doppler sign inconsistency. 21
Figure 3-6. Exemplar range-rate versus DOY scatterplot for the HUSIR 75E CY2018 dataset. 23
Figure 3-7. Range-rate versus DOY for the Goldstone CY2020–2021 dataset. 23
Figure 3-8. Geometry for bistatic range and boresight angle offset calculation. 25
Figure 3-9. Example total RCS versus range scatterplot for CY2016 Goldstone data illustrating the RCS quantization effect for low RCS objects. 26
Figure 3-10. Polarization distribution of 19 June 2021 observation compared to CY2016 data. 27
Figure 3-11. Polarization distribution of 12 October 2021 observation compared to CY2016 data. 27
Figure 3-12. Cumulative count rate versus SEM-size for 2 August 2021 observation compared to CY2016 data. 28
Figure 3-13. Cumulative count rate versus SEM-size for 3 November 2021 observation compared to CY2016 data. 29
Figure 3-14. Illustration of body and projected measurement on complex shape used in finding characteristic length. 30
Figure 3-15. Results of RCS-to-size measurements on 39 representative debris objects (red +). 31
Figure 3-16. NASA SEM (blue) and JPL SEM (orange), plotted with the sphere scattering curve (green). 32
Figure 4-1. Bistatic radar geometry. 33
Figure 4-2. Range versus range-rate plot for Goldstone CY2020–CY2021. 34
Figure 4-3. Orbit altitude versus average Doppler inclination for Goldstone CY2020–2021. 34
Figure 4-4. Range versus total RCS for Goldstone CY2020–2021. 35
Figure 4-5. Orbit altitude versus SEM size for Goldstone CY2020–2021. 36
Figure 4-6. Count rate versus Polarization for CY2020–2021, limited to the beam overlap altitudes of the B pointing and sizes larger. 37
Figure 4-7. The cumulative count rate versus SEM size between Goldstone CY2016, CY2017, and CY2020–2021, at the A, B, C, and D pointings. 38
Figure 4-8. The flux versus orbit altitude between Goldstone CY2016, CY2017, and CY2020–2021, at the A, B, C, and D pointings. 39
Figure 4-9. Flux versus average Doppler inclination between Goldstone CY2016, CY2017, and CY2020–2021, at the A, B, C, and D pointings. 40

Figure 4-10. The cumulative flux versus SEM size comparisons for HUSIR CY2021 and Goldstone CY2020–2021 datasets in all pointings. 41
Figure 4-11. Peak gain product versus altitude for the DSS-14/DSS-15, DSS-14/DSS-25 (A, B, C, D), and DSS-13/DSS-28 antenna pairs. 42
Figure 4-12. Flux versus SEM size HUSIR CY2020 and Goldstone CY2020 comparison. 44
Figure 4-13. Flux versus altitude HUSIR CY2020 and Goldstone CY2020 comparison. 45
Figure 4-14. Flux versus average Doppler inclination for HUSIR CY2020 and Goldstone CY2020. 45
Figure 4-15. Flux versus SEM size in incremented dB calibration constants for Goldstone CY2020, compared to HUSIR CY2020 data. 46
Figure 4-16. Normalized peak gain product of DSS-14 and DSS-25 versus altitude illustrating the bistatic beam overlap. 48
Figure 4-17. Predicted range-time distribution, as detected by Goldstone, of Cosmos 1408 fragments for a candidate observation on DOY 346, ... 49
Figure 4-18. Cumulative count rate versus corrected SEM size comparison for Goldstone CY2016–2017 and CY2021 ASAT special observation campaign. 50
Figure 4-19. Flux versus altitude comparison for Goldstone CY2016–2017 and CY2021 ASAT special observation campaign. 51
Figure 4-20. Flux versus average Doppler inclination for Goldstone CY2016–2017 and CY2021 ASAT special observation campaign. 51
Figure A-1. Cumulative surface area flux versus altitude bound between 5.62 mm and 1 cm. 56
Figure A-2. Cumulative surface area flux versus orbit altitude, bound between 5.62 cm and 1 cm, for Goldstone CY2018-A and HUSIR CY2018 data. 57
Figure A-3. Cumulative surface area flux versus orbit altitude, bound between 5.62 cm and 1 cm, for the first observation of Goldstone CY2018-A with Goldstone CY2016 data overlaid. 58
Figure A-4. Cumulative surface area flux versus orbit altitude, bound between 5.62 cm and 1 cm, for the first 2 observations of Goldstone CY2018-A with Goldstone CY2016 data overlaid. 59
Figure A-5. Cumulative surface area flux versus orbit altitude, bound between 5.62 cm and 1 cm, for the first 3 observations of Goldstone CY2018-A with Goldstone CY2016 data overlaid. 59
Figure A-6. Peak gain versus orbit altitude showing the number of pointings needed to cover all of LEO where the altitude coverage of a single pointing is defined by a constant offset in peak gain of 6 dB. 61
Figure A-7. Peak gain versus orbit altitude showing the number of pointings required to cover all of LEO where the altitude coverage of a single pointing is defined by a constant offset in peak gain of 3 dB. 61
Figure A-8. Peak gain versus orbit altitude showing the number of pointings required to cover all of LEO where the altitude coverage of a single pointing is defined by a constant offset in peak gain of 1 dB. 62
Figure A-9. Peak gain curves centered at 400 km altitude for various transmitter elevations with FSPL relative to 75E included. 63
Figure A-10. Peak gain curves centered at 1000 km altitude for various transmitter elevations with FSPL relative to 75E included. 63

Figure A-11. Peak gain curves centered at 400 km altitude for east and south staring pointings at 75° elevation. 64
Figure A-12. Peak gain curves centered at 400 km altitude for east and south staring pointings at 60° elevation. 65
Figure A-13. Pointings required to cover 700 km to 1000 km in altitude, where the altitude coverage of a single pointing is defined by its intersection with the historical peak gain curve with no offset, ... 66
Figure A-14. Pointings needed to cover 700 km to 1000 km in altitude, where the altitude coverage of a single pointing is defined by its intersection with the historical peak gain curve with a 1.5 dB offset, ... 67
Figure A-15. Orbit altitude versus SEM size of Goldstone CY2016 with historical completeness curve (dashed black curve) and the completeness curves of each of the chosen pointings. 68
Figure A-16. DSS-25, pointing A 69
Figure A-17. DSS-26, pointing A 69
Figure A-18. DSS-25, pointing B 70
Figure A-19. DSS-26, pointing B 70
Figure A-20. DSS-25, pointing C 71
Figure A-21. DSS-26, pointing C 71
Figure A-22. DSS-25, pointing D 72
Figure A-23. DSS-26, pointing D 72
Figure B-1. Flow diagram of range and range-rate residual process. 73
Figure C-1. Range versus range-rate of Goldstone CY2020–2021, pointing A. 74
Figure C-2. Range versus total RCS of Goldstone CY2020–2021, pointing A. 74
Figure C-3. Orbit altitude versus average Doppler inclination of Goldstone CY2020–2021, pointing A. 75
Figure C-4. Flux versus orbit altitude of Goldstone CY2020–2021, pointing A. 75
Figure C-5. Flux versus average Doppler inclination of Goldstone CY2020–2021, pointing A. 76
Figure C-6. Cumulative count rate versus PP SNR of Goldstone CY2020–2021, pointing A. 76
Figure C-7. Count rate versus polarization of Goldstone CY2020–2021, pointing A. 77
Figure C-8. Cumulative count rate versus SEM size of Goldstone CY2020–2021, pointing A. 77
Figure D-1. Range versus range-rate of Goldstone CY2020–2021, pointing B. 78
Figure D-2. Range versus total RCS of Goldstone CY2020–2021, pointing B. 78
Figure D-3. Orbit altitude versus average Doppler inclination of Goldstone CY2020–2021, pointing B. 79
Figure D-4. Flux versus orbit altitude of Goldstone CY2020–2021, pointing B. 79
Figure D-5. Flux versus average Doppler inclination of Goldstone CY2020–2021, pointing B. 80
Figure D-6. Cumulative count rate versus PP SNR of Goldstone CY2020–2021, pointing B. 80
Figure D-7. Count rate versus polarization of Goldstone CY2020–2021, pointing B. 81
Figure D-8. Cumulative count rate versus SEM size of Goldstone CY2020–2021, pointing B. 81
Figure E-1. Range versus range-rate of Goldstone CY2020–2021, pointing C. 82
Figure E-2. Range versus total RCS of Goldstone CY2020–2021, pointing C. 82

Figure E-3. Orbit altitude versus average Doppler inclination of Goldstone CY2020–2021, pointing C. 83
Figure E-4. Flux versus orbit altitude of Goldstone CY2020–2021, pointing C. 83
Figure E-5. Flux versus average Doppler inclination of Goldstone CY2020–2021, pointing C. 84
Figure E-6. Cumulative count rate versus PP SNR of Goldstone CY2020–2021, pointing C. 84
Figure E-7. Count rate versus polarization of Goldstone CY2020–2021, pointing C. 85
Figure E-8. Cumulative count rate versus SEM size of Goldstone CY2020–2021, pointing C. 85
Figure F-1. Range versus range-rate of Goldstone CY2020–2021, pointing D. 86
Figure F-2. Range versus total RCS of Goldstone CY2020–2021, pointing D. 86
Figure F-3. Orbit altitude versus average Doppler inclination of Goldstone CY2020–2021, pointing D. 87
Figure F-4. Flux versus orbit altitude of Goldstone CY2020–2021, pointing D. 87
Figure F-5. Flux versus average Doppler inclination of Goldstone CY2020–2021, pointing D. 88
Figure F-6. Cumulative count rate versus PP SNR of Goldstone CY2020–2021, pointing D. 88
Figure F-7. Count rate versus polarization of Goldstone CY2020–2021, pointing D. 89
Figure F-8. Cumulative count rate versus SEM size of Goldstone CY2020–2021, pointing D. 89
Figure G-1. Range versus range-rate of Goldstone CY2020–2021, pointing 800 km. 90
Figure G-2. Range versus total RCS of Goldstone CY2020–2021, pointing 800 km. 90
Figure G-3. Orbit altitude versus average Doppler inclination of Goldstone CY2020–2021, pointing 800 km. 91
Figure G-4. Flux versus orbit altitude of Goldstone CY2020–2021, pointing 800 km. 91
Figure G-5. Flux versus average Doppler inclination of Goldstone CY2020–2021, pointing 800 km. 92
Figure G-6. Cumulative count rate versus PP SNR of Goldstone CY2020–2021, pointing 800 km. 92
Figure G-7. Count rate versus polarization of Goldstone CY2020–2021, pointing 800 km. 93
Figure G-8. Cumulative count rate versus SEM size of Goldstone CY2020–2021, pointing 800 km. 93
Figure H-1. Histogram of range residuals for the Goldstone CY2018 data. 95
Figure H-2. Spectrogram for Goldstone up-chirp signal backscattered from an object at 800 km slant range. 97
Figure H-3. Spectrogram for Goldstone down-chirp signal backscattered from an object at 800 km slant range. 97
Figure H-4. Output of the matched filter for the received up-chirp backscattered from an object at 800 km slant range. 98
Figure H-5. Normalized range error in the PP channel. 99
Figure H-6. Normalized range error in the OP channel, and the SNR-weighted estimator normalized range error. 99
Figure H-7. Normalized range error in the PP channel, and the SNR-weighted estimator normalized range error. 100

TABLES

TABLE **PAGE**

Table 2-1: Physical dimensions and geographic locations of the antennas used for OD measurements from Goldstone. Geodetic coordinates are with respect to the WGS-84 Ellipsoid. 12

Table 2-2: Pointing details for A, B, C, and D. Computed azimuth and elevation values have been rounded to 4 decimal place input limits for Goldstone's pointing software..... 13

Table 2-3: Minimum and maximum observable orbital altitudes as determined by the null-to-null beam overlaps. 13

Table 2-4: Radar System Hardware Nominal Operating Parameters. 14

Table 2-5: Transmitter Waveform parameters. 14

Table 3-1: The total number of hours, detections, and count rate for the different pointings used in CY2020–2021 data collection. 17

Table 3-2: Tracks provided by JPL, their dates taken, and Doppler sign determination. Note that the observation on 6/12/2021 (in bold) was split into three parts, with inconsistent sign conventions within the file. 22

Table 3-3: JPL Processing Code changes by parameter, before and after changes with the total effect on the data. 24

Table 4-1: Remaining number of hours, detections, and count rate for the different pointings used in CY2020–2021 after ODPO data quality check and processing. 32

Table 4-2: Radar System Hardware Nominal Operating Parameters. 43

Table 4-3: Sensitivity reduction of the DSS-13/DSS-28 configuration relative to DSS-14/DSS-25 for each of the relevant operating parameters. 43

Table 4-4: Total number of hours, detections, and count rate for DSS-13/28 special dataset. 44

Table 4-5: Summary of HUSIR and Goldstone measurements for Cosmos 1408 Debris Cloud. 49

Table A-1: Number of observations and the corresponding hours received from Goldstone from 2008-2018. 60

Table A-2: Pointing details for A, B, C, and D from Figure A-14. Computed azimuth and elevation values have been rounded to 4 decimal place input limits for Goldstone's pointing software. 67

Acronyms

75E	75° Elevation Due East
ASAT	Anti-satellite
AZ	Azimuth
CRLB	Cramer-Rao Lower Bound
CY	Calendar Year
dB	Decibels
dBsm	Square meters measured in decibels
DOY	Day of Year
DSN	Deep Space Network
DSS	Deep Space Station
EL	Elevation
FFT	Fast Fourier Transform
FSPL	Free Space Path Loss
GDSCC	Goldstone Deep Space Communications Complex
Goldstone	Goldstone Orbital Debris Radar
HPBW	Half-power Beamwidth
HUSIR	Haystack Ultra-wideband Satellite Imaging Radar
JPL	Jet Propulsion Laboratory
JSC	Johnson Space Center
LEO	Low Earth Orbit
LFM	Linear Frequency Modulated
ms	Milliseconds
MSE	Mean Square Estimator
NASA	National Aeronautics and Space Administration
OD	Orbital Debris
ODPO	Orbital Debris Program Office
ORDEM	Orbital Debris Engineering Model
OP	Orthogonal Polarization
PP	Principal Polarization
RCP	Right-handed Circularly Polarized
RCS	Radar Cross Section (typically reported in dBsm)
RFI	Radio Frequency Interference
SEM	Size Estimation Model
SNR	Signal-to-Noise Ratio
SSBM	Standard Satellite Breakup Model
SSN	U.S. Space Surveillance Network
WGS	World Geodetic System

1.0 Introduction

1.1 PURPOSE

This report summarizes radar measurement data of the orbital debris (OD) environment in low Earth orbit (LEO) from the Goldstone Orbital Debris Radar (Goldstone) operated by the Jet Propulsion Laboratory (JPL) and provided to the NASA Orbital Debris Program Office (ODPO) at the Johnson Space Center (JSC).

1.2 SCOPE

This report includes data collected by Goldstone during calendar years (CY)2020–2021. Goldstone data from CY2016–2017, as well as data taken in the same year by the Haystack Ultrawideband Satellite Imaging Radar (HUSIR) are presented for comparison purposes. The radar measurement data provide a broad overview of the OD environment in LEO and are used to support the development of NASA's Orbital Debris Engineering Model (ORDEM). Additionally, special observations performed during this time are presented.

1.3 OVERVIEW

For over 30 years, terrestrial radar has been NASA's primary data source for centimeter-sized OD in LEO. HUSIR and Goldstone are the two main radars currently used by ODPO. HUSIR observes debris down to approximately 5.5 mm for altitudes less than 1000 km. Data for OD smaller than 1 mm are provided by *in-situ* measurements. This leaves a gap in debris knowledge for the 1 mm- to 5.5 mm-size range in LEO. Since 1993, Goldstone has collected data on OD as small as approximately 3 mm for altitudes less than 1000 km, contributing to our understanding of the OD environment within that gap.

Several notable system changes were implemented during CY2020–2021. A novel pointing plan was developed to efficiently sample the OD environment from 700 km to 1000 km altitude. Special observations were performed in both experimental setups and in response to the Cosmos 1408 anti-satellite (ASAT) test. This report describes the Goldstone radar systems and changes, the novel pointing plan, radar performance, and data processing and quality control procedures. Results of the statistical survey of LEO and of all special observations are presented as well.

2.0 Radar System Overview

Located far from sources of radio noise in the Mojave Desert, the Goldstone radar's antennas are part of the Goldstone Deep Space Communications Complex (GDSCC). A map showing the GDSCC antenna positions can be found in [1]. ODPO uses three of the antennas (one transmitter and two separate receivers) for OD data collection. Table 2-1 lists the physical dimensions and geographical locations of those antennas for CY2020–2021.

Table 2-1. Physical Dimensions and Geographic Locations of the Goldstone Antennas Used for OD Measurements
Geodetic Coordinates are with Respect to the WGS-84 Ellipsoid

Antenna		Latitude (φ)			Longitude (λ)			Height Above Sea Level (h)
Name	Description	Degree	Min.	Sec.	Degree	Min.	Sec.	Meters
DSS 14	70 meter	35	25	33.24312	243	6	37.66244	1001.390
DSS 25	34 meter	35	20	15.40306	243	7	28.69246	959.634
DSS 26	34 meter	35	20	8.48118	243	7	37.14062	968.686

The Goldstone radar system is bistatic; it uses Deep Space Station (DSS)-14 as a transmitter and either DSS-25 or DSS-26 as receivers [2]. Before 2018, DSS-15 was used as a receiver, providing a relatively short baseline of 500 meters that allowed the beams to overlap all of LEO with a single pointing. In early 2018, DSS-15 was decommissioned and replaced with DSS-25 and DSS-26 of the Deep Space Network Apollo Cluster. Because of the large, approximately 10 km baseline between transmitter and receiver in the current configuration, the antenna beams only overlap for a small fraction of LEO altitudes for a given pointing; therefore, altitudes of interest must now be targeted. In CY2018, most observations were taken such that the transmitter and receiver beams intersected at a slant range of 800 km from DSS-14 [3]. This resulted in a null-to-null range window of approximately 160 km, centered at 800 km, corresponding to approximately 700 km to 860 km in altitude. This target range was chosen for initial measurements with the new system configuration because it roughly corresponds to the altitude with the highest flux of sub-centimeter sized OD.

During CY2019 and most of CY2020, DSS-14 was taken offline for maintenance, giving ODPO time to develop a pointing plan optimized to sample between 700 km and 1000 km in altitude. Full details of the pointing plan, including the development of the pointings, refinement of the altitudes of interest, and analysis of the effects of random pointing errors on beam overlap are given in Appendix A.

For all configurations, DSS-14 is pointed at 75° elevation due East (75E), which mimics the primary observation geometry of the HUSIR radar. The receiver, either DSS-25 or DSS-26, is

then pointed such that the antenna beams intersect at the altitude of interest. Goldstone collects data in a fixed azimuth (AZ) and elevation (EL) staring mode where OD is not tracked but observed as it passes through the beam. ODPO found that with four pointing geometries, called A, B, C, and D, altitudes from 700 km to 1000 km could be sampled with minimal loss of sensitivity relative to the legacy Goldstone radar system. Details of each pointing, such as AZ and EL of each receiver, intersection slant range for the transmitter, and intersection altitude, are presented in Table 2-2. Table 2-3 shows the minimum and maximum observable orbital altitudes as determined by the null-to-null beam overlaps.

Table 2-2. Pointing Details for A, B, C, and D
Computed Azimuth and Elevation Values have been Rounded to Four Decimal Place Input Limits for Goldstone's Pointing Software

Pointing Name	Intersection Altitude (km)	DSS-14 Slant Range (km)	DSS-25 Azimuth (deg)	DSS-25 Elevation (deg)	DSS-26 Azimuth (deg)	DSS-26 Elevation (deg)
A	725.967	755.155	86.7862	75.0842	86.7135	75.1005
B	785.860	816.717	87.0054	75.0800	86.9380	75.0953
C	860.889	893.794	87.2368	75.0753	87.1749	75.0895
D	957.904	993.393	87.4830	75.0700	87.4270	75.0831

Table 2-3. Minimum and Maximum Observable Orbital Altitudes as Determined by the Null-to-Null Beam Overlaps

Pointing	Minimum Orbital Altitude (km)	Maximum Orbital Altitude (km)
A	660.3	806.4
B	709.7	881.0
C	770.4	976.1
D	847.5	1102.8

Most observations in CY2020–2021 were performed using these pointings. Exceptions include an observation using the 800 km pointing in CY2018, experimental observations using DSS-13 and DSS-28 during the DSS-14 downtime, and special breakup response observations. Each of these exceptions has a dedicated section later in this report.

For OD observations, Goldstone transmits a right-handed, circularly polarized (RCP) waveform and receives both left-handed, circularly polarized and RCP returns, referred to as principal polarization (PP) and orthogonal polarization (OP), respectively. Table 2-4 lists the nominal operating parameters of the radar system hardware. The Goldstone waveform is a linear frequency modulated (LFM) "chirp" with a center frequency of 8.56 GHz and a chirp bandwidth of 300 kHz. Goldstone alternates between positive frequency sloped "up-chirps" and negative frequency sloped "down-chirps." Measurements from pairs of up- and down-chirps are used to mitigate frequency-dependent range biases caused by delay-Doppler (or range-Doppler) coupling effects inherent to LFM waveforms [4].

Table 2-4. Radar System Hardware Nominal Operating Parameters

Operating Parameter	Goldstone
Peak Power (kW)	440
Transmitter Frequency (GHz)	8.56
Transmitter Wavelength (cm)	3.5
Transmitter Antenna Diameter (meter)	70.0
Receiver Antenna Diameter (meter)	34.0
Transmitter Half-power beamwidth (HPBW) (deg)	0.03
Receiver HPBW (deg)	0.06
Transmitter Antenna Gain (dB)	74.24
Receiver Antenna Gain (dB)	68.42
Avg. System Temperature (K)	21.79
Intermediate Frequency Bandwidth (MHz)	1.5

In May 2021, JPL updated the chirp and receive window parameters of its waveform. Because the beam overlap with DSS-25 is much smaller than the legacy DSS-15 configuration, a large maximum unambiguous range is no longer necessary. Therefore, the pulse period was decreased from 22.503 ms to 18 ms. The chirp duration was also increased from 2.34 ms to 2.9 ms. The net effect of the two changes resulted in a 55% increase in average power (product of peak power and duty cycle). A comparison of the old and new waveform operating parameters is provided in Table 2-5.

Table 2-5. Transmitter Waveform Parameters

Operating Parameter	Old Waveform	New Waveform
Pulse Period (ms)	22.503	18
Pulse (chirp) Duration (ms)	2.34	2.9
Pulse (chirp) Bandwidth (kHz)	300	300
Pulse Repetition Frequency (Hz)	44.44	55.6
Average Power (kW)	45.75	70.95
Receiver Delay (ms)	0.195	0.1
FFT Length (ms)	19.968	15
Range Window (km)	378-3373	450-2698
Altitude Window (km)	360-3291	430-2627

2.1 RADAR PERFORMANCE

Of the system parameters that affect radar sensitivity, the most variable are transmit power and system noise temperature. Although these two parameters are not directly correlated, they both contribute to variations in the signal-to-noise of the radar system. These values are tracked by JPL and reported to ODPO for each observation. In CY2020, Goldstone operated below nominal peak power at 277 kW. In CY2021, Goldstone ran closer to nominal peak power at ranges from 430 kW to 440 kW. Figure 2-1 shows the history of the transmit power, along with the nominal

peak power of the system (440 kW). Figure 2-2 shows the variation in the receiving system noise temperature, which affects the sensitivity of the receiver. Noise temperature is an effective temperature that includes the brightness temperature of various sources of incident RF noise as well as path losses. The system noise temperature of the receiving dish averaged 19.79 K.

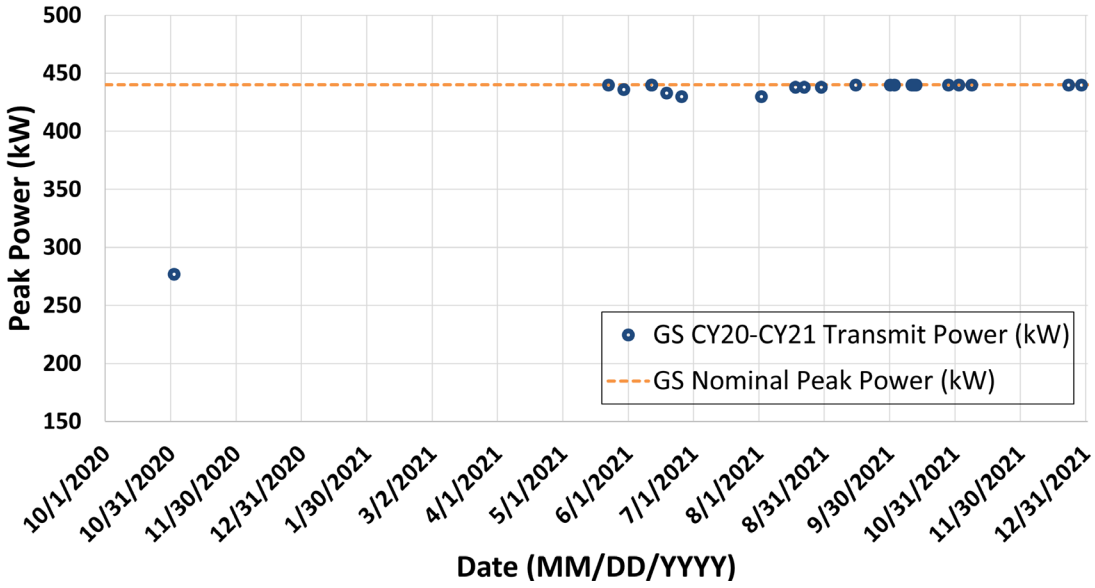

Figure 2-1. System transmit power history for Goldstone DSS-14 from CY2020–2021.

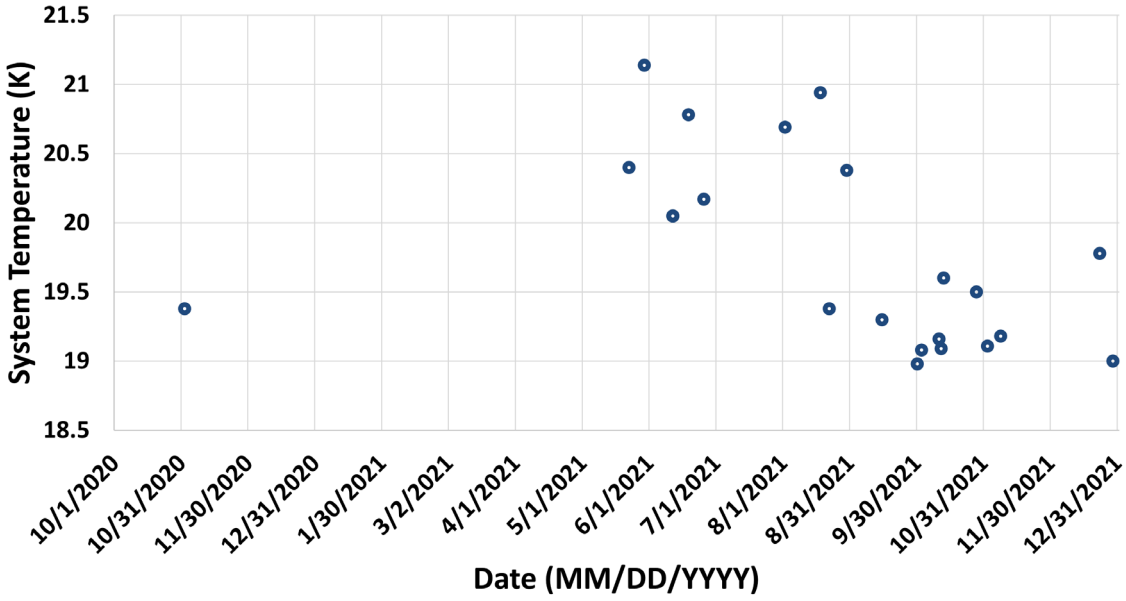

Figure 2-2. System temperature history for Goldstone DSS-25 and DSS-26 from CY2020–2021.

The altitude-dependent debris size detectable by Goldstone is determined by sensitivity and pointing. Figure 2-3 shows a sensitivity curve, the dashed black line, as a function of altitude of Goldstone CY2020–2021 to a 99% completeness level, overlaid on a scatter plot of orbit altitude versus Size Estimation Model (SEM) size for the dataset. This curve shows the altitude-dependent size at which 99% of objects passing through the beam are detected. Details of the sensitivity curve calculation are found in [5]. The horizontal red dashed lines represent the altitude range of focus for the CY2020–2021 dataset (700 km to 1000 km). From Figure 2-3, the Goldstone CY2020–2021 data is approximately 99% complete down to a size of 2.2 mm at an altitude of 1000 km. The sensitivity curve here depicts the maximum sensitivity of the combined pointings, causing the scalloping shape from 700 km to 1000 km. Outside of this altitude band, sensitivity decreases significantly as the main beam overlap decreases, and beam overlap occurs only in the sidelobes.

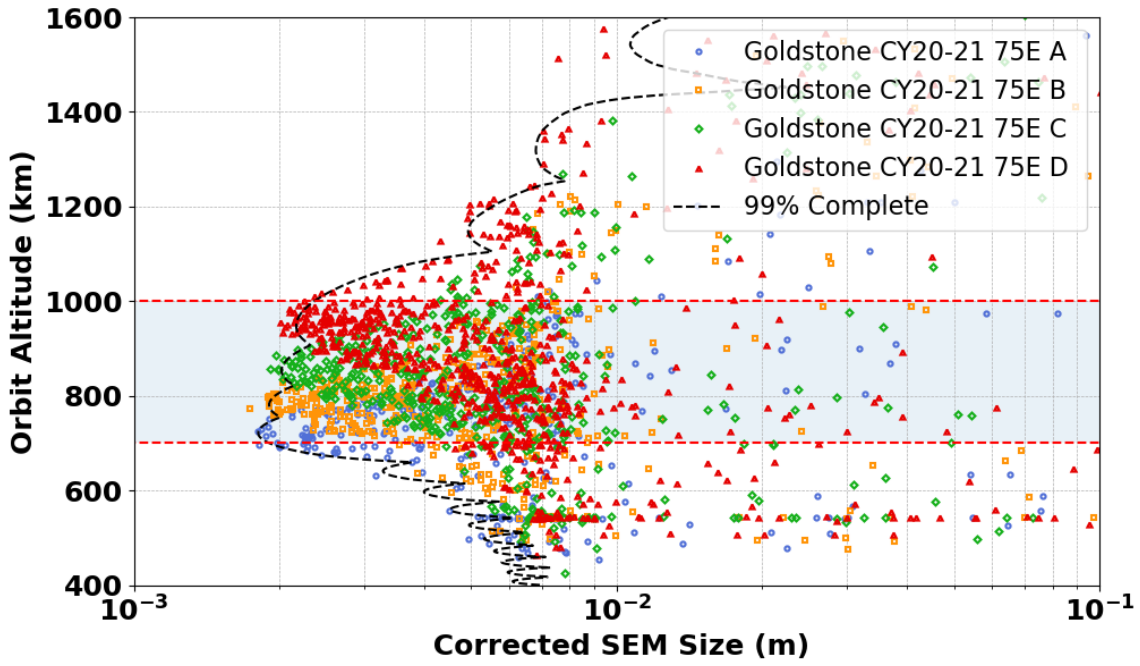

Figure 2-3. Orbit altitude versus SEM size of CY20-21 data with 99% completeness curve overlaid (black dotted line). Altitude range of interest is also shown (red dotted line).

3.0 Data Collection and Radar Processing

3.1 JPL DATA COLLECTION AND PROCESSING

After the OD data is processed by JPL personnel and reviewed by a subject matter expert, it is delivered to ODPO. Table 3-1 summarizes the total hours collected during CY2020–2021, incorporating the hours and number of detections prior to data analysis and curation activities conducted by ODPO. Only one of the observations for CY2020 was at 800 km altitude; not providing enough observation data to obtain statistically significant results. This data is presented separately in Appendix G.

Table 3-1. Total Number of Hours, Detections, and Count Rate for the Different Pointings Used in CY2020–2021 Data Collection

Year	Pointing	Number of Hours	Total # of detections	Count Rate (#/hr)
2020–2021	A	15.9	334	21.0
2020–2021	B	22.8	511	22.4
2020–2021	C	29.9	560	18.7
2020–2021	D	33.4	809	24.2
Total		**102.0**	**2214**	**21.7**

For a detection to be declared valid, at least two pulses must pass the signal-to-noise (SNR) detection threshold. For CY2020–2021, all detections with an SNR threshold 11.76 decibels (dB) or greater are flagged as potential detections. Goldstone then separates detections further: all detections with an SNR greater than 13 dB are automatically declared valid, but those with an SNR between 11.76 dB and 13 dB are manually inspected to determine validity.

For each valid detection, JPL measures SNR, range, Doppler frequency shift, and radar cross section (RCS). From these measured parameters, JPL then estimates an orbital inclination and diameter. Also recorded are the total number of pulses in the detection group and the chirp number and detection time of the highest SNR pulse within the detection group. Detection and measurements are performed independently on the PP and OP channels. Preliminary detection lists for each polarization are then combined by matching detections between the PP and OP channels that have overlapping chirp counts. This data is then delivered to ODPO.

3.2 ODPO PROCESSING AND DATA QUALITY

ODPO performs post-processing and data quality checks on the JPL data to verify data integrity and improve parameter estimation. For CY2020–2021 data, these checks included PP and OP channel range and range-rate residuals analysis, a Doppler sign consistency check, radio frequency interference (RFI) detection, and quantization correction in RCS.

3.2.1 *NASA Beam Gain Correction*

Unlike HUSIR, Goldstone does not have a monopulse receiver and is therefore not able to give information on the path taken by an object through the beam. When an object's RCS is calculated using the peak gain of the transmitter and receiver, it represents a lower bound on the object's true RCS due to off-axis beam shape losses. This effect becomes more prominent in a bistatic system as the distance between the transmitter and receiver increases, where peak gain only occurs at the beam intersection point and decreases rapidly moving away from it. In Goldstone, since the beam width of the transmitter is much smaller than that of the receiver and the baseline is large, the off-axis beam shape losses become a strong function of the range from the transmitter.

As a first-order correction to these off-axis beam losses, a model was created to derive a beam shape correction factor as a function of range from the transmitter. In the model, the transmitter and receiver are placed on an Earth ellipsoid and their boresight vectors are rotated to the

appropriate AZs and ELs. Then, a set of points is chosen on a plane perpendicular to the boresight of the transmitter, Antenna 1 in Figure 3-1, at a range *R* from the transmitter.

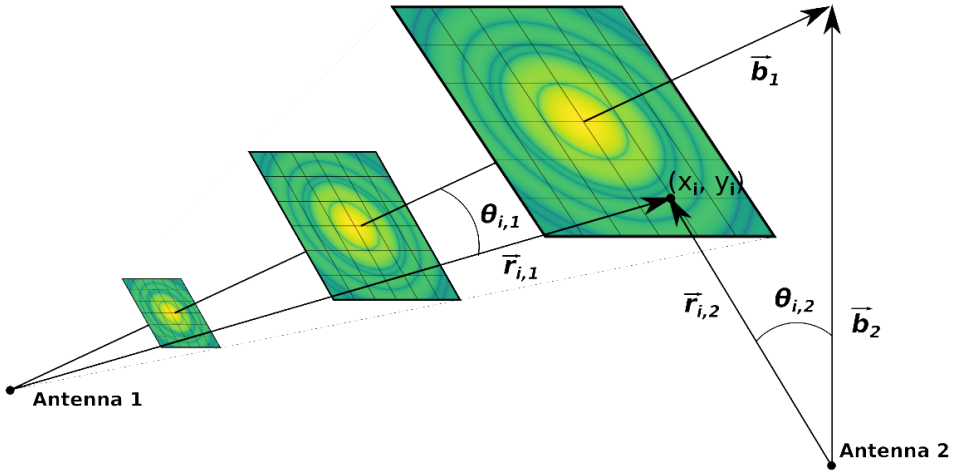

Figure 3-1. Geometry of the beam shape correction factor model calculation.

For each point on the plane, the angular offset from boresight for both the transmitter and receiver are calculated as

$$\theta_{i,j} = \frac{\vec{r}_{i,j} \cdot \vec{b}_j}{|\vec{r}_{i,j}||\vec{b}_j|}$$

where $\vec{r}_{i,j}$ is the vector from the j^{th} antenna to the i^{th} point in the plane and $\vec{b}_j$ is the boresight vector of the j^{th} antenna. The beam shape correction factor at the range *R* from the transmitter is then calculated as the peak gain product of the transmitter and receiver as shown in

$$\Delta\sigma = Max\left[\prod_{j=1,2} G_j(\theta_{i,j})\right]$$

where G_j is the normalized gain pattern of the j^{th} antenna as a function of the angular offset from boresight. Each antenna is modeled as a uniformly illuminated circular aperture with a central obscuration as described in [6]. This process is then repeated at several ranges from the transmitter by sliding the reference plane down the boresight vector of the transmitter to derive a numerical function for the beam shape correction as a function of range from the transmitter. An example of the beam shape correction factor for the DSS-14/DSS-25 transmitter/receiver pair in the D pointing is shown in Figure 3-2.

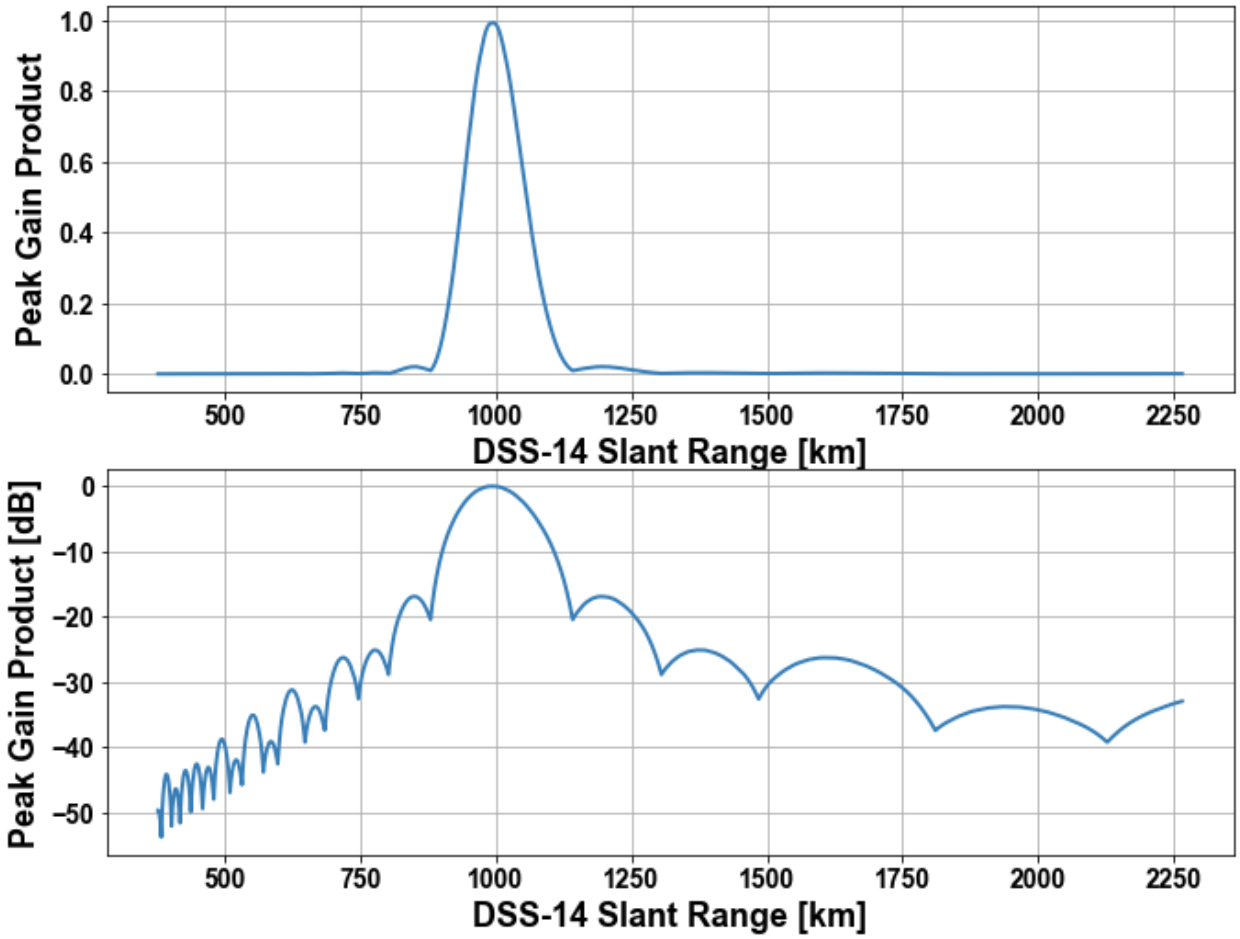

Figure 3-2. An example of the beam shape correction factor as a function of range from the transmitter for the DSS-14/DSS-25 transmitter/receiver pair in the D pointing.
The top chart is in linear units while the bottom is in dB.

3.2.2 *Range and Range-Rate Residuals*

For detections that triggered both PP and OP channels, a data quality check was performed to find those with significantly different range measurements between channels. The residual (or difference) in the reported PP and OP ranges were calculated along with the PP and OP SNR residuals of the same detections. The resulting range and SNR residuals were then plotted against each other in Figure 3-3. Detections where the range residual was more than two standard deviations away from the mean range residual were removed. The overall spread of range residuals was from -649 km to 276 km. Range-rate residuals, analyzed using the same process, are shown in Figure 3-4. Because the range-rate residuals have such a large spread about the average value, two iterations of variance estimation and outlier removal were needed. With this analysis, the spread of range-rate residuals was from –4.37 km/s to 3.65 km/s and 85 detections determined to be outliers were removed from the dataset. A detailed flowchart describing the residual process and detection removal is provided in Appendix B.

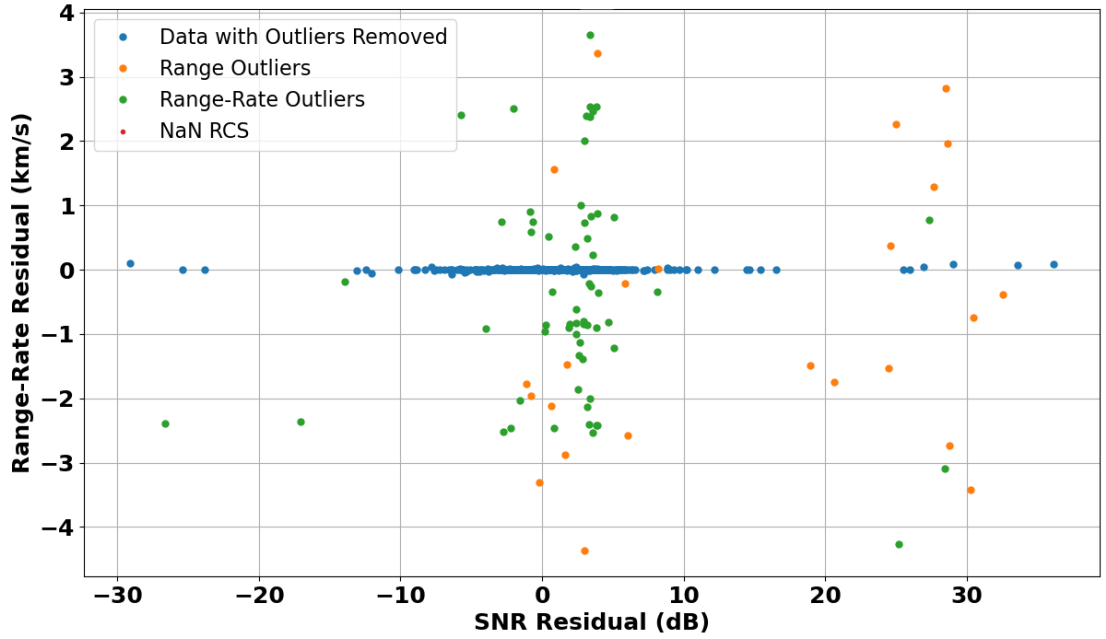

Figure 3-3. Plot of range residuals to SNR residuals for CY2020–2021 data provided by JPL. Points in orange represent residuals that fell outside the 2σ difference in range.

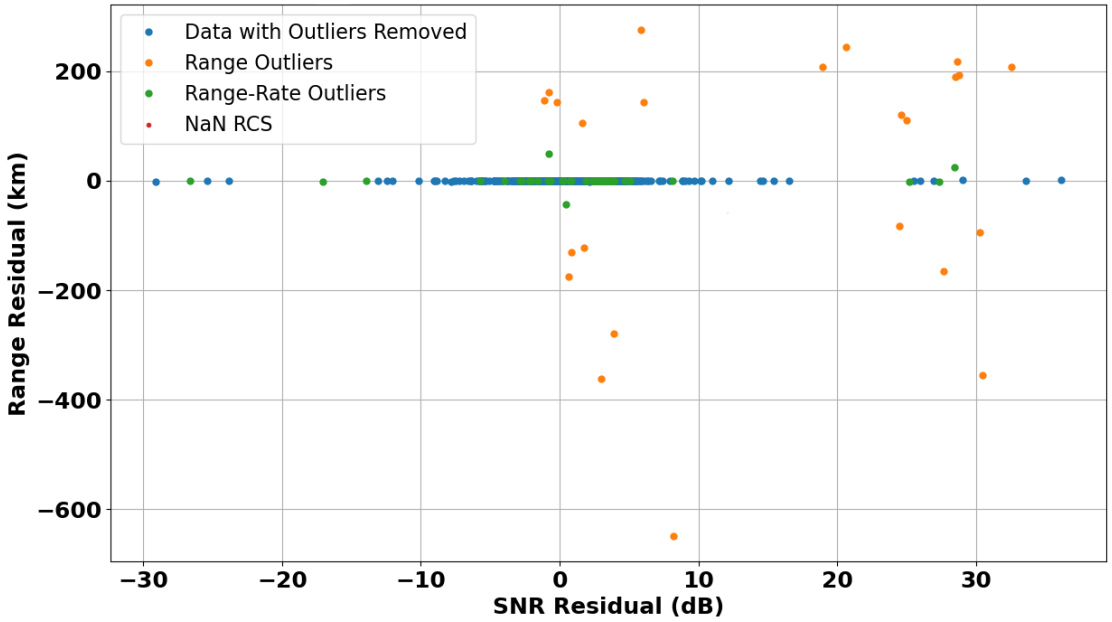

Figure 3-4. Plot of range-rate residuals to SNR residuals for CY2020–2021 data provided by JPL. Points in green represent range-rate residuals that fell outside the 2σ difference in range-rate.

After range and range-rate residual outliers were removed, a singular range and range-rate value was calculated for each of the remaining detections as an SNR weighted average of the PP and OP values. For range of SNR values in the Goldstone dataset, an SNR weighted average

provided a better estimate than a simple average or choosing either the PP or OP value based on SNR criteria, as shown in Appendix H.

3.2.3 *Doppler Sign Consistency*

The detection lists delivered by JPL to ODPO report the measured Doppler frequency shift for each detection. This Doppler frequency shift is used to calculate the velocity along the radar line-of-sight, known as range-rate. A Doppler sign convention is used to define positive Doppler frequency shifts as either positive or negative range-rates. This convention was inconsistent for CY2020–2021 deliveries and changed within a file in some instances. Since Goldstone transmits LFM chirps that alternate between up-chirps and down-chirps, the inconsistency was tracked to a software bug where the odd- and even-numbered chirp number counts, which are meant to correspond to down- and up-chirps, respectively, were swapped. By reversing the Doppler sign convention, the software did not properly determine whether the first pulse in a file was a down- or up-chirp. This software bug was fixed in March 2022.

Before the cause of the Doppler sign inconsistency was identified, ODPO developed a method to find and correct the Doppler sign convention for each observation. For each observation, the distribution of detections in range/range-rate space was compared to an exemplar dataset. When the Doppler sign convention was opposite that used by ODPO, the detections did not line up with the exemplar, but appeared mirrored across the y-axis. Figure 3-5 shows an example where the mirrored groups of detections, in orange, are shown with arrows and CY2016 data acts as the exemplar.

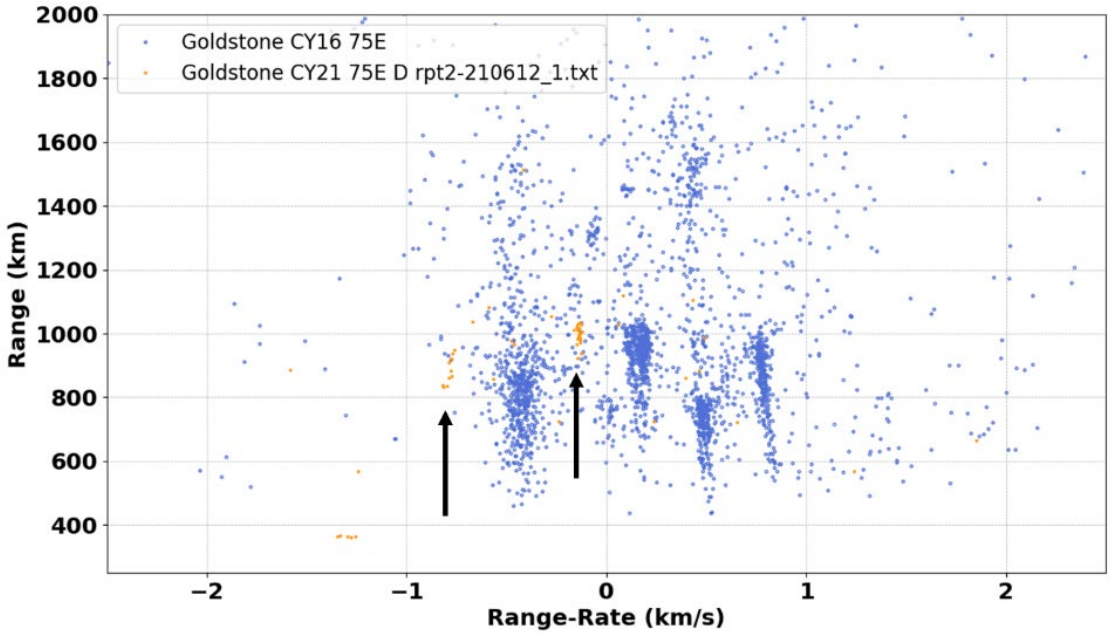

Figure 3-5. Range versus range-rate of a CY2021 observation overlaid on CY2016 data, illustrating the mirroring effect of the Doppler sign inconsistency.

This process was performed for each observation. Doppler signs were recorded in a table, and the range-rate was corrected by multiplying by -1 where needed. Table 3-2 shows a list of

observations with Doppler sign conventions determined by ODPO. Note that the observation on 12 Jun 2021 (bold) was split into three parts, with inconsistent sign conventions within the file.

Table 3-2. Tracks Provided by JPL, Dates Taken, and Doppler Sign Determination.*

Filename	Date	Doppler Sign
rpt-201102.txt	2 Nov 2020	1
rpt2-211229.txt	29 Dec 2021	1
rpt-210530.txt	30 May 2021	-1
rpt2-211011.txt	11 Oct 2021	1
rpt2-210619.txt	19 Jun 2021	-1
rpt2-210822.txt	22 Aug 2021	1
rpt2-211012.txt	12 Oct 2021	1
rpt2-211102.txt	2 Nov 2021	1
rpt2-210626.txt	26 Jun 2021	-1
rpt2-210818.txt	18 Aug 2021	-1
rpt2-210830.txt	30 Aug 2021	-1
rpt2-211001.txt	1 Oct 2021	-1
rpt2-211013.txt	13 Oct 2021	-1
rpt2-211108.txt	8 Nov 2021	1
rpt-210523.txt	23 May 2021	1
rpt2-210612_1.txt*	12 Jun 2021	-1
rpt2-210612_2.txt*	12 Jun 2021	1
rpt2-210612_3.txt*	12 Jun 2021	1
rpt2-210802.txt	2 Aug 2021	1
rpt2-210915.txt	15 Sept 2021	1
rpt2-211003.txt	3 Oct 2021	1
rpt2-211028.txt	28 Oct 2021	-1
rpt2-211223.txt	23 Dec 2021	1

3.2.4 *Radio Frequency Interference Inspection*

To check the data for RFI, range-rate versus day of year (DOY) was plotted to find changes in detection rates or transmitter dropout. RFI, which typically has a uniform distribution in range-rate, manifests as a vertical line of detections, and detection rates in the presence of RFI typically increase significantly. Figure 3-6 shows one such plot for observations made by HUSIR in CY2018 demonstrating the difference between true detections and data contaminated by RFI. No RFI, as defined here, was seen in the datasets for CY2020–2021 (Figure 3-7).

* The observation on 06/12/2021 was split into three parts, with inconsistent sign conventions within the file.

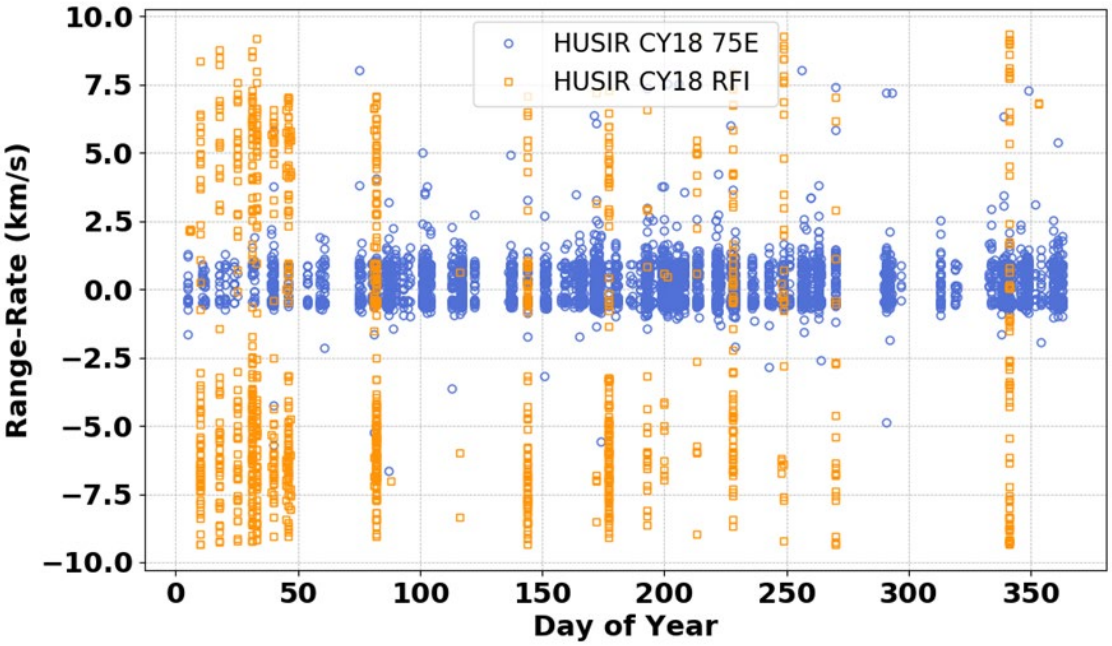

Figure 3-6. Exemplar range-rate versus DOY scatterplot for the HUSIR 75E CY2018 dataset. RFI is identified with the orange data points.

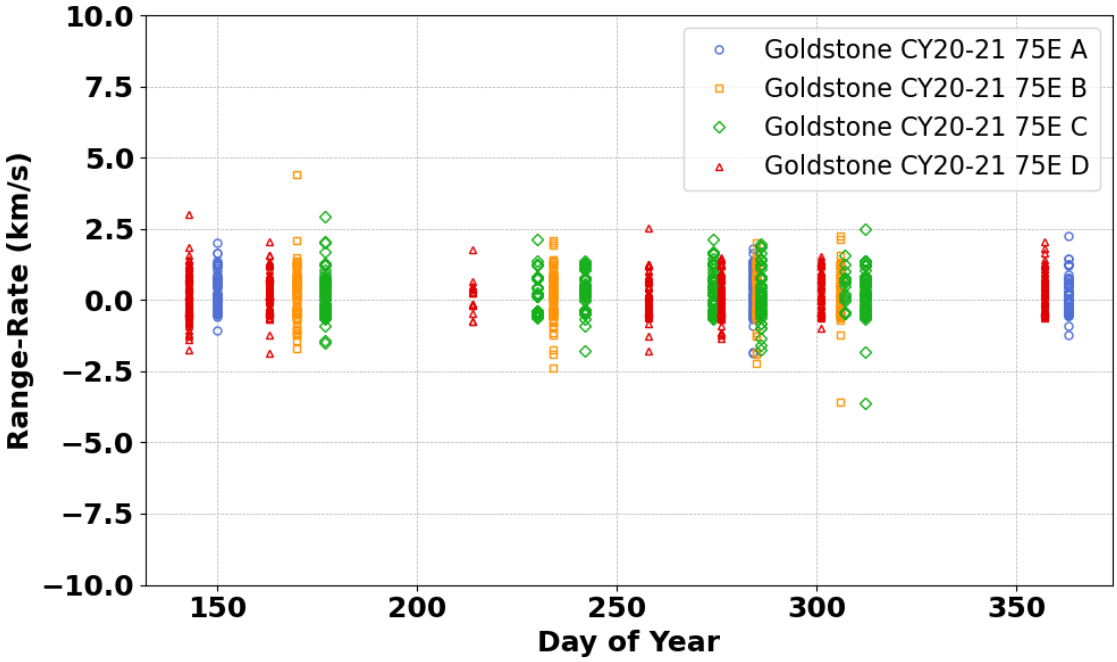

Figure 3-7. Range-rate versus DOY for the Goldstone CY2020–2021 dataset. No discernable RFI is present.

3.2.5 *JPL Reported Range, RCS calculation, and Beam Overlap Correction*

In CY2020, JPL updated their processing code to improve the accuracy of bistatic measurements. Examination of the JPL source code revealed three definitional changes: first, the

definition of reported range; second, the range used in RCS calculation; and third, the off-boresight angle used in beam overlap correction. The reported range was changed from half the round-trip distance, r, to the range from the transmitter to the target, r_t. The range used in RCS calculations was changed from using r^4 to using r_t^2 and r_r^2, where r_r^2 is the range from the target to the receiver. The calculated receiver off-boresight angle was changed from $\delta = \frac{|r_0 - r|\beta}{r}$ to $\delta = \sin^{-1}\left(\frac{r_t - r_0}{r_r}\sin\beta\right)$, where r_0 is the intersection range, β is the bistatic angle of the pointing geometry, and δ is the angular offset from the boresight of DSS-14. ODPO post-processing software was adjusted to handle these changes and the effect on final data has been analyzed. Table 3-3 summarizes the above-described parameter changes and effects in the JPL processing code. Figure 3-8 shows the relevant geometry, where:

$$r_0 = r_1,$$

$$r = \frac{r_1 + r_2 + r_3}{2},$$

$$r_t = r_1 + r_2,$$

$$r_r = r_3,$$

and r_4 is the baseline between the transmitter and receiver.

Table 3-3. JPL Processing Code Changes by Parameter, Before and After Changes with the Total Effect on the Data

Parameter	Before	After Changes Applied	Difference
Reported Range	Half of round-trip distance	Range from transmitter to target (calculated from round-trip time, assuming target on transmitter boresight)	Max difference in reported ranges are < 0.2 km
RCS Calculation	Calculated with half of the round-trip distance raised to the fourth power	Calculated using transmitter to target and receiver to target ranges squared	Max difference in reported RCS is < 0.00005 dB
Beam Overlap Correction $\Delta\sigma = 1 + 6000\,\delta^{2.5}$	Calculated receiver off-boresight angle $\delta = \frac{\lvert r_0 - r\rvert\beta}{r}$	Calculated receiver off-boresight angle $\delta = \sin^{-1}\left(\frac{r_t - r_0}{r_r}\sin\beta\right)$	Maximum difference in reported RCS is < 0.005 dB

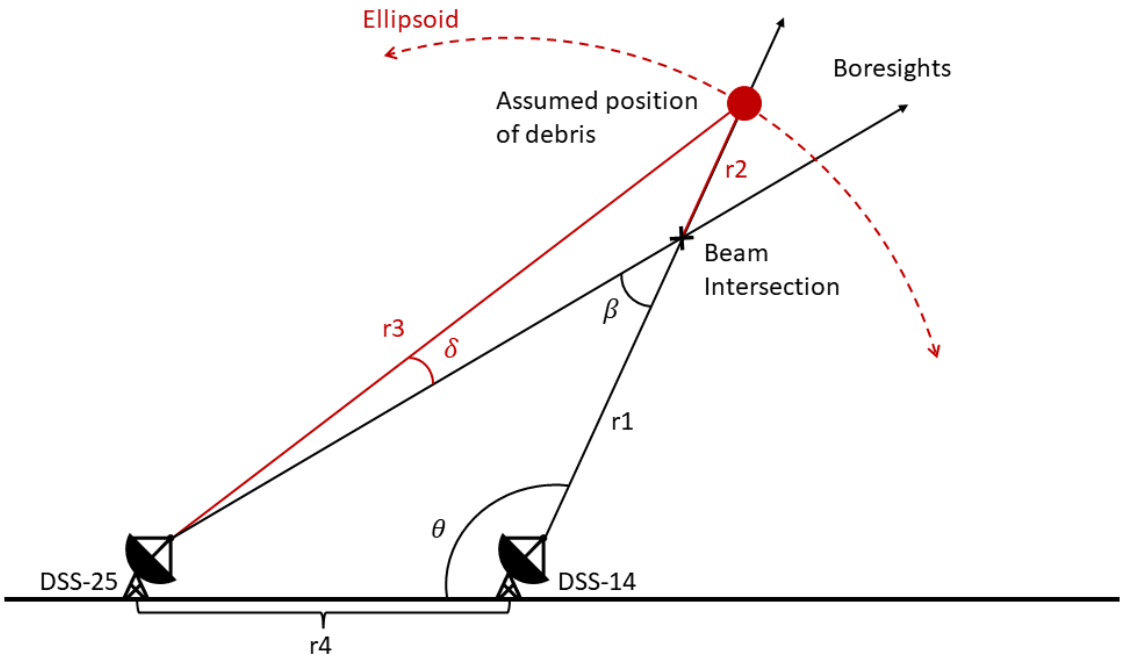

Figure 3-8. Geometry for bistatic range and boresight angle offset calculation.

3.2.6 *RCS Quantization Correction*

Quantization errors were introduced into the data collection summaries provided by Goldstone, an issue arising from the use of linear units in the delivered detection lists and the truncation to a specific number of decimal places rather than number of significant figures. These quantization errors are corrected for reported RCS values ≤ 5.47 mm^2 by re-calculating the RCS from the reported size using the formula:

$$RCS_{mm^2} = \frac{9}{4}\pi \frac{(Size_{mm})^6}{(\lambda_{mm})^4}$$

This is possible because the reported size is calculated from the measured RCS before being written to a file. Additionally, the values for size show a greater dynamic range when truncated to a fixed number of decimal places, relative to the reported RCS, due to the relationship between RCS and size used by JPL. Figure 3-9 shows an example of the quantization errors introduced in the reported RCS values between -70 dBsm and -80 dBsm in the Goldstone CY2016 data, with quantization for RCS values beginning at approximately -70 dBsm. Although the quantization correction was applied to the CY2020–2021 data, quantization is not as pronounced as that in CY2016 since the reduced beam overlap of the radar did not allow detection of as many objects in the affected RCS regime. Therefore, a similar plot for CY2020–2021 is not included in this section. A plot showing the corrected RCS values is presented in the results section.

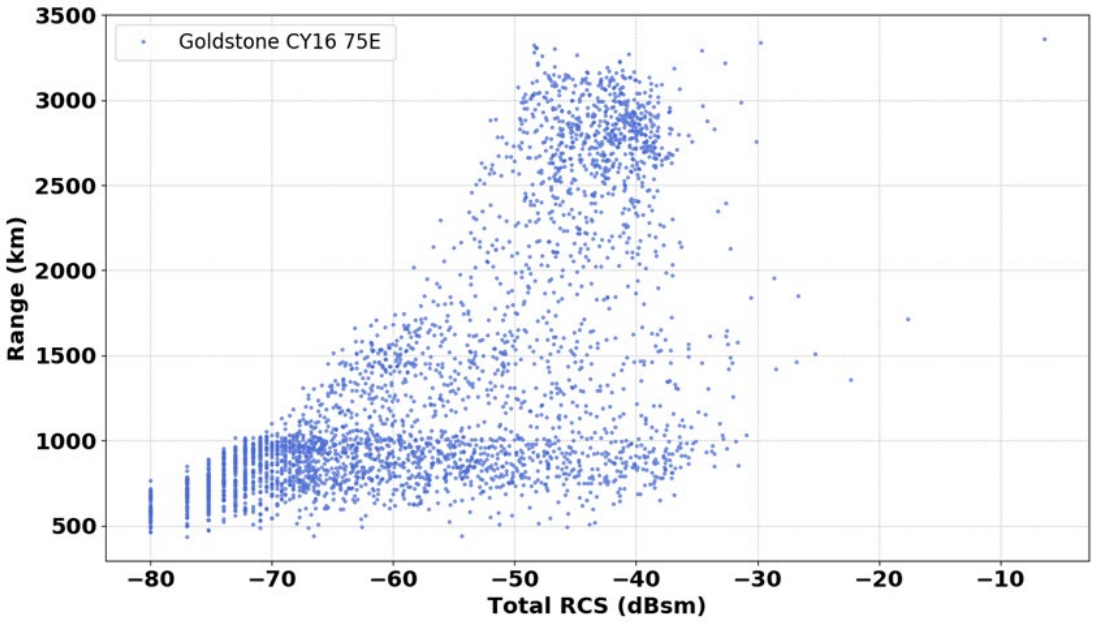

Figure 3-9. Example total RCS versus range scatterplot for CY2016 Goldstone data illustrating the RCS quantization effect for low RCS objects.

3.3 STANDARD CHART EXAMINATION

To ensure data quality, a standard set of charts illustrating the behavior of the data set over relevant radar and detected object parameters including range, range-rate, RCS, NASA SEM-estimated size, SNR, inclination, and altitude are generated for inspection by OD subject matter experts. These sets are compared with previous annual data sets and/or data sets from other sensors to ensure behavior is consistent and differences are understood. Once this process is complete, a final detection list is placed under configuration management for use by teams modeling the OD environment.

During CY2021, the qualitative behavior of the polarization distribution of detections experienced a major change. Since polarization information first became available in Goldstone data in late CY2015, the polarization distribution has been qualitatively similar to that of HUSIR when appropriate size and altitude filters are applied. Likewise, data from Goldstone in CY2018 (the first using DSS-25 and DSS-26 as receivers) showed qualitatively similar polarization distributions [3]. Figure 3-10 shows the polarization distribution of an observation taken at the B pointing on 19 June 2021. When compared to data from CY2016, it shows similar behavior. The shaded regions represent the 2σ Poisson uncertainty bounds. Details on the definition and significance of polarization are presented in Section 4.

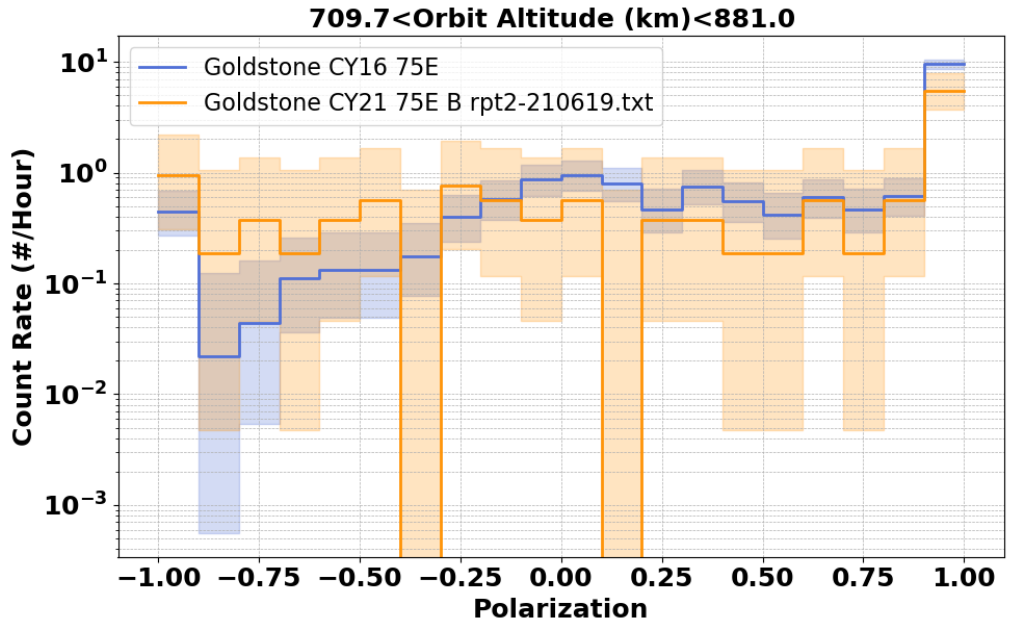

Figure 3-10. Polarization distribution of 19 June 2021 observation compared to CY2016 data. The shaded regions represent the 2σ uncertainty bounds.

Figure 3-11 shows the polarization distribution of another observation taken at the B pointing on 12 October 2021. The distribution exhibits no negatively polarized detections, with most detections having a polarization between 0.1 to 0.6. The right-most bin consists of detections with only a PP response, which is polarization of +1 by default. All observations from 30 August 2021 onward showed this different polarization distribution. Since the distribution remained similar from CY2015 up to early CY2021, the variation cannot be attributed to the change of receivers in CY2018 nor the change in pointings in CY2021.

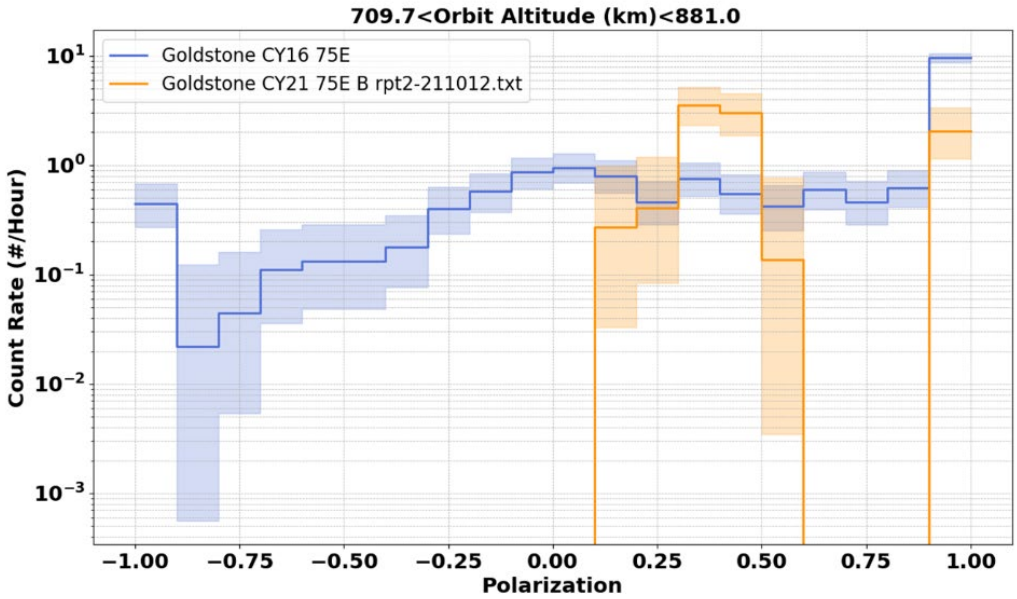

Figure 3-11. Polarization distribution of 12 October 2021 observation compared to CY2016 data. The shaded regions represent the 2σ uncertainty bounds.

In examining the data from before and after 30 August 2021 it was found that cumulative count rates versus SEM-size also changed. Figure 3-12 shows the cumulative count rate versus SEM-size for an observation taken at the D pointing on 2 August 2021. When filtered on the main beam overlap the cumulative count rates match well. Figure 3-13 shows the cumulative count rate versus SEM-size for an observation taken at the D pointing on 3 November 2021. Here the cumulative count rate is lower than what was observed in CY2016 across a range of sizes.

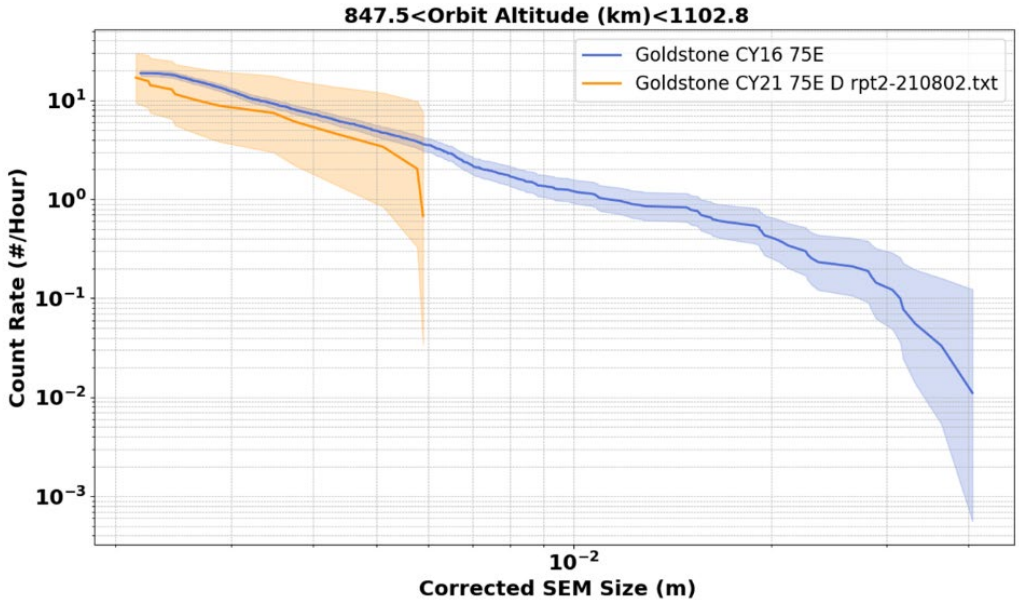

Figure 3-12. Cumulative count rate versus SEM-size for 2 August 2021 observation compared to CY2016 data. The 2 August 2021 observation occurred prior to hardware issues with the PP and OP cables. The shaded regions represent the 2σ uncertainty bounds. The count rates seen before the hardware issues match those from CY 2016 within uncertainties.

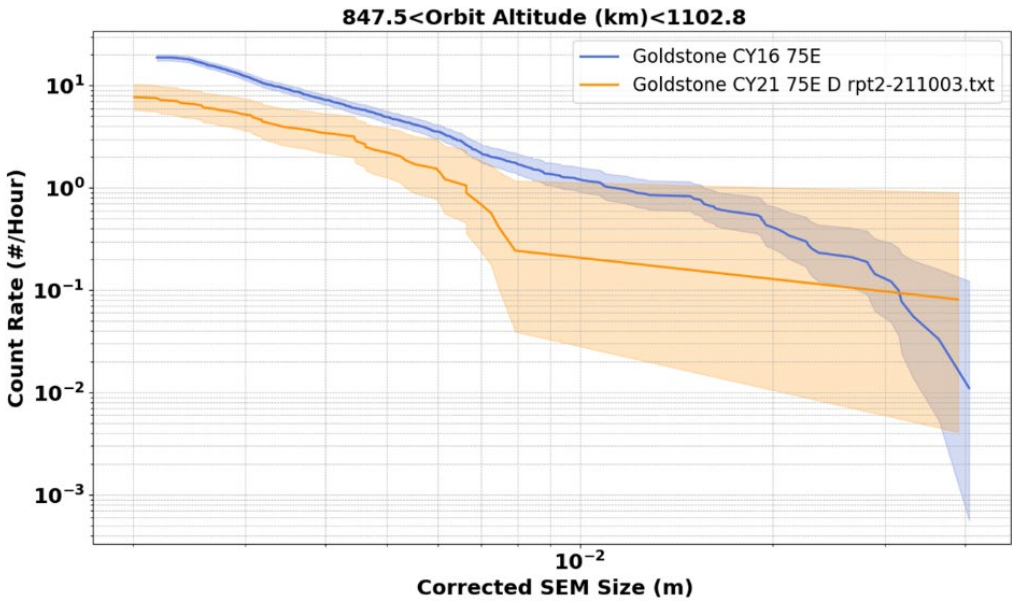

Figure 3-13. Cumulative count rate versus SEM-size for 3 November 2021 observation compared to CY2016 data. The 3 November 2021 observation occurred after hardware issues with the PP and OP channel cables occurred.
The shaded regions represent the 2σ uncertainty bounds. The count rates seen after the hardware issues are notably lower than those observed in CY 2016. N.B.: the probability of detecting objects > 10 cm in a given observation is low. The 3 November observation recorded a single object >10 cm.

The ODPO and JPL teams determined that these data features were caused by two separate hardware issues. First, signal attenuation on an OP channel cable was found to be several decibels higher than expected and was replaced. Second, early in the signal chain, cables were swapped at a patch panel such that both the PP and OP signal chains were connected to the PP channel output, resulting in both the PP and OP channel digitizers recording signals from the PP channel. Since the OP channel signal was never recorded for these observations, they are currently being reanalyzed as single-polarization only data. For this report, all data from 30 August 2021 and a single observation from 26 June 2021 (which also experienced low count rates) were removed from the environmental summary charts in Sections 4.1 and 4.2 .

3.4 THE SIZE ESTIMATION MODEL

Size estimates from radar data sources are reported using the NASA SEM, which relates the RCS of debris objects from the measured PP and OP channels and a wavelength to an empirically derived characteristic length. The SEM originated from an early 1990s study led by XonTech that used representative debris objects taken from two U.S. Department of Defense hypervelocity impact tests of satellites conducted at the Arnold Engineering Development Complex [7] [8] [9]. In addition to representative objects from the impact tests, several debris-like objects were included in the sample to better represent the postulated debris environment at the time.

The RCS values for the 39 debris objects were measured at an RCS radar range operated by the System Planning Corporation. RCS measurements of these objects were taken over 4 commonly used radar frequency bands (S band: 2.5647–3.9111 GHz; C band: 4.116–7.986 GHz; X band: 8.1544–12.7684 GHz; and Ku band: 12.924–17.538 GHz), with 8 frequency samples taken in the lowest frequency band and 16 frequency samples taken in the remaining 3 frequency bands. These radar frequency bands correspond to the frequency bands in use by OD radars. Measurements were taken from multiple, different orientations of the debris objects to understand the distribution of possible RCS values that each piece of debris would present to a radar as the tumbling debris passes through the radar beam [10] [11] [12].

The characteristic length is the average of the projected dimensions, or the dimensions along the shadow of a debris object. ODPO defines *x* as the longest projection dimension, *y* as the longest shadow dimension perpendicular to *x*, and *z* as the longest projection dimension orthogonal to both *x* and *y* [13]. As shown in Figure 3-14, the first axis was chosen to coincide with the largest dimension, the second axis to coincide with the largest dimension in a plane orthogonal to the first axis, and the third axis to be orthogonal to the plane defined by the first two axes. The characteristic length of an object is referred to interchangeably as size or diameter.

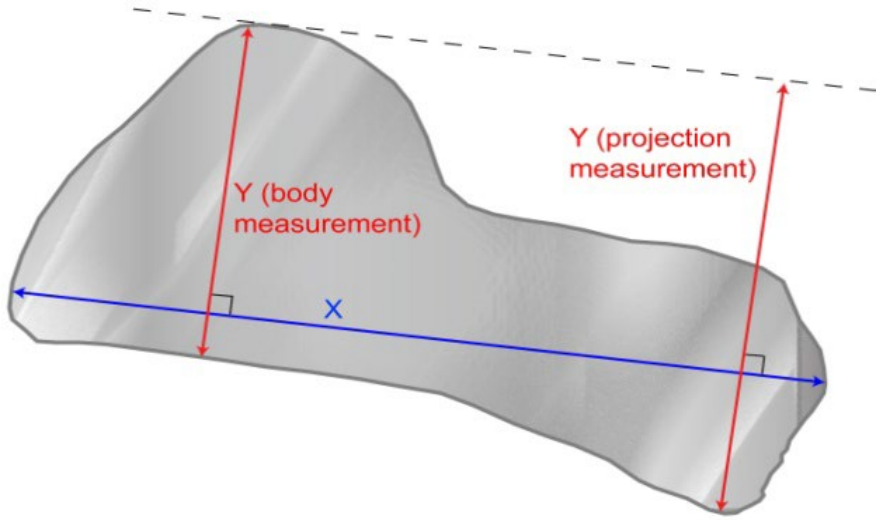

Figure 3-14. Illustration of body and projected measurement on complex shape used in finding characteristic length.

Radar data from sensors operating with different wavelengths may be compared by scaling the size by the wavelength, λ, of the measurement frequency and the RCS by the square of the wavelength. This results in a normalized size, diameter/ λ, and a normalized RCS, RCS/ λ^2. Combining all the measurements – different frequency and object orientations – onto a single plot results in the normalized RCS versus normalized size shown in Figure 3-15. Each of the 2072 data points on this plot is a weighted average for a single debris object over the hundreds of different orientations at a single frequency. The data were weighted to account for the non-uniform sampling of the object orientations during collection.

From the plot shown in Figure 3-15, a scaling curve – the solid black line – was developed, which is the mean of the measured RCS for each normalized size. The solid blue line shows the theoretical RCS for a sphere as a function of size. For debris sizes much smaller or larger than the radar wavelength, the scaling curve approaches the same result as the Rayleigh or optics regions, respectively, for the sphere. Between these two regimes is the Mie resonance region, where for the case of the sphere, there exists a one-to-many mapping between a given RCS value and the size of the sphere. In the case of the size estimation model there is a one-to-one relationship between a given RCS and the size of the object, as shown in Figure 3-15.

For more details on the piecewise function definition of the SEM or scaling curve from Figure 3-15, see [14].

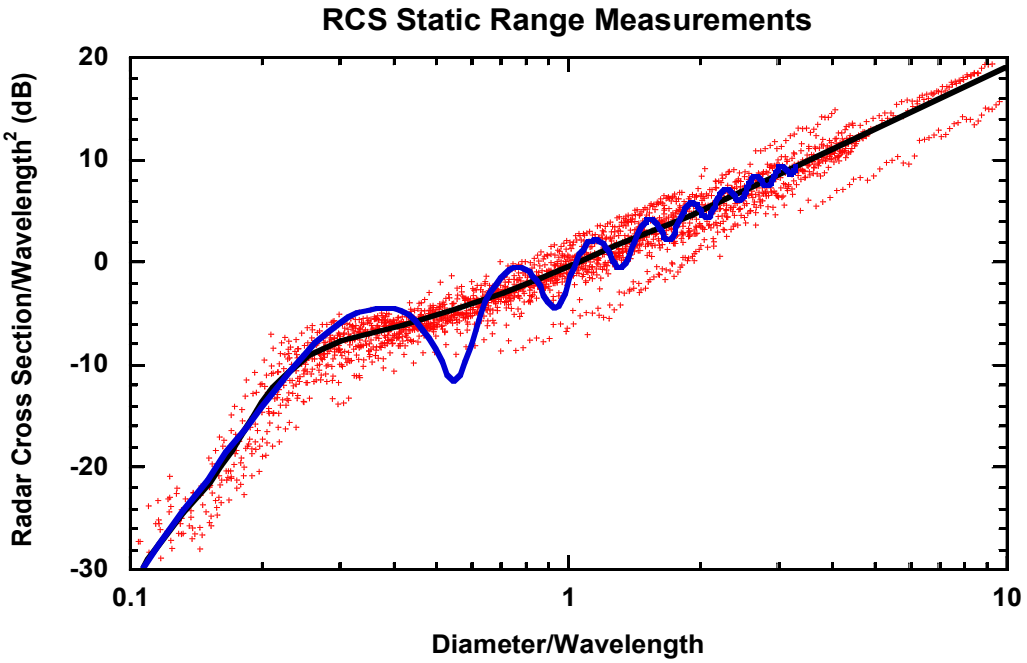

Figure 3-15. Results of RCS-to-size measurements on 39 representative debris objects (red +). The oscillating blue curve is the RCS for a spherical conductor while the smooth black curve is the polynomial fit to the data.

Data provided by Goldstone has a differently calculated size estimate for objects passing through the beam. To estimate OD particle size, Goldstone compares the RCS to that of an equivalent sphere of large dielectric constant using either the geometric cross section for larger debris or the Rayleigh cross section for smaller debris [4]. Figure 3-16 compares the NASA SEM and the SEM used by JPL. Size estimates presented in this report use the NASA SEM rather than size estimates provided by Goldstone.

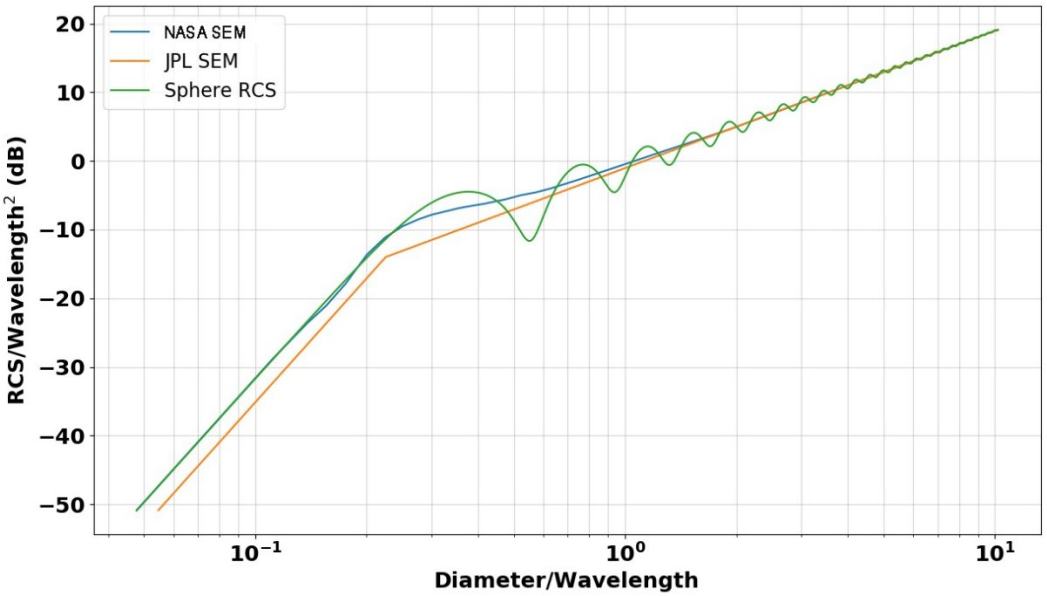

Figure 3-16. NASA SEM (blue) and JPL SEM (orange), plotted with the sphere scattering curve (green).

4.0 Results

After ODPO's data quality processing, a total of 30 hours and 801 detections for CY2020–2021 remained out of the 102 hours of data provided by Goldstone. Table 4-1 shows the number of observation hours and the total number of detections remaining.

Table 4-1. Remaining Number of Hours, Detections, and Count Rate for the Different Pointings Used in CY2020–2021 After ODPO Data Quality Check and Processing

Year	ID	Number of Hours	Total # of detections	Count Rate (#/hr)
2020–2021	A	4.2	99	23.4
2020–2021	B	10.2	268	26.2
2020–2021	C	2.7	68	25.6
2020–2021	D	12.9	366	28.4
Total		**30.0**	**801**	**26.7**

Plots in the following sections compare each of the pointings with each other and with previous years of data. Appendix C through Appendix G have a comprehensive set of interdependent charts for each of the A, B, C, D, and 800 km pointings, respectively.

4.1 RADAR MEASUREMENT PLOTS

4.1.1 *Range versus Range-Rate and Altitude versus Doppler Inclination*

Range and range-rate are two of the fundamental measurements made by the radar. The range definition used in this report is the distance from the target to the point on a line connecting the transmitter and receiver; defined by the bisection of the angle subtended between the transmitter, target, and receiver, or bistatic angle. Range-rate is a measurement of the velocity of the target along the line connecting the target to the point on a line connecting the transmitter and receiver, defined by the bisection of the bistatic angle, as shown in Figure 4-1. It is calculated from the Doppler shift of the received signal. Figure 4-2 presents the calculated range plotted against the range-rate for the Goldstone CY2020–2021 data. The data forms distinct clusters in range and range-rate.

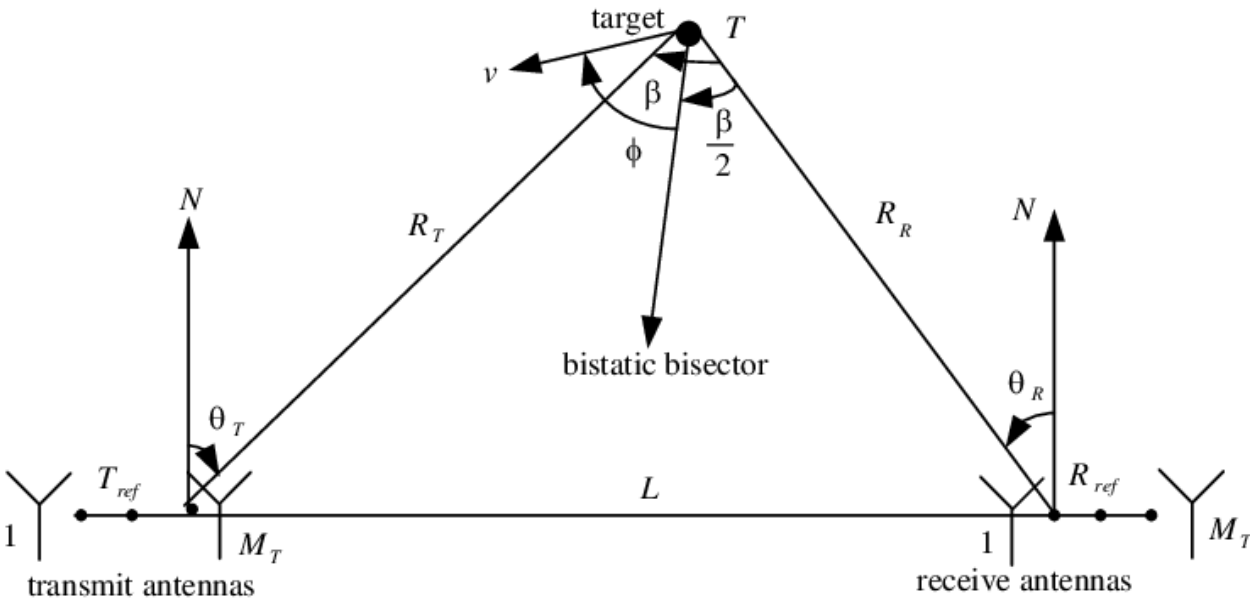

Figure 4-1. Bistatic radar geometry [15].

An object's inclination (referred to as Doppler inclination) and orbital altitude can be estimated using measurements of range and range-rate and assuming a circular orbit. Doppler inclination allows identification and study of various orbital families. Figure 4-3 shows the orbit altitude versus Doppler inclination for the Goldstone CY2020–2021 data. When viewed this way, several debris families can be identified, the largest of which is the heavily trafficked sun-synchronous orbits clustered about the black dashed curve that represents the sun-synchronous inclinations for circular orbits. Several notable on-orbit fragmentation events are highlighted by black circles, where the center of each circle denotes the altitude and inclination of the parent body at the time of the event. Additionally, a grouping of detections associated with the Starlink constellation at 53° inclination is indicated by a black ellipse.

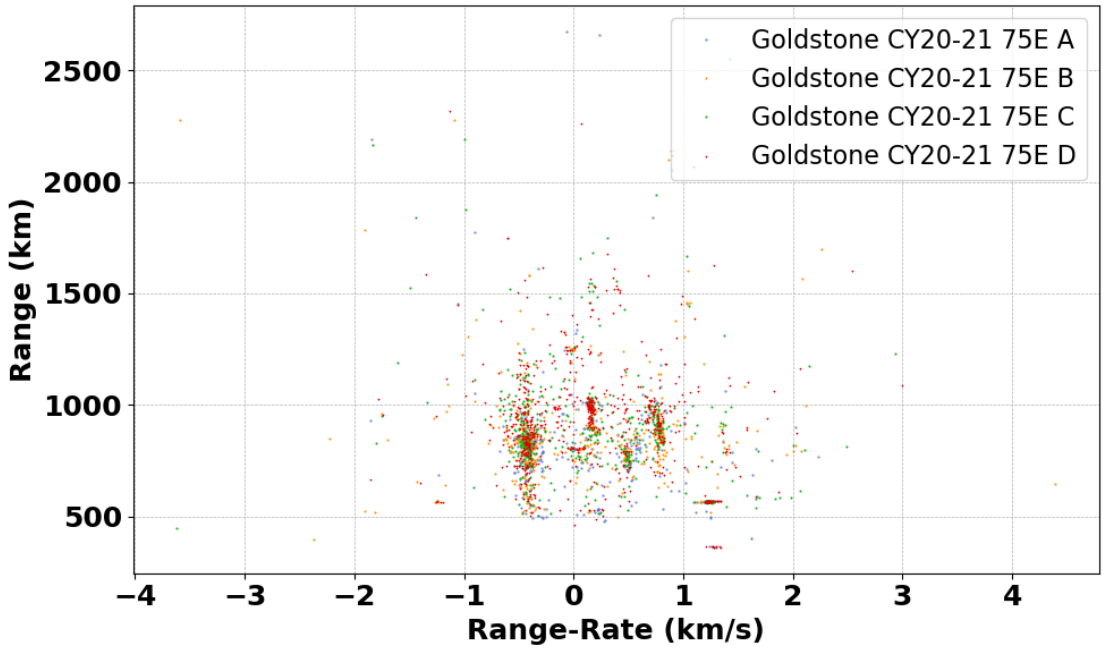

Figure 4-2. Range versus range-rate plot for Goldstone CY2020–CY2021.

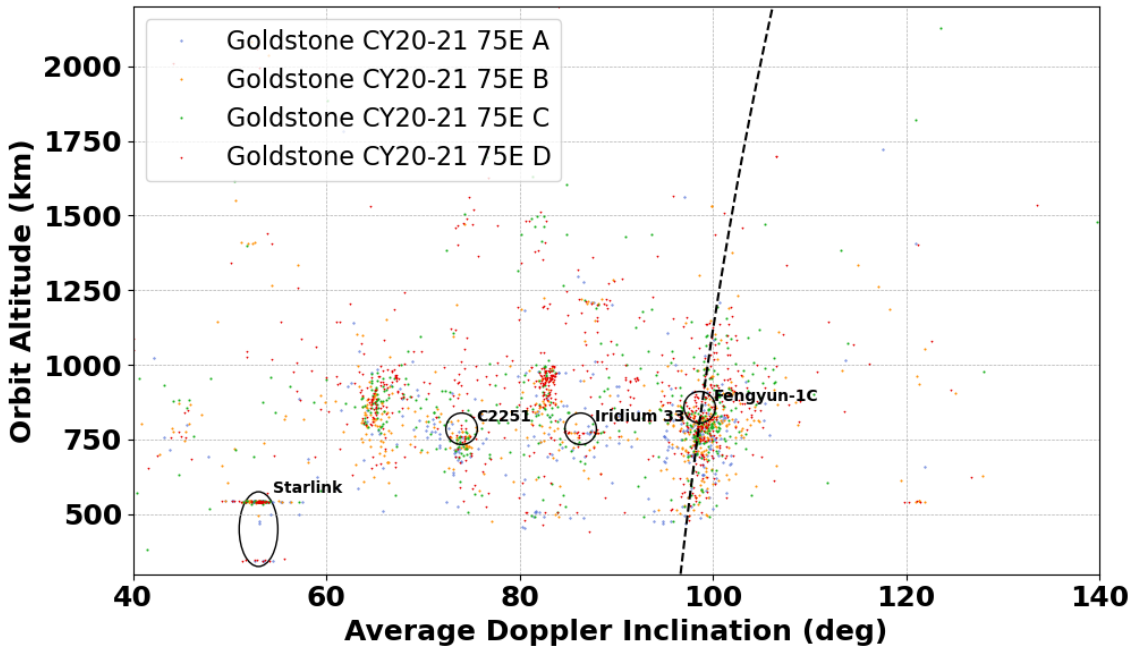

Figure 4-3. Orbit altitude versus average Doppler inclination for Goldstone CY2020–2021.

4.1.1 *Range versus RCS and Orbit Altitude versus SEM Size*

RCS is another key measurement made by the radar, in addition to range and range-rate. Figure 4-4 shows the range versus total RCS for Goldstone CY2020–2021. The RCS is calculated using the bistatic radar range equation,

$$\sigma = \frac{P_r (4\pi)^3 R_t^2 R_r^2}{P_t G_t G_r \lambda^2}$$

where R_t and R_r are the range to the transmitter and range to receiver, respectively, which are calculated using the assumption that the detection occurs on the transmitter boresight because the beam of the transmitter is narrower than the receiver beam. Within the 700 km to 1000 km target altitudes, the combined data from each pointing collectively exhibit the expected $\frac{1}{R^4}$ trend typically observed in datasets that cover large ranges in a single pointing. The RCS is related to size using the NASA SEM. Figure 4-5 shows orbit altitude versus SEM size for Goldstone CY2020–2021.

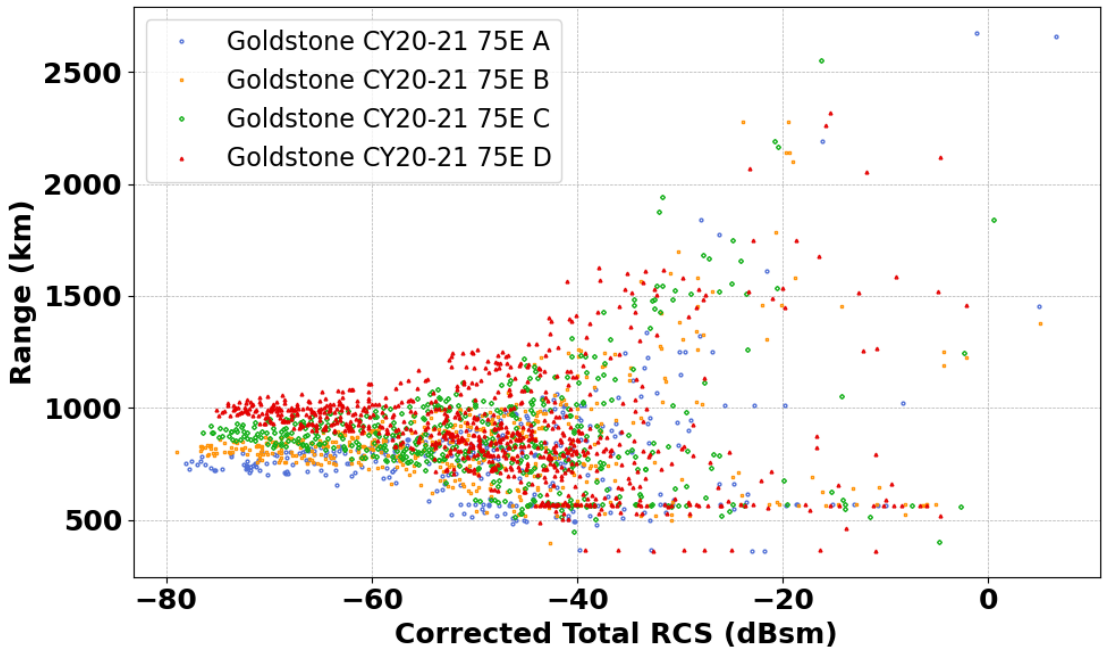

Figure 4-4. Range versus total RCS for Goldstone CY2020–2021.

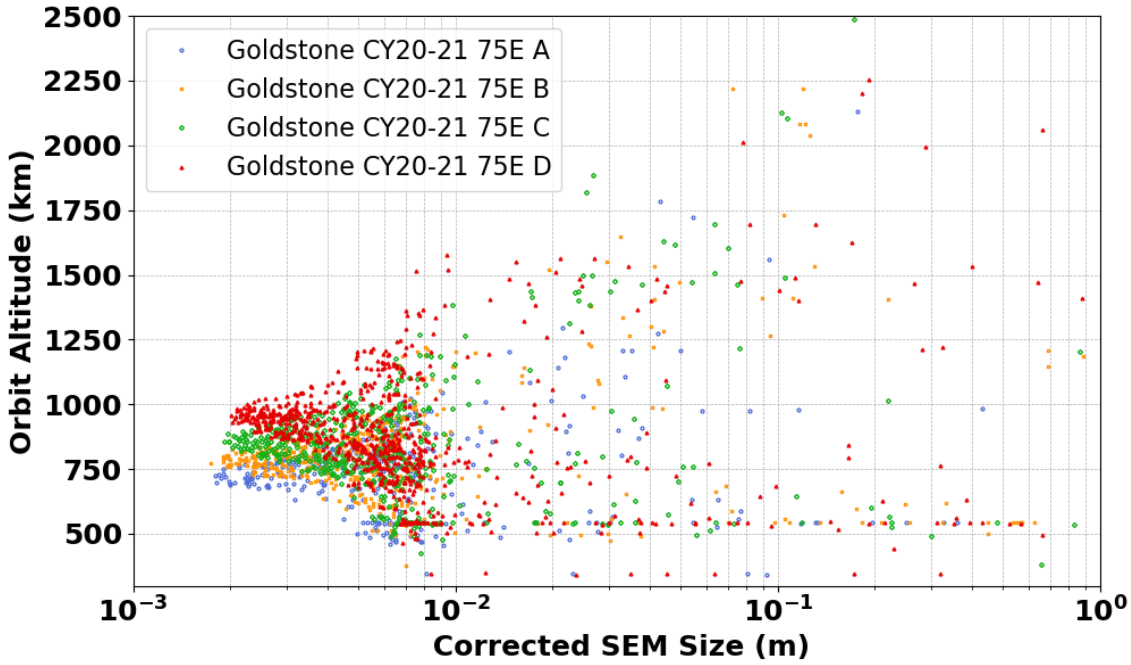

Figure 4-5. Orbit altitude versus SEM size for Goldstone CY2020–2021.

4.1.2 *Polarization Distribution*

Polarization is calculated from the PP RCS and OP RCS and is defined as follows, where RCS_{PP} and RCS_{OP} are in linear units.

$$P = \frac{RCS_{PP} - RCS_{OP}}{RCS_{PP} + RCS_{OP}}$$

Polarization can provide a rough indication of the shape of an object. A perfectly conducting sphere would show a polarization of +1, since it only has a PP response. A dipole-like object would reflect energy equally into both the PP and OP channels exhibiting a polarization of zero. Figure 4-6 shows the polarization distribution of the B pointing of CY2020–2021 data limited to the altitudes of the main beam overlap and sizes larger than 3 mm. It exhibits similar behavior to data from CY2016 and CY2017 with a peak of highly polarized detections, a roughly flat distribution of positively polarized detections, and a trend of decreasing counts toward more negative polarizations.

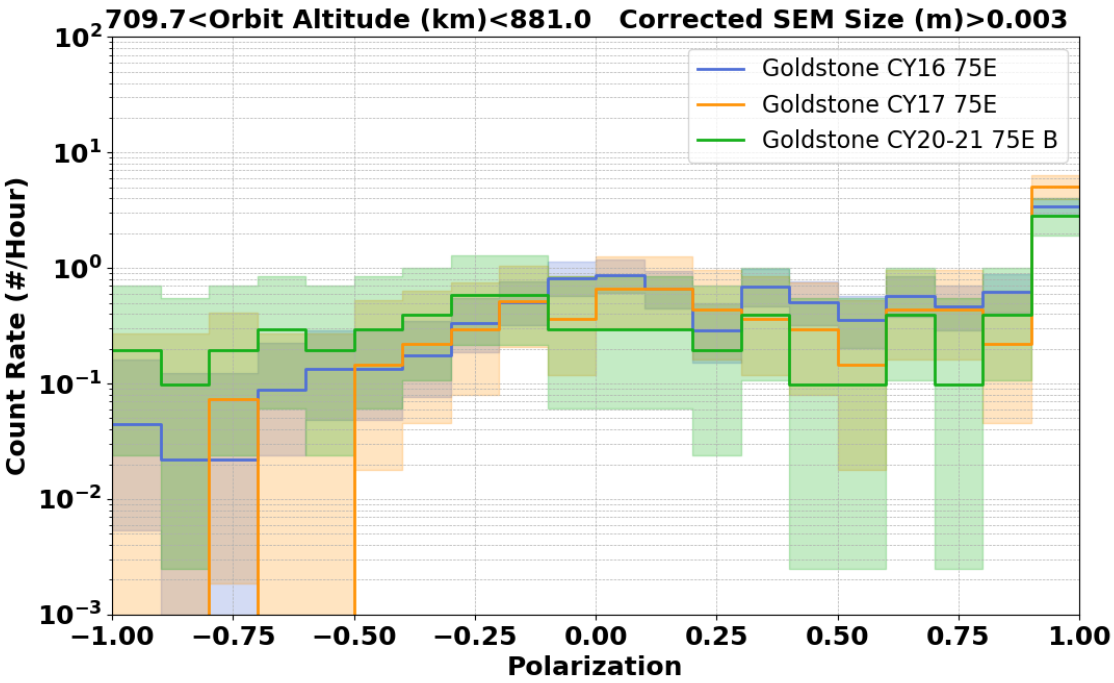

Figure 4-6. Count rate versus Polarization for CY2020–2021, limited to the beam overlap altitudes of the B pointing and sizes larger.

4.2 ENVIRONMENT CHARACTERIZATION SUMMARY

4.2.1 *SEM-Size Cumulative Distribution*

Total debris count rate can change from year to year, due to changes in radar sensitivity; however, the shape of the distributions for sizes larger than the limiting size each year is similar. A meaningful change in the OD environment may manifest as large changes in the count rate from one year to the next, or significant changes to the size distribution. Figure 4-7 shows the count rate versus SEM size between Goldstone CY2016, CY2017, and CY2020–2021, at the A, B, C, and D pointings. All except the C pointing, which had the fewest observation hours, compare well to previous years of data.

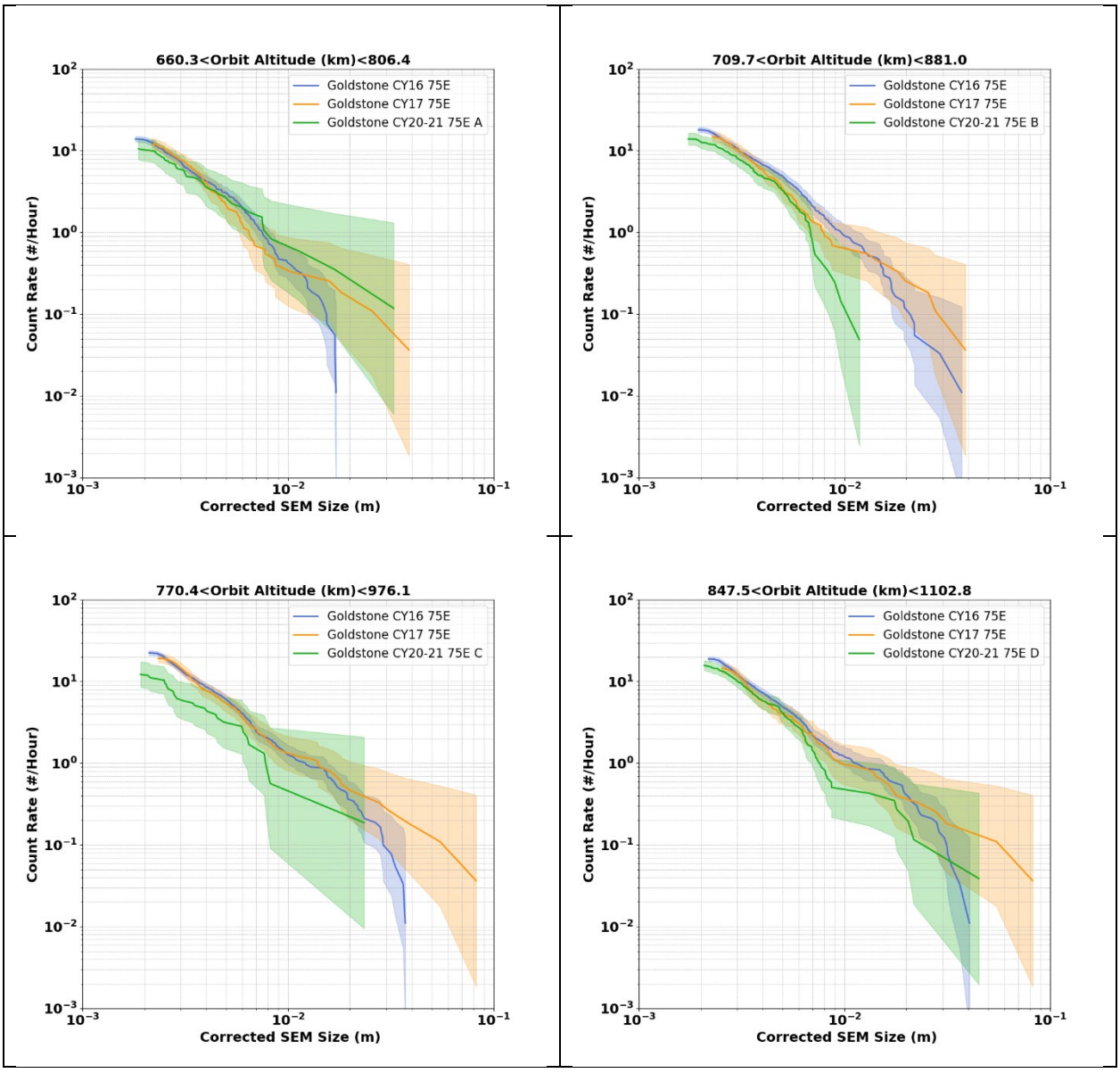

Figure 4-7. The cumulative count rate versus SEM size between Goldstone CY2016, CY2017, and CY2020–2021, at the A, B, C, and D pointings.

4.2.2 *Flux versus Altitude*

Flux is defined as the number of detections through the lateral surface area of the radar beam, considering width of the main beam only, within a given period. The main beamwidth is taken as the beamwidth of the product of the transmitter and receiver beams and is approximately 0.037°. Total flux is the flux of all objects regardless of NASA SEM size. To aid in comparing flux in different years, which may show different sensitivities, surface area flux to a limiting size is used. Figure 4-8 shows the flux versus orbit altitude between Goldstone CY2016, CY2017, and CY2020–2021, at the A, B, C, and D pointings limited to sizes 3 mm and larger. The vertical dashed black lines represent the upper and lower limits of the main beam overlap for each

pointing. Within the main beam overlap, most altitude bins are within relative uncertainties. The increase in the 500 km to 550 km altitude bin for all pointings, while outside the main beam overlap, is statistically significant relative to previous years and is attributed to the increase in the number of Starlink constellation spacecraft.

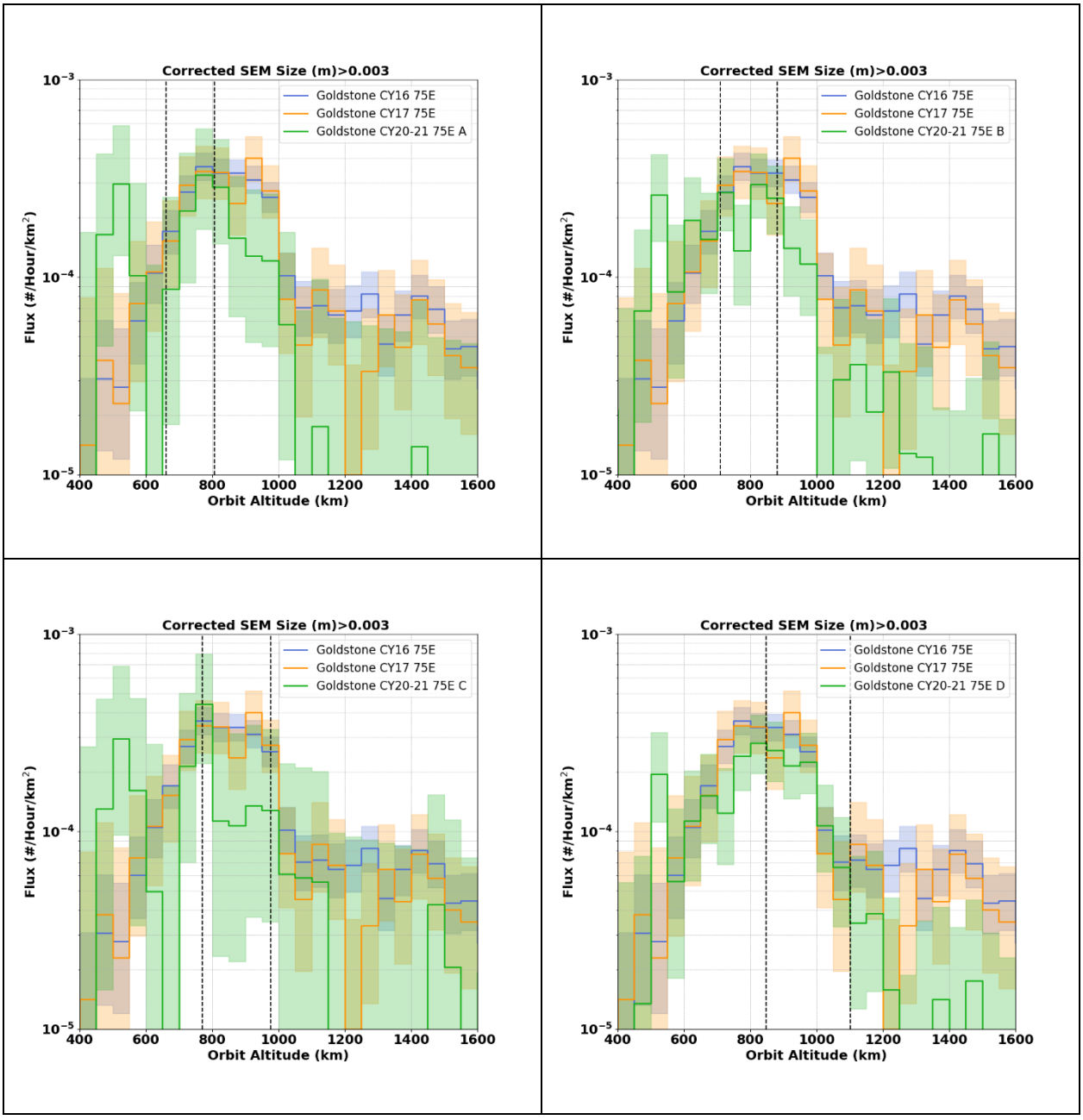

Figure 4-8. The flux versus orbit altitude between Goldstone CY2016, CY2017, and CY2020–2021, at the A, B, C, and D pointings.

4.2.3 *Flux versus Inclination*

Examining flux versus inclination gives more insight to the distinct populations and families of debris. The surface area flux is presented within the orbit altitude window of the main beam

overlap for each pointing. Figure 4-9 shows the flux versus average Doppler inclination between Goldstone CY2016, CY2017, and CY2020–2021, at the A, B, C, and D pointings limited to sizes 3 mm and larger. When limited to the main beam overlap, most inclination bins are within their relative uncertainties.

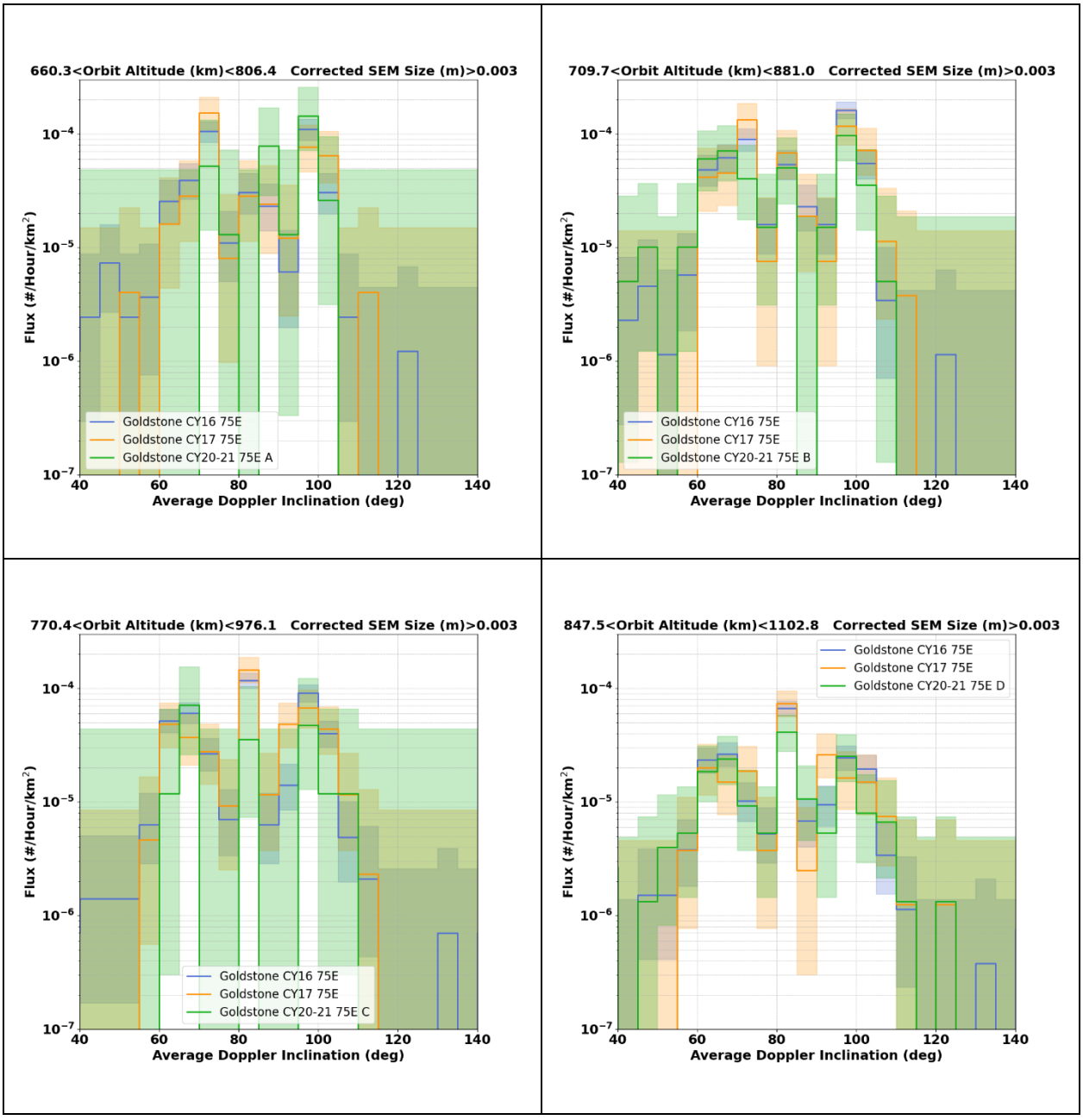

Figure 4-9. Flux versus average Doppler inclination between Goldstone CY2016, CY2017, and CY2020–2021, at the A, B, C, and D pointings.

4.2.4 *HUSIR Comparisons*

Comparisons to HUSIR CY2021 75E data are made to verify the Goldstone data against contemporaneous data from an independent sensor. Cumulative flux comparisons take the

cumulative count rates for each sensor within the altitude window covered by Goldstone CY2020–2021 and divide each by the total lateral beam surface area between those altitudes. The beam for each sensor is modeled as a cone, with the two-sided 3 dB beam width forming the cone angle. As seen in Figure 4-10, the HUSIR CY2021 and Goldstone CY2020–2021 datasets match within their respective uncertainties in all pointings down to the limiting size of HUSIR (approximately 5.5 mm), and when limited to the altitudes of the beam overlap for each pointing. The apparent difference in slope at larger sizes for pointing B is likely due to a low number of counts, though the curves still overlap within the 2σ Poisson uncertainties.

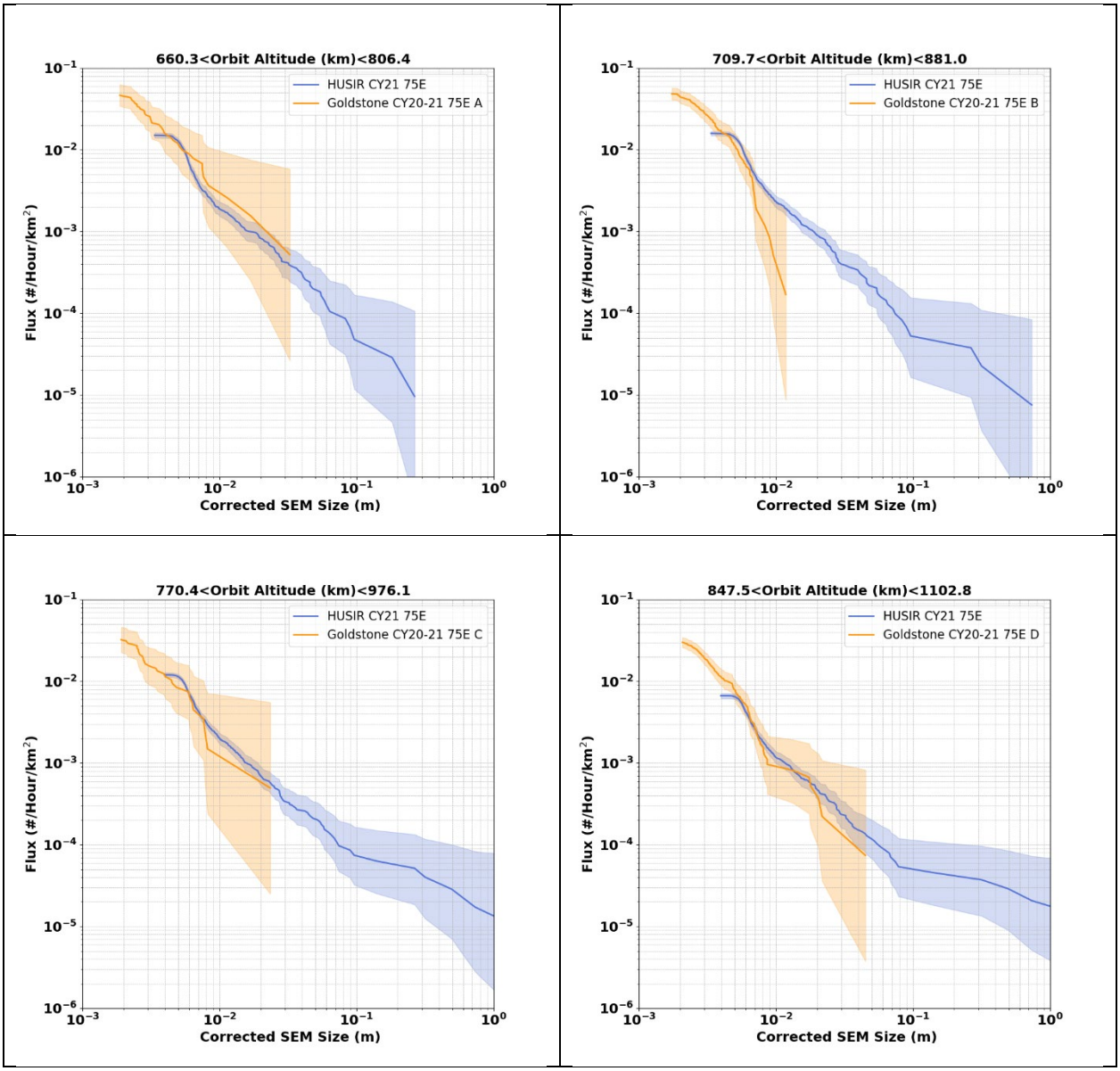

Figure 4-10. The cumulative flux versus SEM size comparisons for HUSIR CY2021 and Goldstone CY2020–2021 datasets in all pointings.

4.3 SPECIAL DATASETS

4.3.1 *DSS-13/DSS-28 Experimental Data*

During CY2020 while DSS-14 was offline for maintenance, two experimental observations were performed using DSS-13 as a transmitter and DSS-28 as a receiver [4]. The baseline between DSS-13 and DSS-28 is approximately 1.7 km, significantly smaller than the approximately 10 km baseline of the current DSS-14/DSS-25 configuration. For these observations, DSS-13 was pointed at 75E, like DSS-14, and DSS-28 was pointed such that the transmitter and receiver beams intersected at 800 km slant range from DSS-13. With this pointing, the reduced baseline resulted in the antennas having a null-to-null beam overlap that covered all of LEO. Additionally, the -6 dB overlap covered approximately 480 km to 1910 km in altitude.

Figure 4-11 shows the normalized peak gain product of the DSS-13/DSS-28 pair in the described geometry as a function of altitude illustrating the beam overlap. Additionally, the beam overlap of both the legacy system with DSS-14/DSS-15 and the four pointings currently employed with DSS-14/DSS-25 (A, B, C, and D) are shown. While not as large as the legacy overlap, this experimental configuration has significantly more overlap than the current configuration.

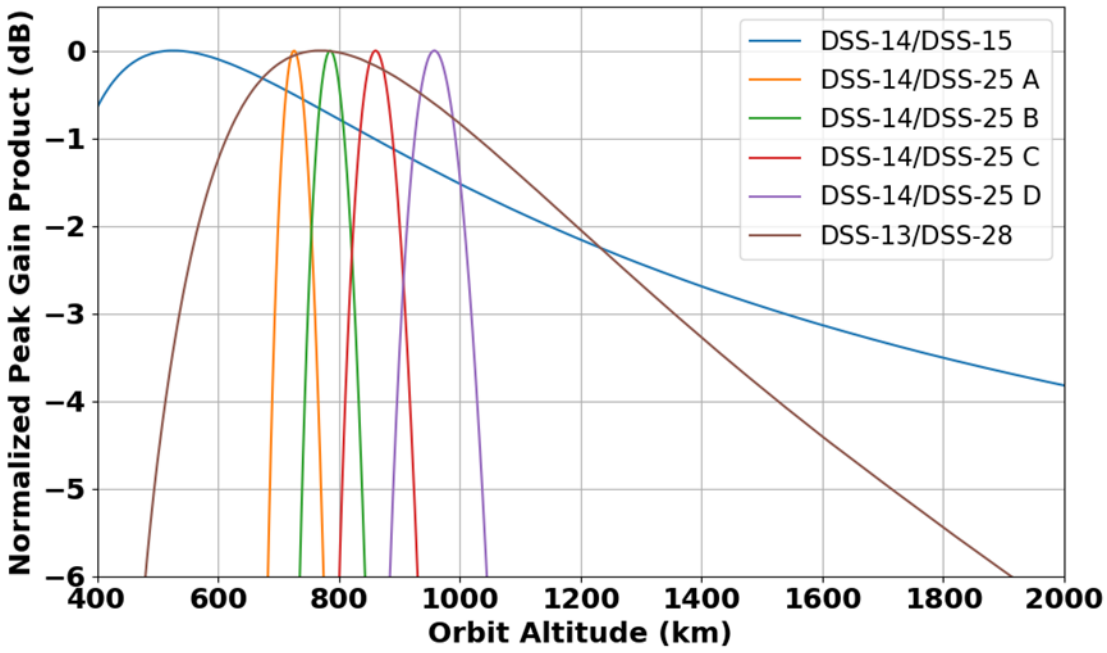

Figure 4-11. Peak gain product versus altitude for the DSS-14/DSS-15, DSS-14/DSS-25 (A, B, C, D), and DSS-13/DSS-28 antenna pairs.

Although the beam overlap is larger, the DSS-13/DSS-28 configuration has drawbacks. The receiver can only record the PP channel, which increases uncertainty in the computed RCS and precludes the discrimination of on-orbit sodium-potassium droplets. These were used successfully as an ad-hoc calibration source in CY2016 and CY2017 [16]. Additionally, the transmitter has a smaller dish, a lower transmit power, and a higher system temperature than the standard configuration, all of which reduce the system sensitivity. To simplify setup between the

different systems, the same chirp parameters were used, although with a lower center frequency. Table 4-2 displays the nominal operating parameters for DSS-14/25 and DSS13/28.

Table 4-2. Radar System Hardware Nominal Operating Parameters

Operating Parameter	DSS-14/DSS-25	DSS-13/DSS-28
Peak Power (kW)	440	80
Transmitter Frequency (GHz)	8.56	7.15
Transmitter Wavelength (cm)	3.502	4.193
Transmitter Antenna Diameter (meter)	70.0	34.0
Receiver Antenna Diameter (meter)	34.0	34.0
Transmitter HPBW (deg)	0.03	0.07*
Receiver HPBW (deg)	0.06	0.07*
Transmitter Antenna Gain (dB)	74.24	66.86**
Receiver Antenna Gain (dB)	68.42	66.86**
Avg. System Temperature (K)	21.79	41.0
*HPBW derived by linear frequency scaling of DSS-25 HPBW **Gain derived from frequency scaling DSS-25 gain by $20\log_{10}\frac{f_0}{f}$		

This experimental dataset did not have sufficient data to confidently find a completeness size. Analyzing the differences between relevant parameters in Table 4-2 provides an estimation of the experimental setup sensitivity relative to the current Goldstone configuration. Accounting for changes in peak power, center frequency, transmitter and receiver gains, and system temperature, the total sensitivity reduction of the experimental setup relative to the current configuration is approximately 23.7 dB. By scaling the completeness size of 2.2 mm at 1000 km altitude as determined for the CY2020–2021 dataset by 23.7 dB, a rough estimate of 6.5 mm is obtained for the DSS-13/DSS-28 dataset. A breakdown of the individual contributions of each parameter is shown in Table 4-3.

Table 4-3. Sensitivity Reduction of the DSS-13/DSS-28 Configuration Relative to DSS-14/DSS-25 for Each of the Relevant Operating Parameters

Operating Parameter	Sensitivity Reduction (dB)
Peak Power	7.4
Transmitter Frequency	1.6
Transmitter Antenna Gain	10.4
Receiver Antenna Gain	1.6
Avg. System Temperature	2.8
Total	**23.8**

Two observations were performed with this experimental setup. A total of 188 detections were recorded over 11.8 hours of observation for an average count rate of 15.9 per hour. Table 4-4 shows observation hours, detections, and count rate for each observation.

Table 4-4. Total Number of Hours, Detections, and Count Rate for DSS-13/28 Special Dataset

DOY	Number of Hours	Total # of detections	Count Rate (#/hr)
65	5.5	97	17.5
132	6.3	91	14.5
Total	**11.8**	**188**	**15.9**

Comparisons to HUSIR data taken in CY2020 were made to evaluate the data obtained from this experimental setup. Figure 4-12 shows the cumulative flux versus SEM size for this data compared to HUSIR CY2020 75E data. There is agreement between the two datasets at smaller sizes. Discrepancies at mid-range sizes may be related to the fewer hours collected in this configuration, a data calibration issue, and/or the effects of detections near the edge of the beam. A major result is that the sensitivity of the DSS-13/DSS-28 configuration is comparable to that of HUSIR, since the cumulative flux distributions roll off at similar sizes. This is consistent with the rough estimate of 6.5 mm for the DSS-13/DSS-28 configuration being close to the 6 mm estimated for the HUSR CY2020 75E dataset [5]. Without sensitivity improvements, this configuration cannot replicate the small-size sensitivity performance that made the Goldstone system a valuable complementary sensor to ODPO's workhorse, HUSIR, but data of similar sensitivity from an independent sensor can still be useful for validation purposes.

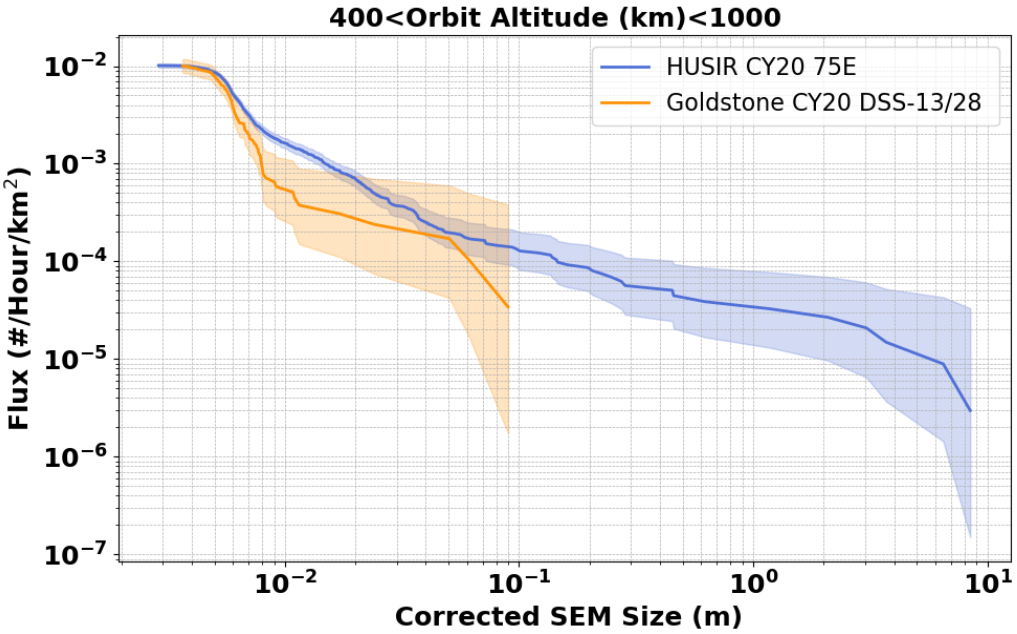

Figure 4-12. Flux versus SEM size HUSIR CY2020 and Goldstone CY2020 comparison.

Figure 4-13 shows the surface area flux versus altitude of the DSS-13/DSS-28 data compared to HUSIR CY2020 75E data, using 50 km-wide bins and limited to objects 6 mm and larger. The 6 mm limit was chosen since the experimental data closely matches the HUSIR data at smaller sizes and there is higher confidence in the HUSIR size limit estimation. For almost all altitudes, the fluxes are within their relative confidence intervals. Figure 4-14 shows the surface area flux versus inclination of the DSS-13/DSS-28 data compared to HUSIR CY20 75E data, using 5 degree-wide bins and limited to objects 6 mm and larger and altitudes from 400 km to 1000 km. Again, the confidence intervals overlap for almost all inclination bins.

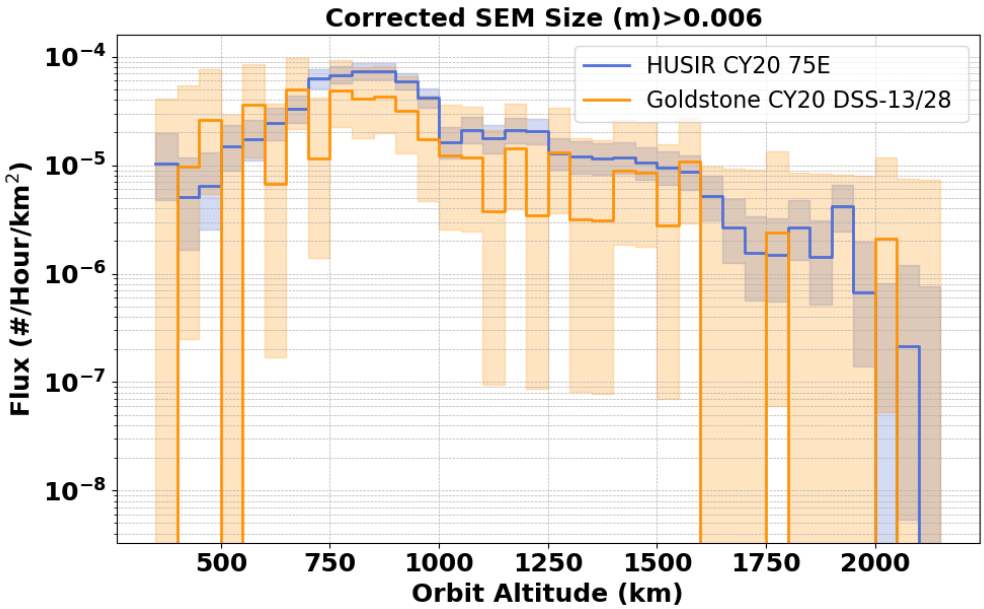

Figure 4-13. Flux versus altitude HUSIR CY2020 and Goldstone CY2020 comparison.

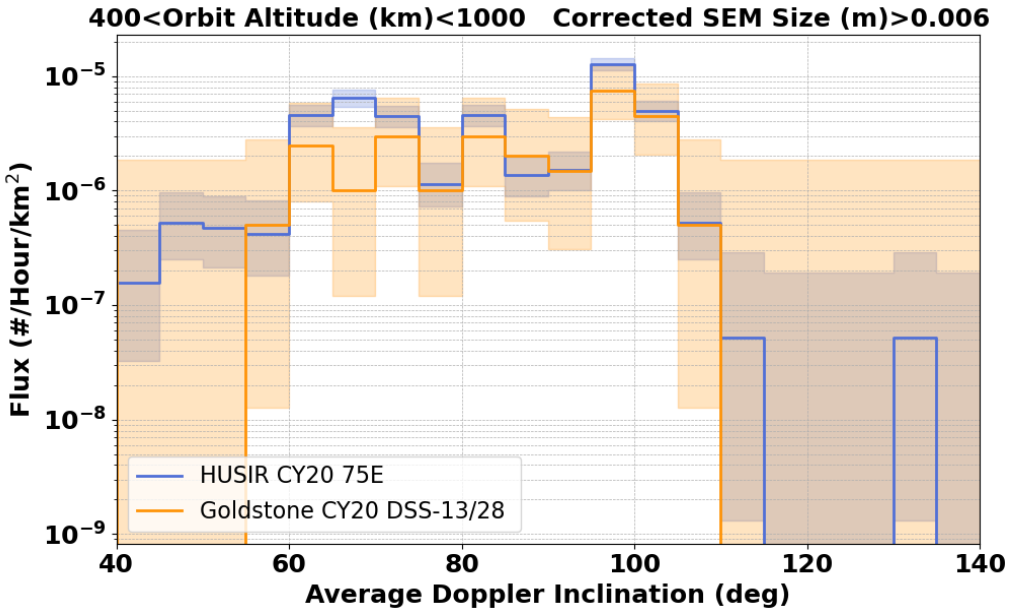

Figure 4-14. Flux versus average Doppler inclination for HUSIR CY2020 and Goldstone CY2020.

4.3.1.1 *Ad-Hoc Uniform RCS Calibration Estimation*

A rough calibration was attempted to improve the cumulative flux versus size comparison at sizes > 7 mm. Uniform RCS calibration factors were added in 1 dB increments from 1 dB to 5 dB, and the resulting cumulative flux versus size distributions were compared to HUSIR data. Figure 4-15 shows the results for each of the 1 dB increments, increasing from left-to-right and top-to-bottom. While a calibration factor between 2 dB and 3 dB provides the best match at smaller sizes, a uniform RCS correction is insufficient to match cumulative flux at larger sizes. Most likely, a more sophisticated calibration method is needed to achieve a match at all sizes.

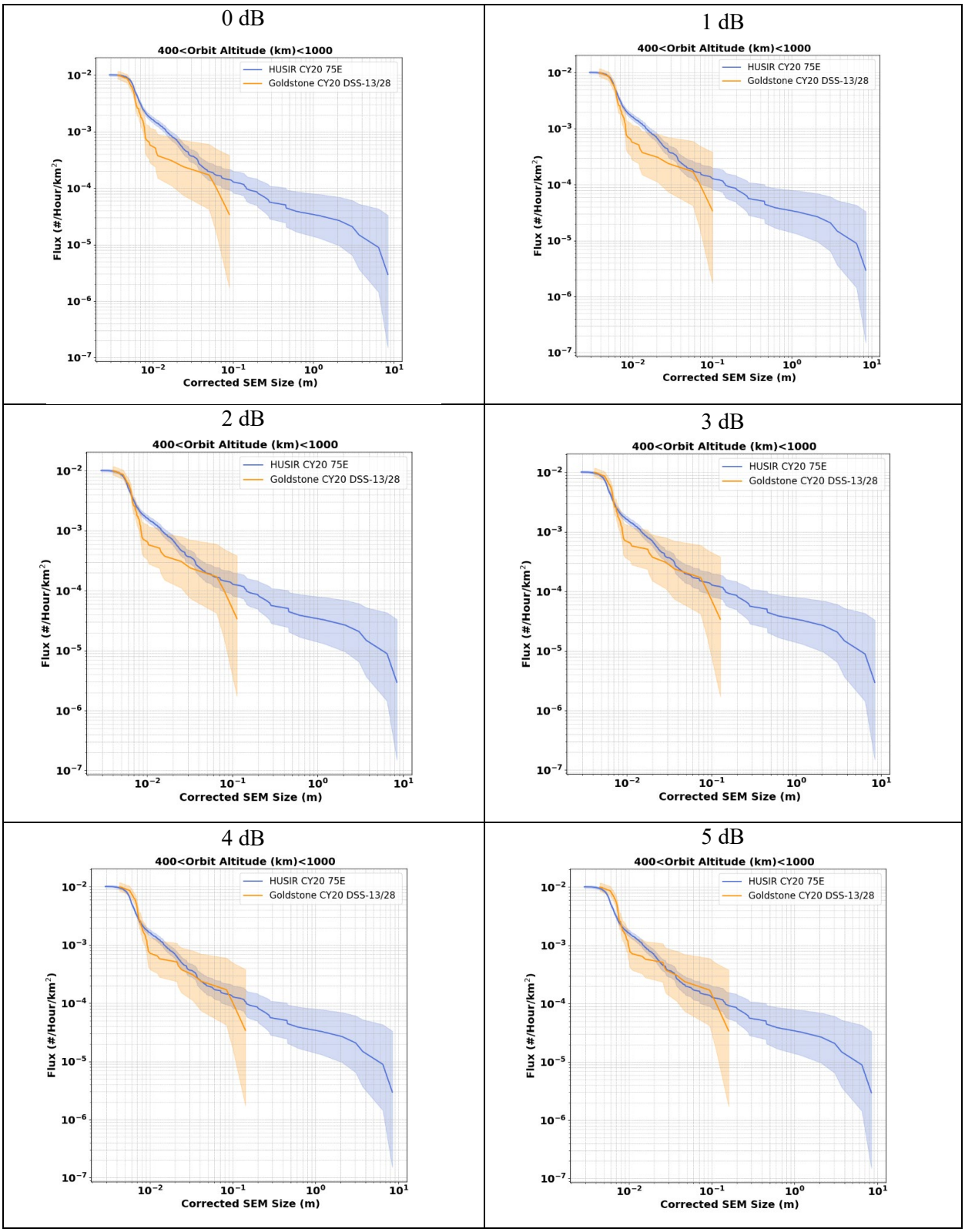

Figure 4-15. Flux versus SEM size in incremented dB calibration constants for Goldstone CY2020, compared to HUSIR CY2020 data.

4.3.2 *Cosmos 1408 ASAT*

On 15 November 2021, Russia conducted a direct ascent ASAT test that caused the breakup of the Cosmos 1408 spacecraft. The spacecraft (a Soviet electronic and signals intelligence Tselina-D-class) was launched into a 666 × 636 km altitude, 82.6-degree inclination orbit in 1982 but had decayed to a 490 × 465 km altitude orbit. The ASAT test produced more than 1500 large fragments immediately trackable by the U.S. Space Surveillance Network (SSN) [17]. Because the resulting cloud could endanger other satellites in LEO, ODPO requested measurements of debris too small to be tracked by the SSN from the Goldstone and HUSIR radars. Data collection began within a day of the event and was collected for 25 days.

Measurements were taken at times corresponding to expected passes of the resulting debris cloud through the beam of the radar. Candidate windows (times where satellite orbits passed through the radar beam at 75E geometry) were identified using Satellite Trajectory and Attitude Kinetics software. Fragments of the breakup cloud were modeled by the NASA Standard Satellite Breakup Model (SSBM) and then propagated to the time of the candidate observation window. A detailed description of the SSBM can be found in [18].

The beam overlap as a function of range from DSS-14 was calculated for several target altitudes around the breakup altitude of Cosmos 1408. The optimal pointing was that for which the largest fraction of the cloud passed within the bistatic radar beam overlap. The optimal intersection altitude for the observations was approximately 472 km, close to the altitude at which the breakup is estimated to have occurred. Figure 4-16 shows the normalized peak gain product of DSS-14 and DSS-25 as a function of orbit altitude illustrating the bistatic beam overlap, where the vertical dashed black lines show the upper and lower altitude limits of the nearly 64 km-wide overlap.

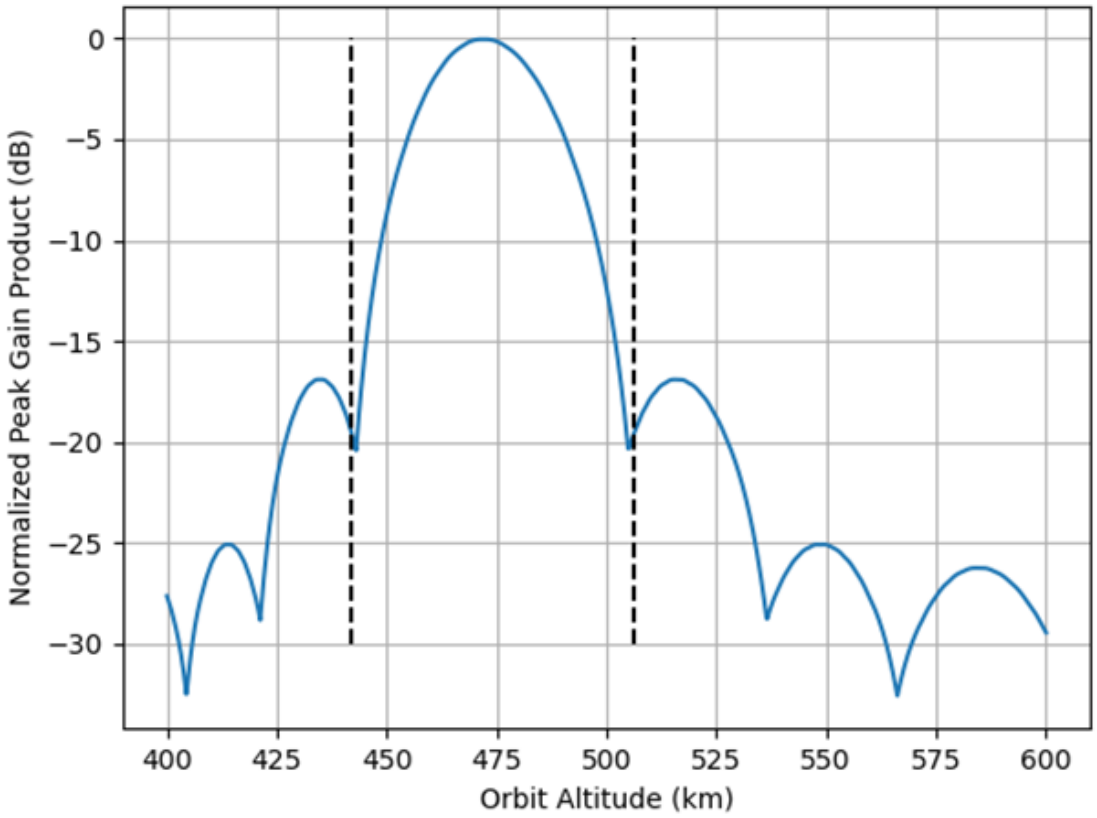

Figure 4-16. Normalized peak gain product of DSS-14 and DSS-25 versus altitude illustrating the bistatic beam overlap. Vertical, dashed black lines indicate the lower and upper altitude limits of the overlap.

Figure 4-17 shows the modeled range-time distribution of the Cosmos 1408 debris cloud for a candidate window on DOY 346 as detected by Goldstone. Start and stop times are shown by vertical red lines. The beam overlap extent is indicated by the black dotted line. With both the time and altitude limitations, only about 30% of the fragments would have been visible in this example. Even so, Goldstone still gives insight into small size regimes inaccessible to other ground-based radars. Though Goldstone is described in these examples, the same process was used for HUSIR. More observation planning details can be found in [19].

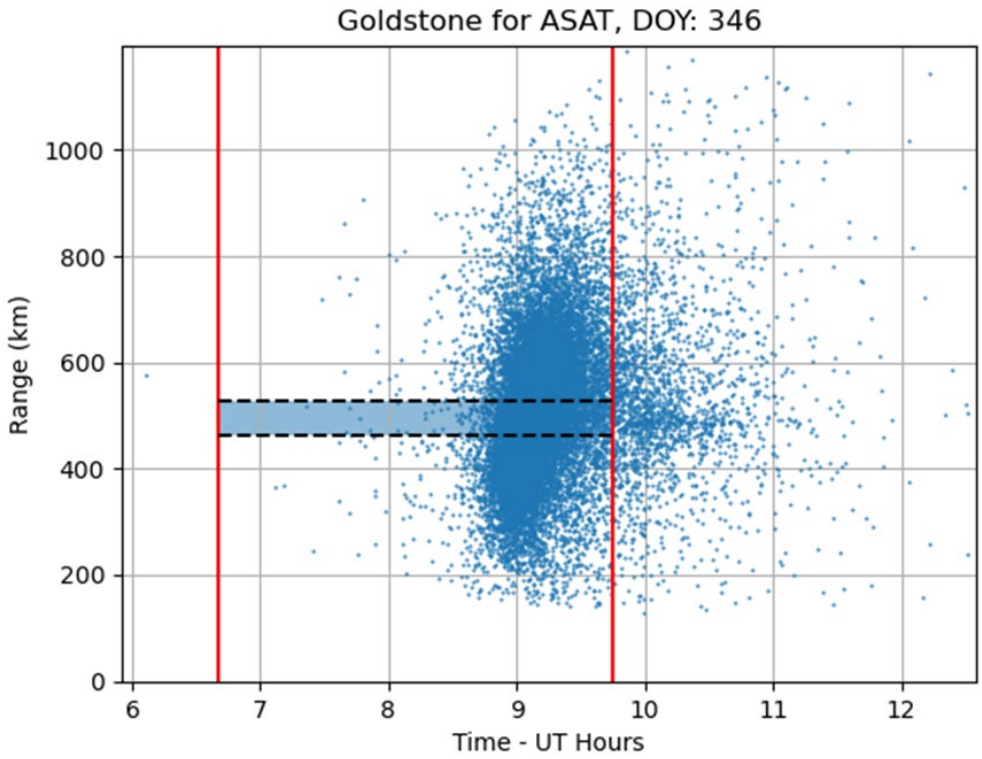

Figure 4-17. Predicted range-time distribution, as detected by Goldstone, of Cosmos 1408 fragments for a candidate observation on DOY 346, highlighting the subset of the range/time space to be measured by Goldstone based on the bistatic beam overlap constraints. The vast majority (> 90%) of the possible detections were predicted to fall within this time window.

Over 11 days, the measurement campaign for Goldstone and HUSIR successfully measured 16 debris cloud passes. Table 4-5 describes the dates of data collection, number of debris cloud passes, debris counts, and observation hours for the radar measurement campaign.

Table 4-5. Summary of HUSIR and Goldstone Measurements for Cosmos 1408 Debris Cloud

Radar	Day of Year (DOY)	Cloud Passes	Detections	Hours
HUSIR	320	2	152	1.40
HUSIR	321	2	163	0.99
HUSIR	322	2	149	1.22
HUSIR	323	2	166	1.02
HUSIR	324	1	79	0.33
HUSIR	325	2	140	1.11
Goldstone	327	1	144	1.48
Goldstone	328	1	104	0.96
HUSIR	341	1	60	0.76
HUSIR	344	1	66	0.84
Goldstone	345	1	77	4.99
Total		**16**	**1300**	**15.1**

Figure 4-18 shows the cumulative count rate versus size of the Goldstone ASAT observations, limited to the approximate null-to-null bistatic beam overlap of the CY2021 ASAT observation geometry. Due to saturation issues, Goldstone cannot effectively measure debris larger than about a centimeter [16]. It was shown in [17] that this data, along with data from other SSN assets, matches the number of fragments predicted by the NASA SSBM across multiple orders of magnitude in size.

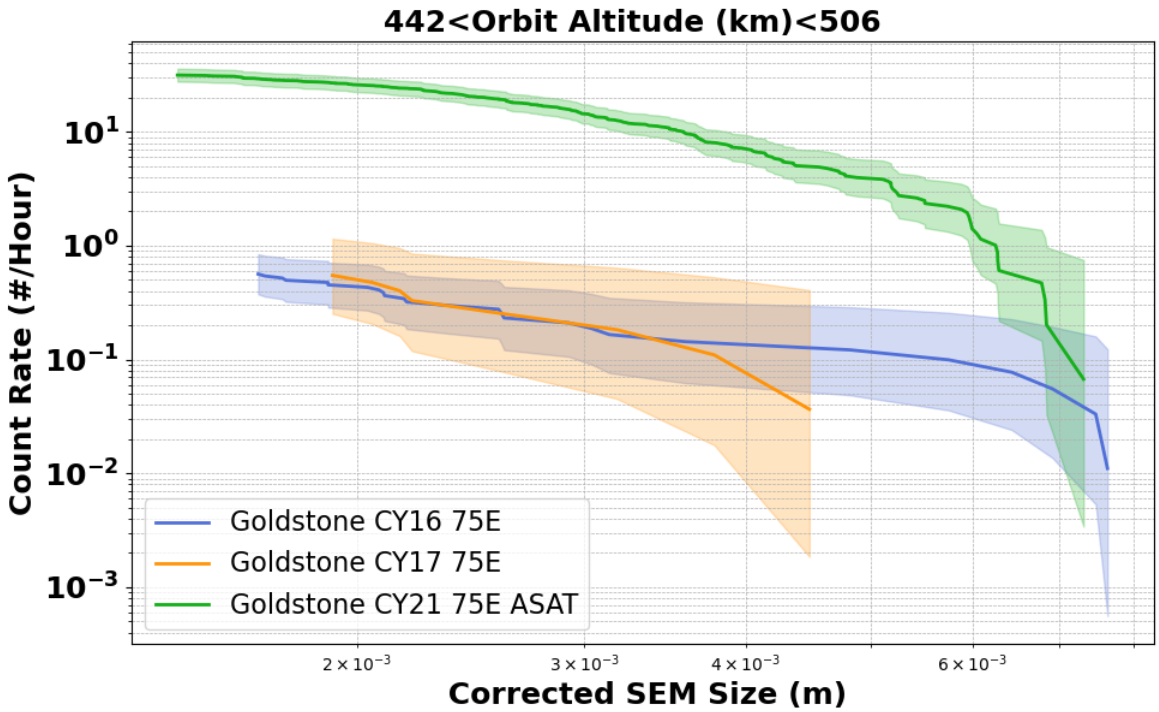

Figure 4-18. Cumulative count rate versus corrected SEM size comparison for Goldstone CY2016–2017 and CY2021 ASAT special observation campaign.

Figure 4-19 shows the surface area flux versus altitude of the Goldstone ASAT observations compared to the background debris environment as measured in CY2016 and CY2017, where the flux is limited to sizes larger than 3 mm. The fluxes presented for the ASAT are derived from observations targeting the fresh breakup debris ring before it dispersed, which deliberately enhance the relative contribution from the breakup. It does not represent the average flux expected from random observations. The highest flux occurs in the 450 km to 500 km altitude bin, corresponding to the altitude at which the breakup occurred. Although the flux is also higher in adjacent altitude bins, the main beam overlap covers little more than the 450 km to 500 km altitude bin. HUSIR measurements showed the flux elevated above background levels from 650 km down to at least 400 km altitude [19]. Figure 4-20 shows the surface area flux versus Doppler inclination of Goldstone ASAT measurements, compared to the background, and limited to the main beam overlap and sizes larger than 3 mm. The flux is elevated above background levels from 75° to 85° inclination, with a peak flux in the 80° to 85° inclination bin, which corresponds to the inclination of the parent body.

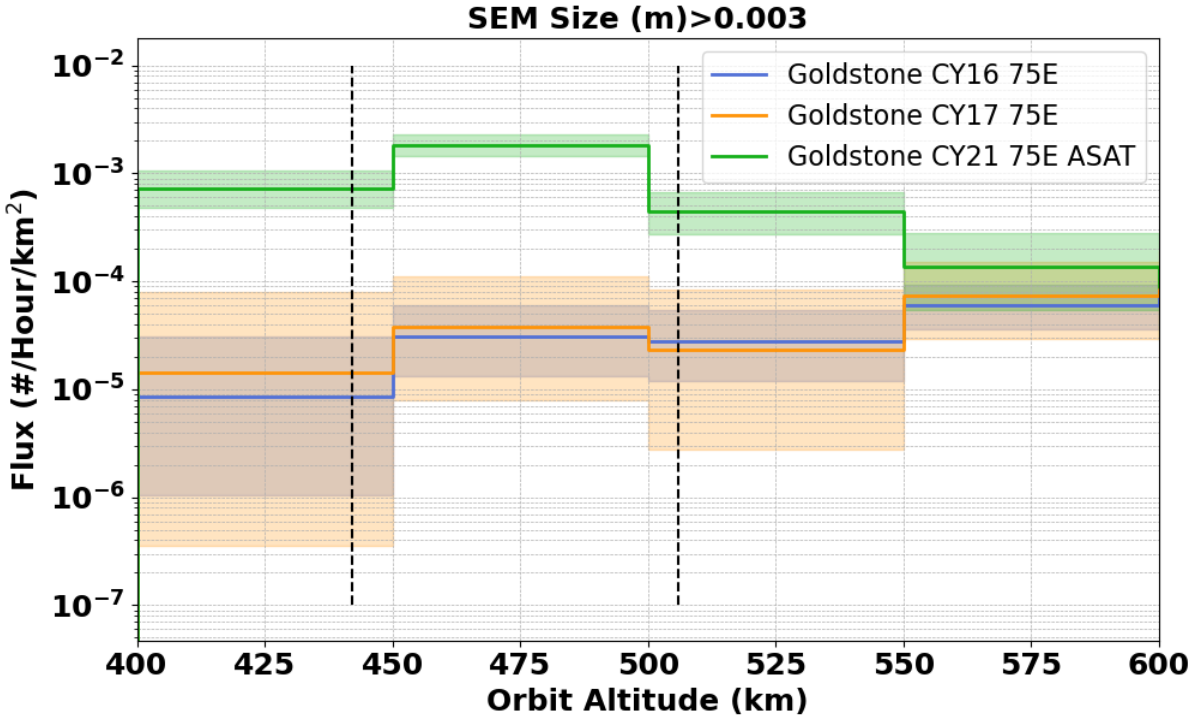

Figure 4-19. Flux versus altitude comparison for Goldstone CY2016–2017 and CY2021 ASAT special observation campaign.

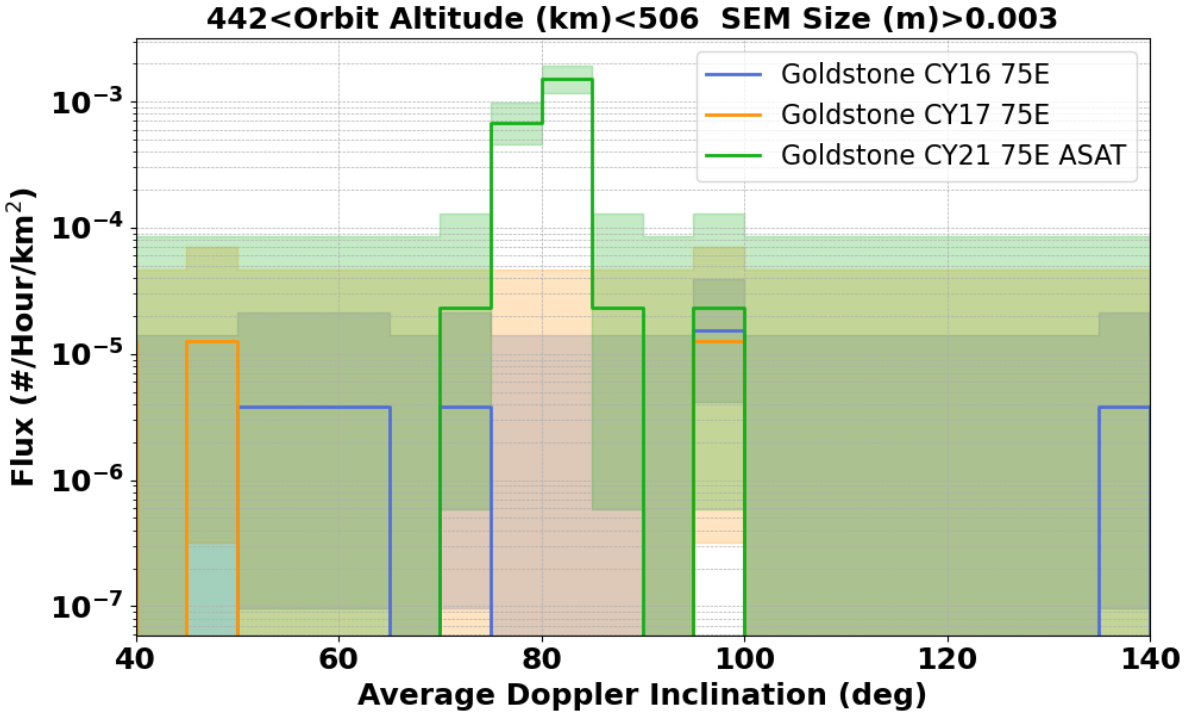

Figure 4-20. Flux versus average Doppler inclination for Goldstone CY2016–2017 and CY2021 ASAT special observation campaign.

5.0 Summary

The LEO environment observed by Goldstone in CY2020–2021 and measurements from the radar were discussed and analyzed. A new pointing plan developed to efficiently sample from 700 km to 1000 km was presented. Changes to radar system parameters, including augmentation of the transmit waveform and receive window were discussed.

A total of 102 observation hours were delivered from the Goldstone radar system and analyzed at four pointing geometries from 700 km to 1000 km. A single observation using the old 800 km pointing was also received but lacked sufficient data to produce statistically significant results. Several data quality checks and corrections were described and implemented including RCS quantization correction, the identification and removal of detections that had significantly different measurements of range and range-rate in the PP and OP channels, and RFI identification. Examination of standard chart sets revealed an issue with the polarization distribution and cumulative count rates of all data taken on and after 30 August 2021. The cause was traced to cable issues that resulted in single-polarization-only data. All affected data were removed from the environment summary charts presented in this report and are being reprocessed.

After quality checks and processing were completed by ODPO, 30 observation hours and 801 detections remained, mostly due to data removed because of polarization distribution issues. These remaining detected objects were measured for RCS, range, range-rate, and polarization, then analyzed to produce orbital altitude and inclination, size, and flux distributions. Cumulative size distributions, surface area flux versus altitude, and surface area flux versus inclination for Goldstone CY2020–2021 were shown to generally agree with results from previous years. Additionally, comparisons of cumulative flux versus SEM size were made to HUSIR data from CY2021 and showed agreement down to the sensitivity roll-off of HUSIR.

Experimental observations performed using DSS-13 as a transmitter and DSS-28 as a receiver were discussed. Although the reduced baseline compared to the DSS-14/DSS-25 configuration increased the beam overlap, the system also had drawbacks, including a single polarization receiver, a smaller transmitter dish, lower transmit power, higher system temperature, and lower center frequency. The resulting reduced sensitivity was comparable to that of HUSIR. Although unable to measure smaller sized debris, contemporaneous data from independent sensors of comparable sensitivity are useful for data validation.

The Cosmos 1408 ASAT test, a major LEO fragmentation event, was discussed. Goldstone conducted a series of special observation campaigns to characterize the portion of the debris cloud too small to be tracked by the SSN, gathering 7.43 hours of data while measuring three passes of the debris cloud on three separate days. The peak flux in altitude and inclination corresponded to the altitude and inclination of the parent body at the time of the event. Along with data from HUSIR, this data matched SSBM predictions across orders of magnitude in size.

This report presented key results from the curated Goldstone CY2020–2021 radar measurements of the OD environment. With the new observation plan, Goldstone can continue supplementing ODPO's HUSIR radar data and providing valuable information on OD in the few-millimeter size regime from 700 km to 1000 km in altitude. Goldstone provides the most sensitive measurements at these altitudes by terrestrial radar to date, improving the sensitivity from 3 mm at 1000 km in CY2017 down to 2.2 mm at 1000 km in CY2020–2021.

6.0 References

[1] S. D. Slobin, "DSN Coverage and Geometry," DSN Handbook, 810-005, 301, Rev. N, 2022.

[2] J. Murray, "A New Geometry for Debris Observations using the Goldstone Orbital Debris Radar," *Orbital Debris Quarterly News,* vol. 23, no. 2&3, p. 8, 2019.

[3] R. Miller, J. Murray and T. Kennedy, "Goldstone Radar Measurements of the Orbital Debris Environment: 2018," NASA/TP-20210015780, 2021.

[4] C. Lee, *et al.*, "Micro-Meteoroid and Orbital Debris Radar from Goldstone Radar Observations," proceedings of the *First International Orbital Debris Conference*, ntrs.nasa.gov/citations/20210015979.

[5] J. Murray and T. Kennedy, "Haystack Ultra-Wideband Satellite Imaging Radar Measurements of the Orbital Debris Environment: 2020," NASA/TP-20220006634, NASA/JSC, Houston, 2022.

[6] K. J. Quirk and M. Srinivasan, "GSSR System Model for Lunar Observations," 2020.

[7] C. Dalquist and G. Bohannon, "Physical Descriptions of Debris Objects Used in Static RCS Measurements," XonTech Report 910555-1978, 1991.

[8] E. Stansbery, *et al*, "Characterization of the orbital debris environment from Haystack radar measurements," *Advances in Space Research,* vol. 16, no. 11, pp. 5-16, 1995.

[9] G. Bohannon, T. Caampued and N. Young, "First Order RCS Statistics of Hypervelocity Impact Fragments," XonTech Report 940128-BE-2305, 1994.

[10] D. Barton, *et al.*, "Final Report of the Haystack Orbital Debris Data Review Panel," Technical Memorandum 4809, NASA/JSC, Houston, Texas, 1998.

[11] R. Everett, T. Caampued and J. Chu, "Summary of Data Processing of September 1990 SPC Debris Data," XonTech Report 940128-BE-2305, 1991.

[12] R. Everett, C. Dalquist and T. Caampued, "Summary of Processing of January 1991 SPC Debris Data," XonTech Report 940128-BE-2305, 1991.

[13] N. Hill, "Measurement Techniques for Hypervelocity Impact Test Fragments," in *59th International Astronautical Congress*, Glasgow, Scotland, 2008.

[14] Y.-l. Xu and C. Stokely, "A Statistical Size Estimation Model for Haystack and HAX Radar Detections," in *56th International Astronautical Congress*, Fukuoka, Japan, 2005.

[15] H. Chen, *et al.*, "Effects of Geometry Configurations on Ambiguity Properties for Bistatic MIMO Radar," *Progress In Electromagnetics Research,* vol. B, no. 30, pp. 117-133, 2011.

[16] J. Murray, *et al.*, "Recent Results from the Goldstone Orbital Debris Radar: 2016-2017," in *First International Orbital Debris Conference*, 2019.

[17] NASA Orbital Debris Program Office, "The Intentional Destruction of Cosmos 1408," *Orbital Debris Quarterly News,* vol. 26, no. 1, pp. 1-5, March 2022.

[18] N. Johnson, *et al.*, "NASA's new breakup model of evolve 4.0," *Advances in Space Research,* vol. 28, no. 9, pp. 1377-1384, 2001.

[19] J. Murray, *et al.*, "Observations of Small Debris from the Cosmos 1408 Anti-Satellite Test using the HUSIR and Goldstone Radars," in *23rd Advanced Maui Optical and Space Surveillance Technologies Conference*, Maui, Hawaii, 2022.

[20] R. Tjoelker, "304 Frequency and Timing," 810-005, 304, Rev.B, Jet Propulsion Laboratory, 2014.

[21] M. Richards, Fundamentals of Radar Signal Processing, New York: McGraw Hill, 2014.

[22] M. Evans and J. Rosenthal, Probability and Statistics, The Science of Uncertainty, Macmillan, 2009.

[23] J. Jao, *personal communication,* 2020.

Appendix A: Goldstone Radar Geometries Observation Plan

This appendix provides a detailed observation plan for Goldstone using the combination of DSS-14 and either DSS-25 or DSS-26, which constitute the new pointing geometry for Goldstone.

Background

In March 2018, the Goldstone OD radar changed its bistatic radar geometry. Until this time, OD radar observations were conducted using a combination of DSS-14 as the transmitter and DSS-15 as the receiver. The baseline for this pointing geometry was 500 meters. The new bistatic radar geometry uses a combination of DSS-14 as the transmitter and one of the Deep Space Network (DSN) Apollo cluster antennas, DSS-25 or DSS-26, as the receiver, producing an approximately 10 km baseline. As a side effect, the overlap of the transmitter and receiver beams with the new baseline significantly reduces altitude coverage. A detailed observation plan was developed to determine how the current Goldstone radar should be operated for OD radar observations. The plan includes analysis of the coverage that may be obtained from different pointing geometries and recommendations on which pointing to use for a given altitude. A complicating factor is that data collected in 2018 showed that at the altitude where the overlapping gain patterns from the transmitter and receiver should be a maximum, a drop off in the OD flux was observed relative to prior years and relative to HUSIR for the same year.

Estimate of Required Hours

To find the maximum number of pointings that can be used in an annual survey plan with Goldstone, the number of observation hours necessary for an individual pointing to produce statistically significant data must be estimated. Of interest is the presence of an anomalously low flux observed near the beam intersection altitude in the Goldstone CY2018 data, specifically in the 750 km to 800 km altitude bin as shown in Figure A-1 and Figure A-2. In Figure A-1, the anomaly is evident when comparing Goldstone CY2018 data to other years, whereas in Figure A-2, the anomaly is evident in comparing the data against HUSIR observations in 2018. In the following figures, CY2017 represents the second half of the CY2017 dataset, whereas CY2018 represents the 800 km pointing used during that year.

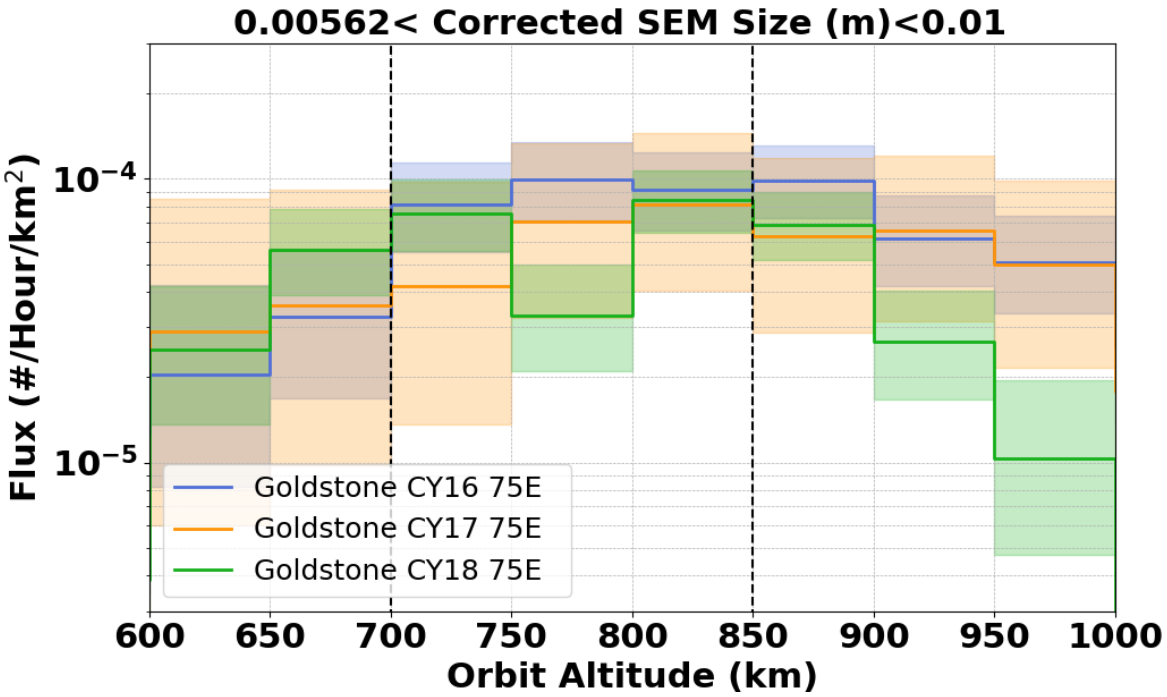

Figure A-1. Cumulative surface area flux versus altitude bound between 5.62 mm and 1 cm. The shaded regions represent the 2σ Poisson uncertainty bounds. The vertical dashed lines are approximate null-to-null beam overlap altitudes for the transmitter and receiver.

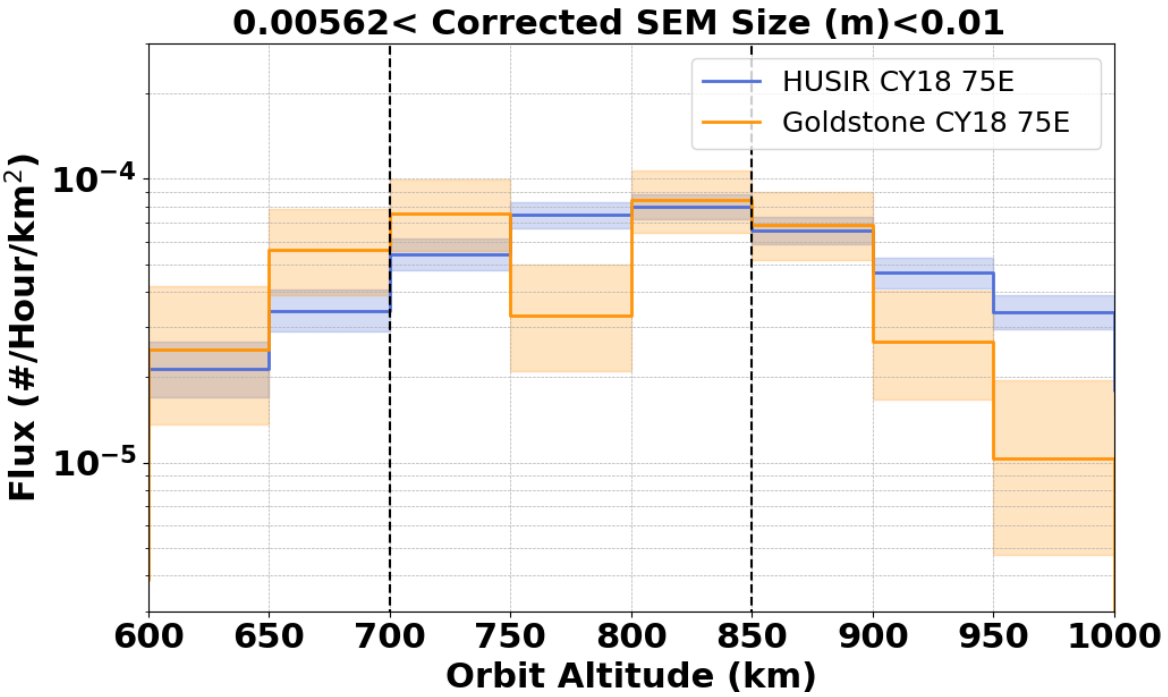

Figure A-2. Cumulative surface area flux versus orbit altitude, bound between 5.62 cm and 1 cm, for Goldstone CY2018-A and HUSIR CY2018 data.
The shaded regions represent the 2σ Poisson uncertainty bounds. The vertical dashed lines are the approximate null-to-null beam overlap altitudes for the transmitter and receiver.

To estimate the number of hours required for each pointing, observation hours were integrated for the CY2018 dataset until reasonable uncertainties in the flux were obtained – clearly indicating the presence of a reduced flux measurement at the beam overlap altitude. This was done by monitoring the evolution of the flux and uncertainties in the 750 km to 800 km bin as observations were performed over the year, integrating the data from each new observation one observation at a time. Figure A-3 shows the flux versus altitude for the first observation of CY2018, which occurred on DOY 196. Although the flux appears lower, the 2σ uncertainty bounds represented by the shaded regions show large uncertainties in the flux values, particularly at the beam overlap altitude. Figure A-4 shows the flux versus altitude for a combination of the first and second days with comparable results. After 3 days of observations (shown in Figure A-5) are integrated (about 13 hours), the flux and the associated count uncertainties in the 750 km to 800 km bin can be resolved to be statistically lower than the mean fluxes in adjacent altitude bins, and with respect to the CY2016 data. For the purposes of observation planning, a minimum of 3 observations (about 13 hours) are needed for each pointing to produce statistically significant data.

Since Goldstone collects data on an as available basis, it is necessary to estimate the expected number of observations and hours from Goldstone in a single year. Table A-1 shows the number of hours and observations received from Goldstone from 2008 to 2018 and shows ODPO has received an average of 12 observations (69.2 hours) per year in that time. Since each pointing requires at least three observations, this constrains the number of pointings in a viable survey plan to a maximum of three or four.

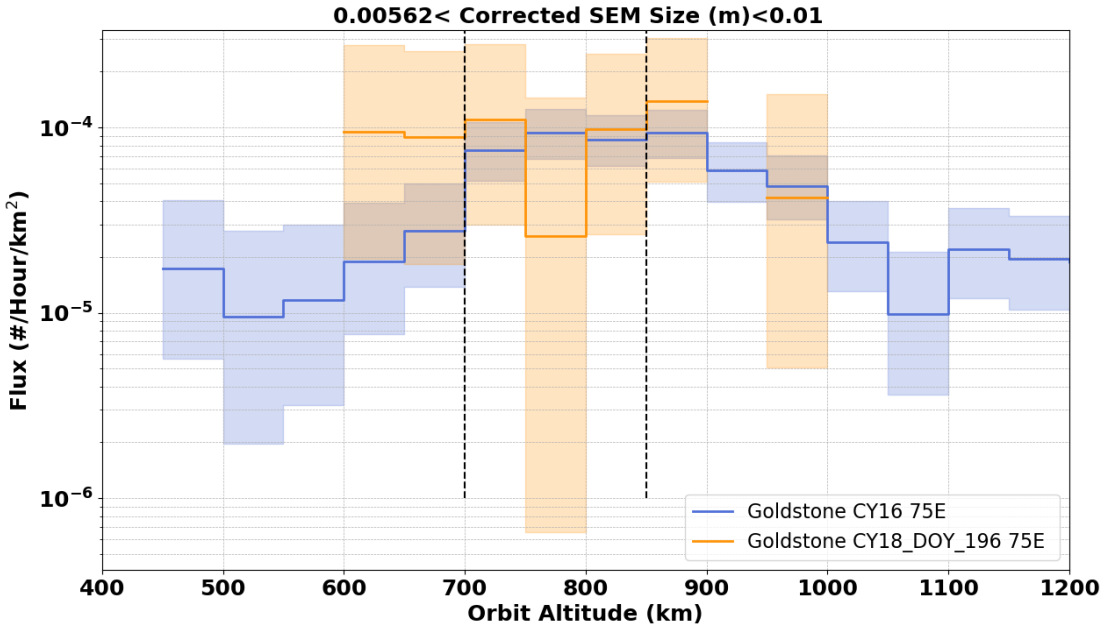

Figure A-3. Cumulative surface area flux versus orbit altitude, bound between 5.62 cm and 1 cm, for the first observation of Goldstone CY2018-A with Goldstone CY2016 data overlaid. The shaded regions represent the 2σ uncertainty bounds.

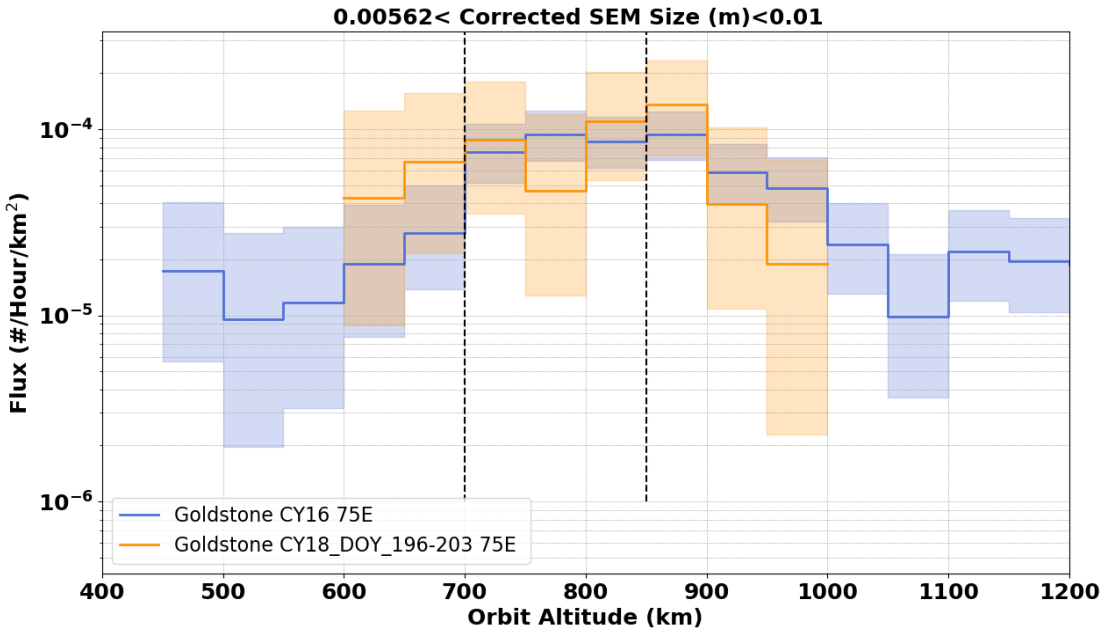

Figure A-4. Cumulative surface area flux versus orbit altitude, bound between 5.62 cm and 1 cm, for the first 2 observations of Goldstone CY2018-A with Goldstone CY2016 data overlaid. The shaded regions represent the 2-σ uncertainty bounds.

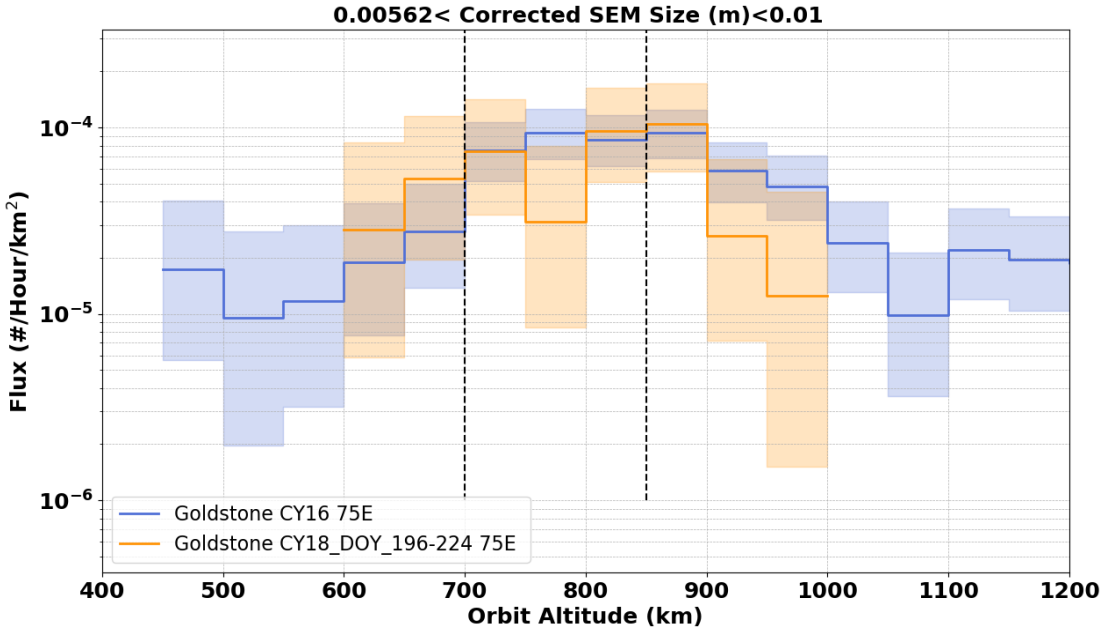

Figure A-5. Cumulative surface area flux versus orbit altitude, bound between 5.62 cm and 1 cm, for the first 3 observations of Goldstone CY2018-A with Goldstone CY2016 data overlaid. The shaded regions represent the 2-σ uncertainty bounds.

Table A-1. Number of Observations and the Corresponding Hours Received from Goldstone from 2008 to 2018

Year	Observations	Hours
2018	17	79
2017	11	52
2016	8	46
2015	20	99
2014	17	117
2013	12	72
2012	13	89
2011	12	63
2010	2	11
2009	7	36
2008	15	97
Average	12.2	69.2

Complete LEO Coverage Geometries (400 km – 2000 km)

The short baseline of the historical pairing of DSS-14/DSS-15 (about 500 meters), previously allowed Goldstone to sample all LEO altitudes with a single pointing. To determine the number of pointings required by the new geometry to replicate this ability, the altitude coverage of a single pointing relative to a constant dB gain offset in the previous baseline's peak gain as a function of altitude was defined. Offsets of 6 dB, 3 dB, and 1 dB were chosen for investigation. Figure A-6 shows that a reference offset of 6 dB requires 13 pointings, Figure A-7 shows that a reference offset of 3 dB requires 18 pointings, and Figure A-8 shows that a reference offset of 1 dB requires 29 pointings.

Practical constraints on the number of hours obtainable each year and those needed at each pointing to produce statistically significant data make it impossible to survey all of LEO within a single year. Instead, an approach that focuses on altitudes with a higher priority for observations is needed.

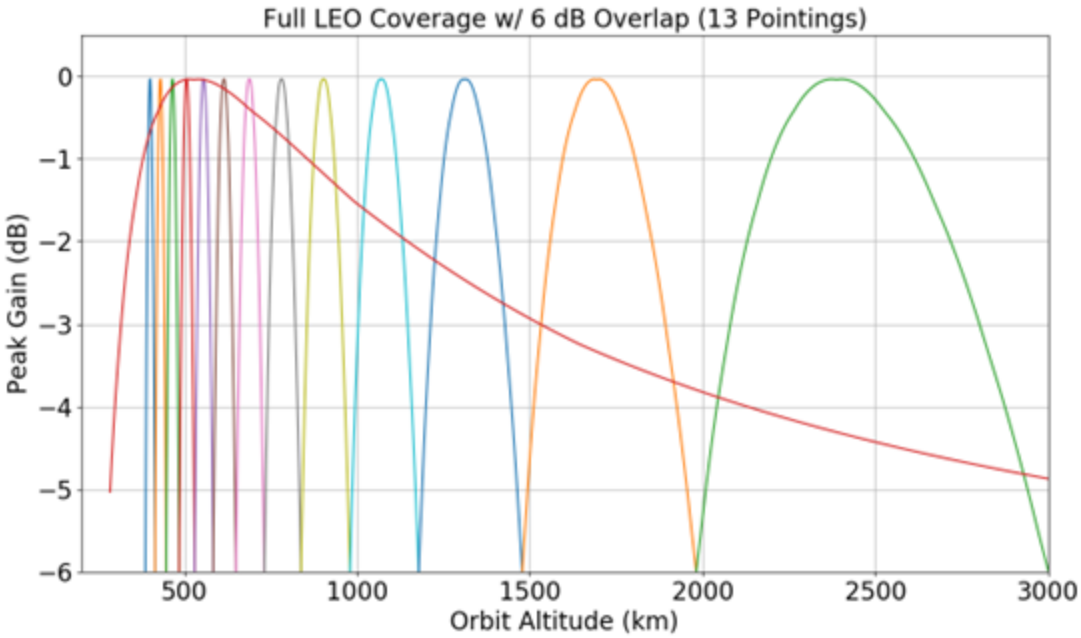

Figure A-6. Peak gain versus orbit altitude showing the number of pointings needed to cover all of LEO where the altitude coverage of a single pointing is defined by a constant offset in peak gain of 6 dB. The broad curve represents the peak gain of the legacy pointing.

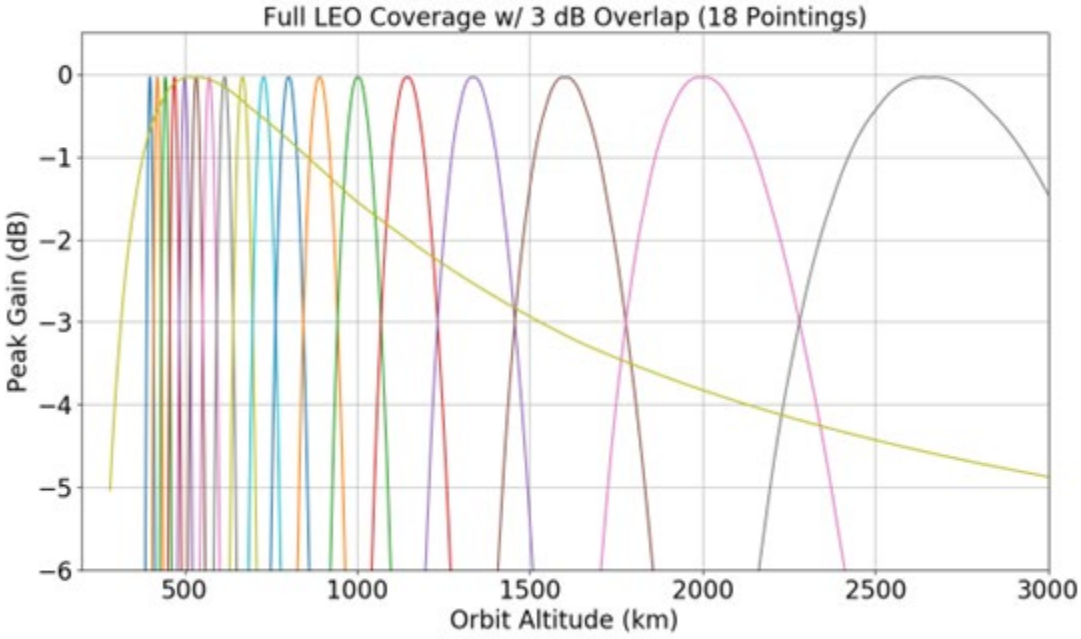

Figure A-7. Peak gain versus orbit altitude showing the number of pointings required to cover all of LEO where the altitude coverage of a single pointing is defined by a constant offset in peak gain of 3 dB.
The broad curve represents the peak gain of the legacy pointing.

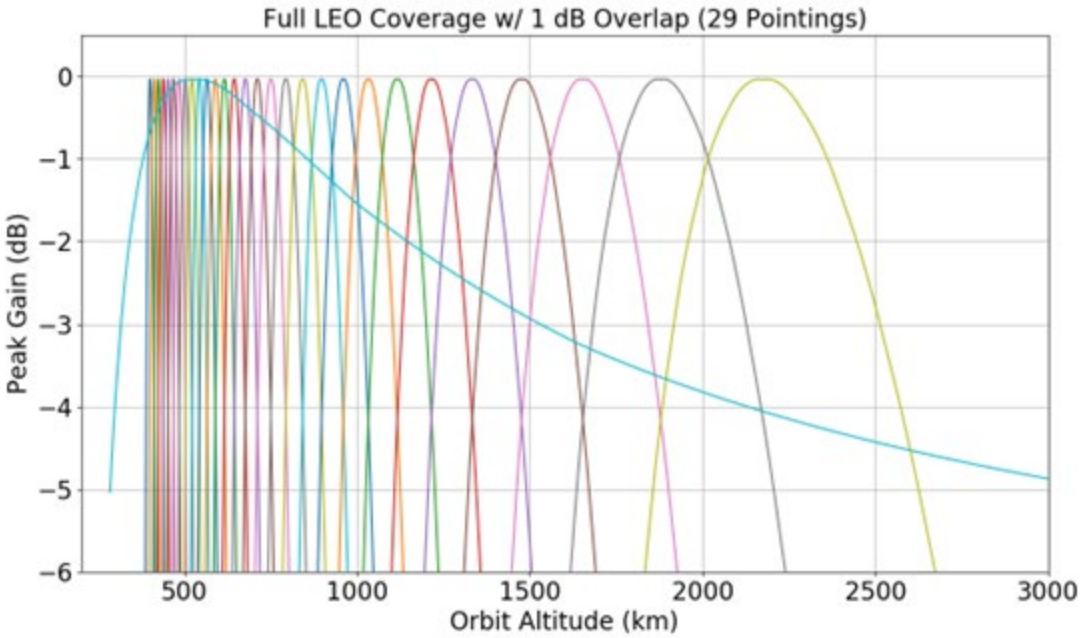

Figure A-8. Peak gain versus orbit altitude showing the number of pointings required to cover all of LEO where the altitude coverage of a single pointing is defined by a constant offset in peak gain of 1 dB.
The broad curve represents the peak gain of the legacy pointing.

Reducing Elevation to Increase Altitude Coverage

One approach to increase the altitude coverage of a single pointing at a particular altitude is to reduce the elevation angle of observation. The increased slant range results in a wider beam of both the transmitter and receiver for a given altitude. Figure A-9 and Figure A-10 show the widening of the altitude coverage as the elevation angle of the transmitter is reduced, at 400 km and 1000 km target altitudes. When considering the reduced sensitivity due to increased free space path loss (FSPL) at a given altitude, the increased altitude coverage is dwarfed by the loss of sensitivity. By 45° elevation, Goldstone would be no more sensitive than HUSIR (represented by the dashed black line), so reducing the elevation of observation is not a viable method of increasing the altitude coverage of a particular pointing.

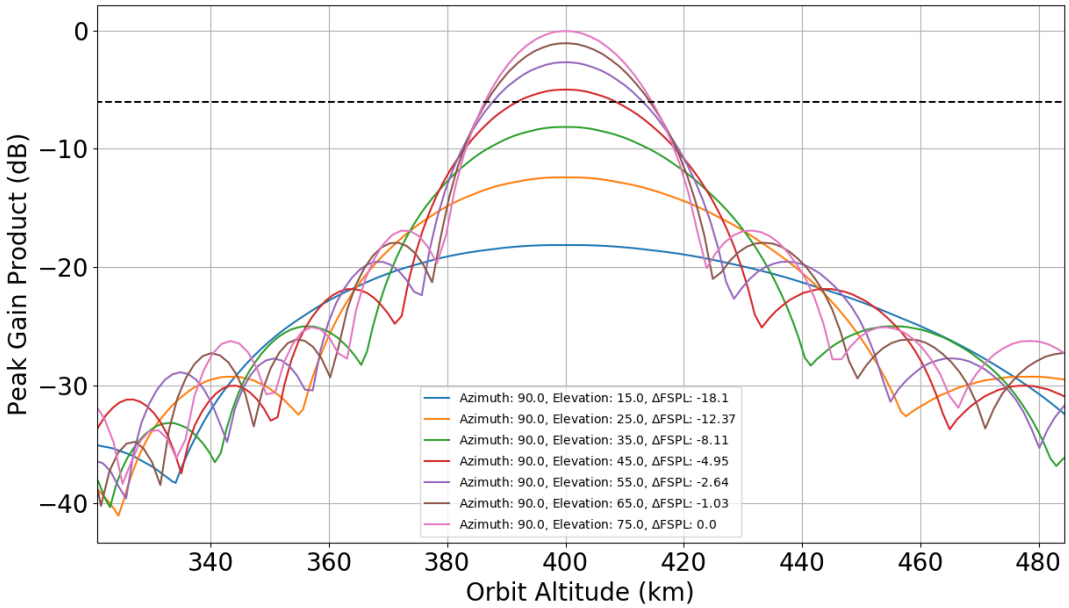

Figure A-9. Peak gain curves centered at 400 km altitude for various transmitter elevations with FSPL relative to 75E included.
The dashed black line represents the peak gain product of HUSIR, for comparison.

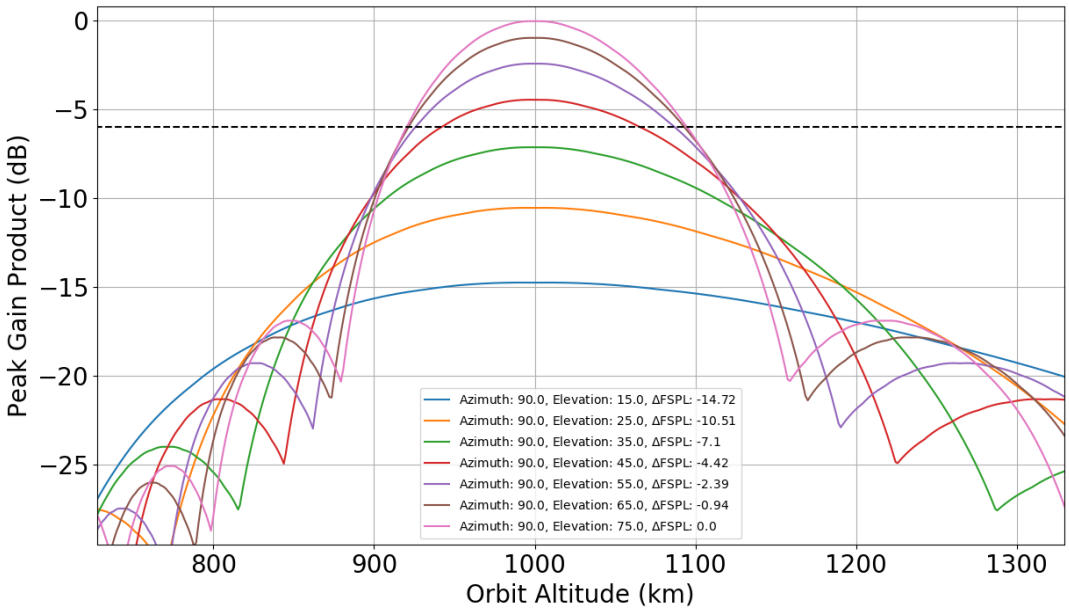

Figure A-10. Peak gain curves centered at 1000 km altitude for various transmitter elevations with FSPL relative to 75E included.
The dashed black line represents the peak gain product of HUSIR, for comparison.

South Staring versus East Staring to Increase Altitude Coverage

Another approach to increase altitude coverage of the beam overlap is to aim the antennas along the baseline connecting them, sometimes referred to as "over the shoulder." Since DSS-25 and DSS-26 lie mostly south of DSS-14, the difference in altitude coverage between a south pointing and east pointing geometry was investigated. Figure A-11 and Figure A-12 show the altitude coverage of east and south pointings at 400 km for elevations of 75° and 60° respectively. Although the altitude coverage is increased, it is negligible. The ability to resolve the ambiguity in Doppler inclinations for orbits with inclination above 90° would be lost, making this option undesirable.

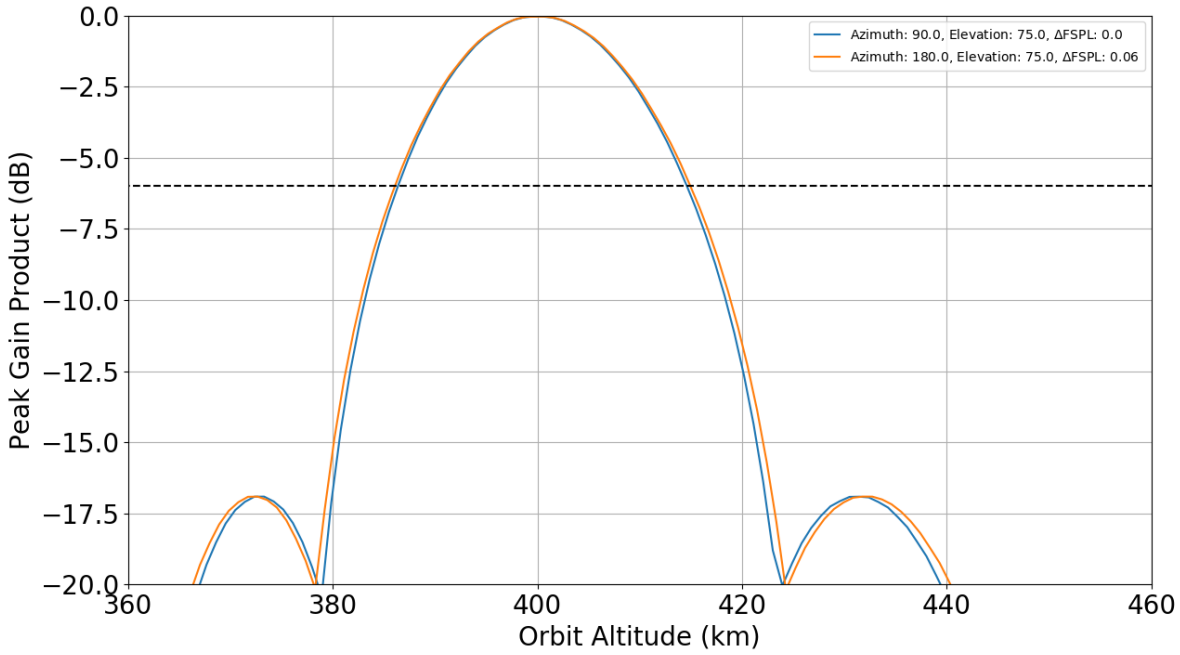

Figure A-11. Peak gain curves centered at 400 km altitude for east and south staring pointings at 75° elevation.
The dashed black line represents the peak gain product of HUSIR, for comparison.

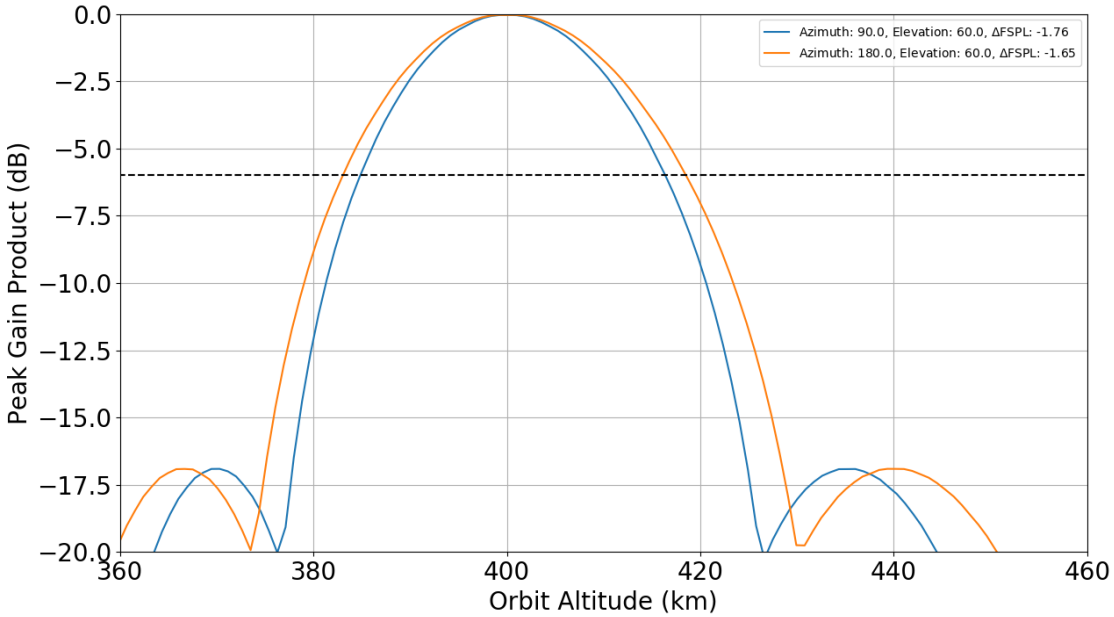

Figure A-12. Peak gain curves centered at 400 km altitude for east and south staring pointings at 60° elevation.
The dashed black line represents the peak gain product of HUSIR, for comparison.

Limited Coverage Geometry: 700 km – 1000 km

Based on results above in the estimated required hours section, the maximum number of pointings that can be employed in an observation plan designed for an annual survey is four, assuming the average observation trends from 2008 to 2018. Since results from the full LEO coverage (400 km to 2000 km) require at least 13 pointings, a limited coverage geometry plan was developed to focus on narrower coverage of altitudes of interest, namely 700 km to 1000 km. From results presented in reducing elevation to increase altitude coverage sections, it was determined that the optimal pointing for the transmitter, DSS-14, is 75E. This plan was developed assuming the transmitter is pointed 75E and the receiver pointing is chosen to intersect the transmitter boresight at altitudes of interest.

To determine the altitude coverage of a particular pointing, some convention for when the altitude coverage of a pointing starts and ends must be used. One method is to define some fixed gain offset, such as 1 dB, 3 dB, or 6 dB, as the start and stop altitudes. However, to mimic the historical sensitivity of the DSS-14/DSS-15 pair, the convention chosen was to define the start and stop altitudes in reference to the historical peak gain curve, offset by some constant value. This ensured that the sensitivity of the new geometry was at least as good as the historical geometry at any given altitude. Although the ideal case would have no offset from the historical peak gain curve, analysis showed this would require at least seven individual pointings to cover 700 km to 1000 km, as shown in Figure A-13.

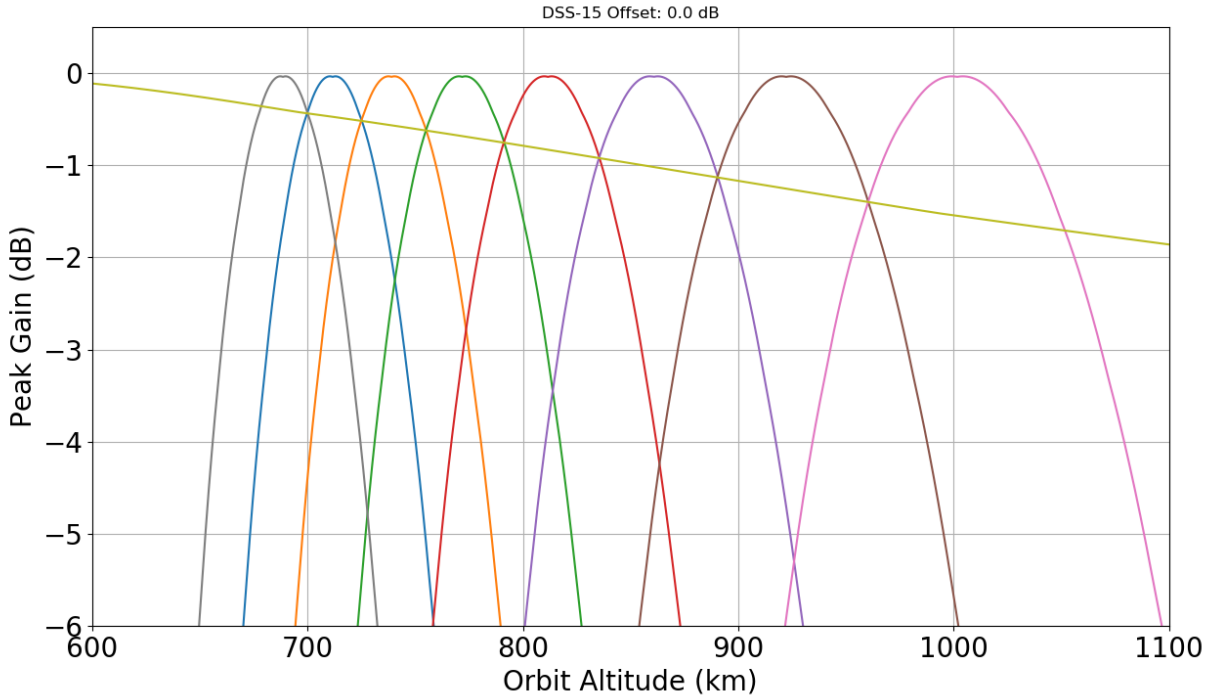

Figure A-13. Pointings required to cover 700 km to 1000 km in altitude, where the altitude coverage of a single pointing is defined by its intersection with the historical peak gain curve with no offset, represented by the yellow curve.

By using an offset of 1.5 dB from the historical peak gain curve, 700 km to 1000 km could be covered with only 4 pointings and 700 km to 900 km with just 3, as shown in Figure A-14. This set of pointings, dubbed A, B, C, and D, were chosen for initial testing in FY2021. Details of each pointing, such as AZ and EL of each receiver, intersection slant range for the transmitter, and intersection altitude, are presented in Table A-2. Figure A-15 shows the completeness size as a function of altitude for each of these pointings, as well as the historical completeness size, overlaid on CY2016 data from Goldstone.

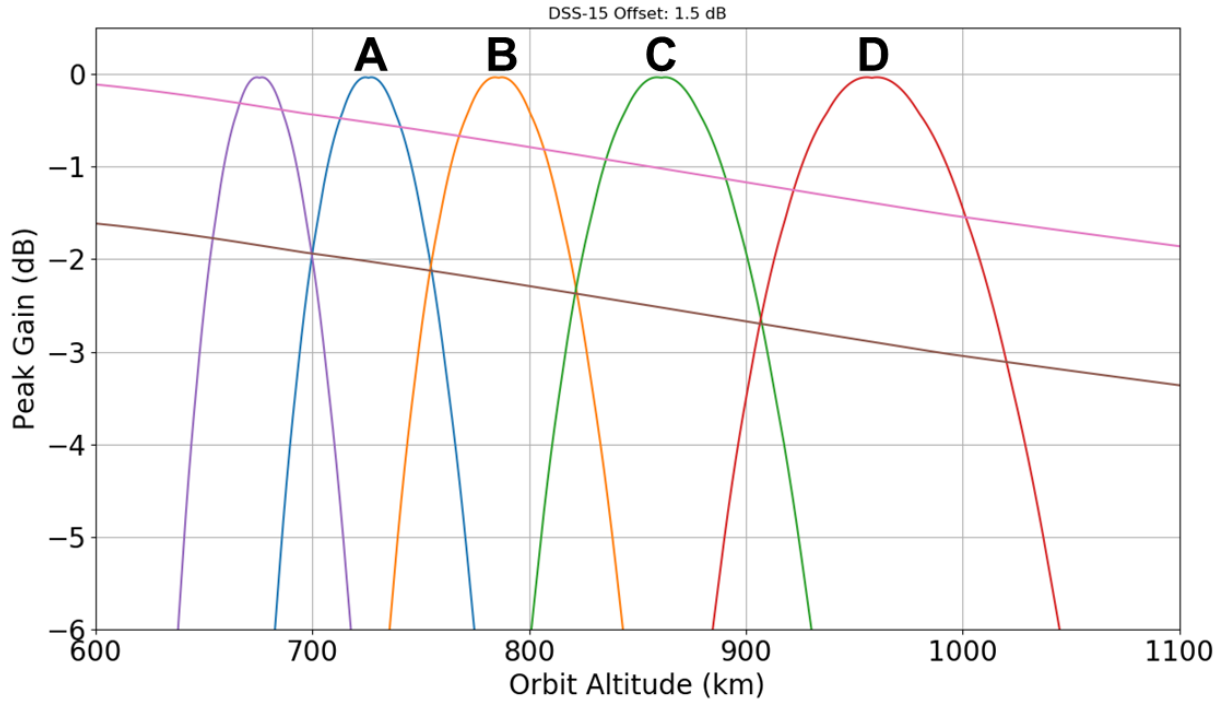

Figure A-14. Pointings needed to cover 700 km to 1000 km in altitude, where the altitude coverage of a single pointing is defined by its intersection with the historical peak gain curve with a 1.5 dB offset, represented by the brown curve. The historical peak gain curve with no offset is represented by the pink curve.

Table A-2. Pointing Details for A, B, C, and D from Figure A-14*[*]

Pointing Name	Intersection Altitude (km)	DSS-14 Slant Range (km)	DSS-25 Azimuth* (deg)	DSS-25 Elevation* (deg)	DSS-26 Azimuth* (deg)	DSS-26 Elevation* (deg)
A	725.967	755.155	86.7862	75.0842	86.7135	75.1005
B	785.860	816.717	87.0054	75.0800	86.9380	75.0953
C	860.889	893.794	87.2368	75.0753	87.1749	75.0895
D	957.904	993.393	87.4830	75.0700	87.4270	75.0831

[*] Computed AZ and EL Values are Rounded to Four Decimal Place Input Limits for Goldstone's Pointing Software.

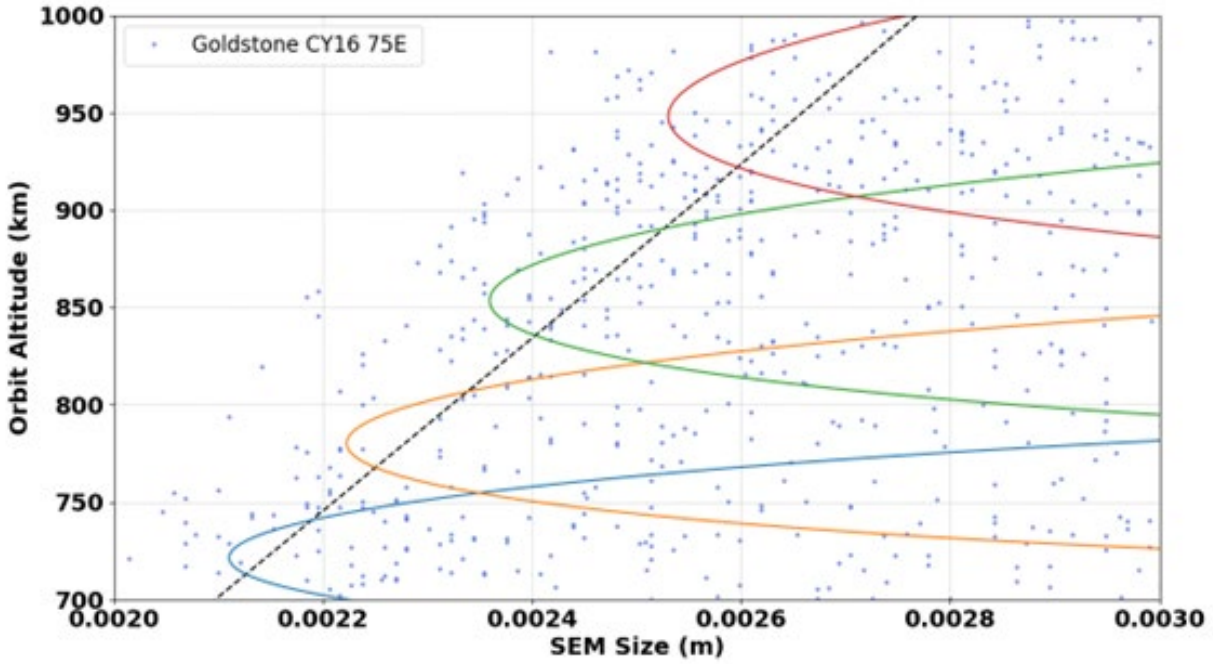

Figure A-15. Orbit altitude versus SEM size of Goldstone CY2016 with historical completeness curve (dashed black curve) and the completeness curves of each of the chosen pointings.

Pointing Error Gain Loss

One area worsened by the longer baseline is errors in the pointing of the two dishes, causing a misalignment of the beams. To estimate the variations in peak range and possible losses in maximum gain due to these pointing errors, Monte Carlo simulations were performed in which random errors, drawn from Gaussian distributions, were added to the nominal AZ and EL of the transmitter and receiver. Based on information received from Goldstone antenna calibration engineers, the maximum standard deviation of EL or cross-elevation pointing error measured over March to December 2018 was 4.36 millidegrees. As a conservative estimate, this value was used for the standard deviations of the EL error and cross-elevation error distributions.

The Monte Carlo program accepts inputs for EL and AZ for each antenna. The EL and AZ for a drawn elevation error, ΔEL, and cross-elevation error, ΔXEL, are given by equations A-1 and A-2, where $EL_{nominal}$ and $AZ_{nominal}$ are the nominal elevation and azimuth for a given pointing.

$$EL = EL_{nominal} + \Delta EL \qquad (A-1)$$

$$AZ = AZ_{nominal} + \frac{\Delta XEL}{cosEL_{nominal}} \qquad (A-2)$$

The peak gain product as a function of range was calculated using the perturbed pointings of both the transmitter and the receiver. From this curve, the maximum peak gain product, and the

range at which this maximum occurred were recorded. This process was then repeated for a total of 10,000 samples. The gain and range distributions for each transmitter/receiver pair for each of the four pointings (eight total combinations), as well as the mean and standard deviations of the range distributions, are shown in Figure A-16 through Figure A-23. Data from all 80,000 Monte Carlo runs are available for additional analysis. Further work for the parameterization of this data and its incorporation into modeling uncertainties is ongoing.

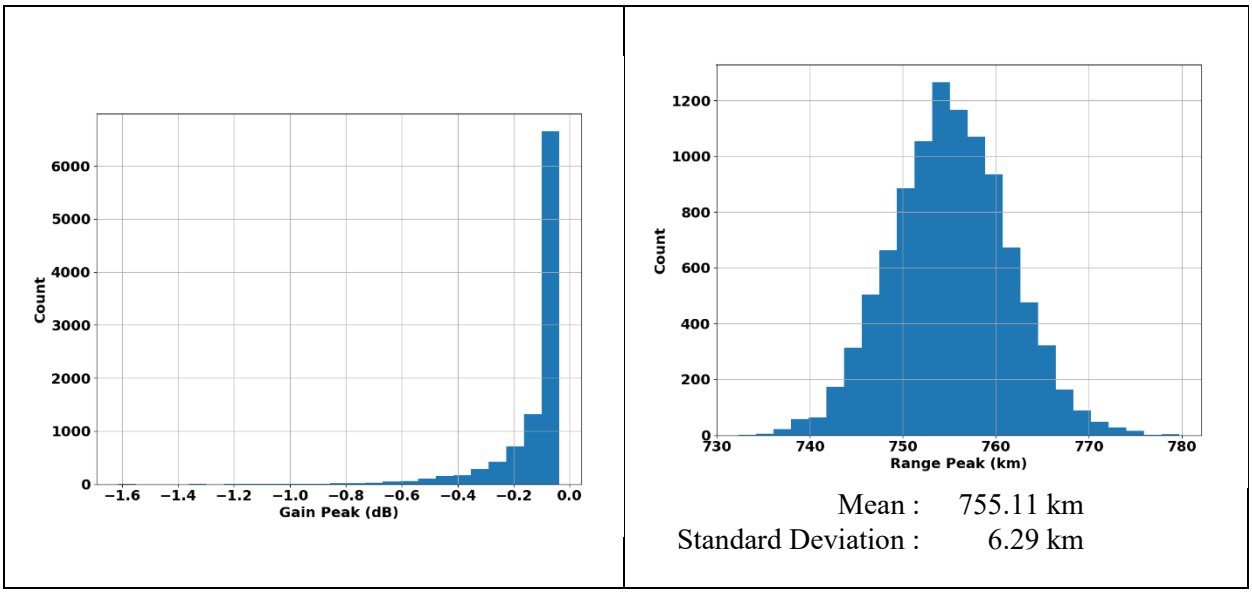

Figure A-16. DSS-25, pointing A

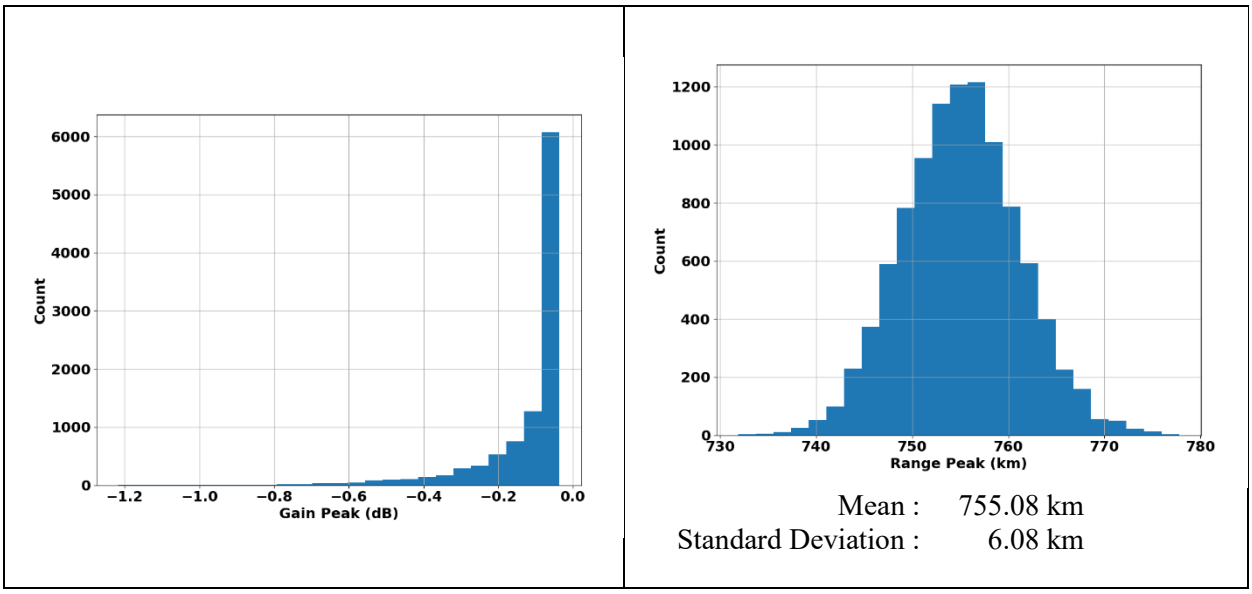

Figure A-17. DSS-26, pointing A

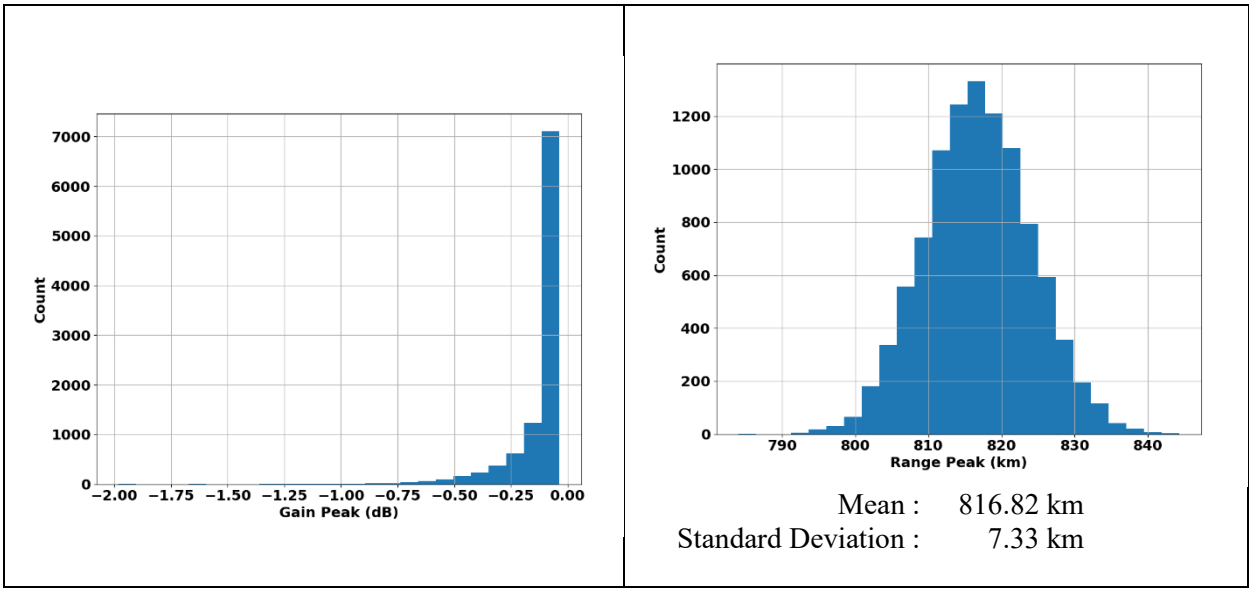

Figure A-18. DSS-25, pointing B

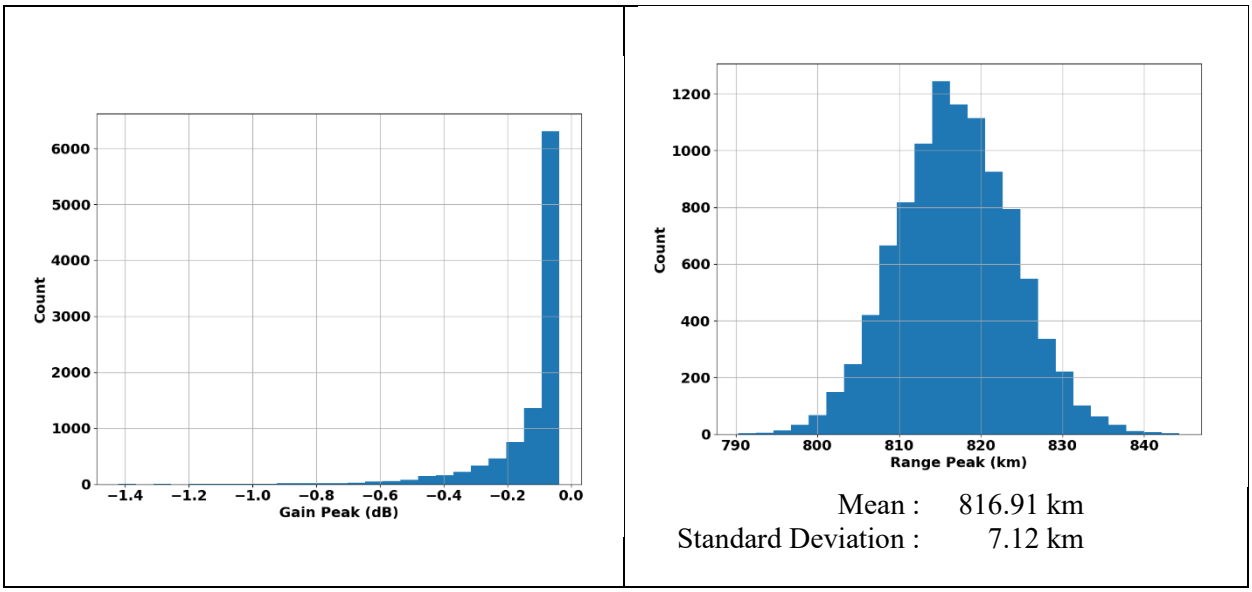

Figure A-19. DSS-26, pointing B

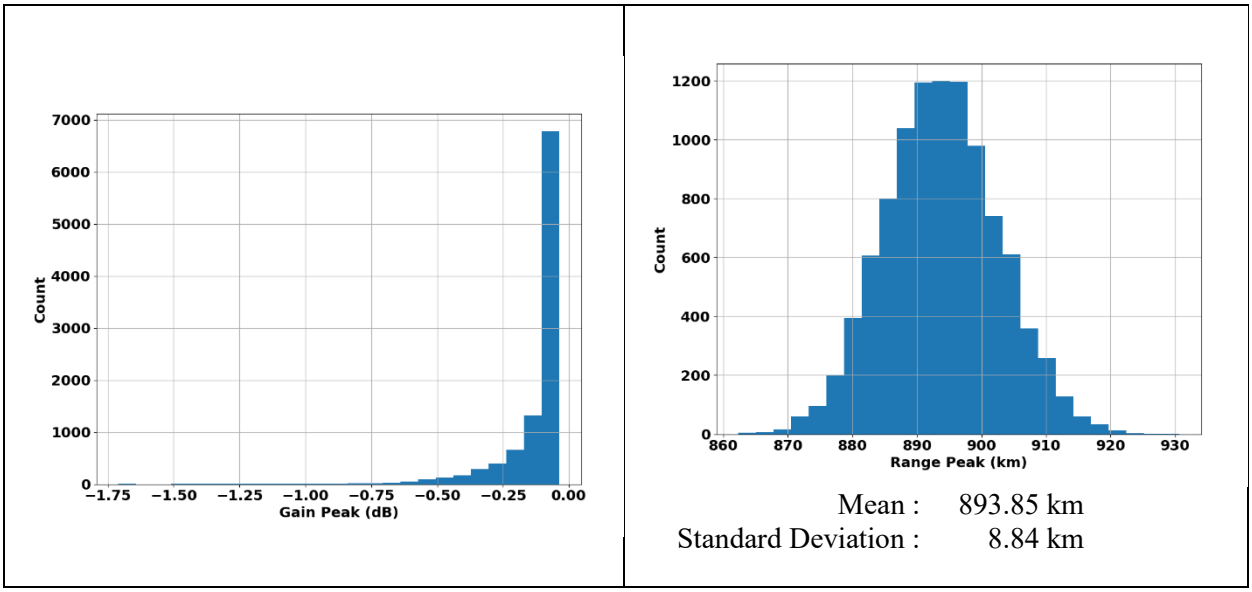

Figure A-20. DSS-25, pointing C

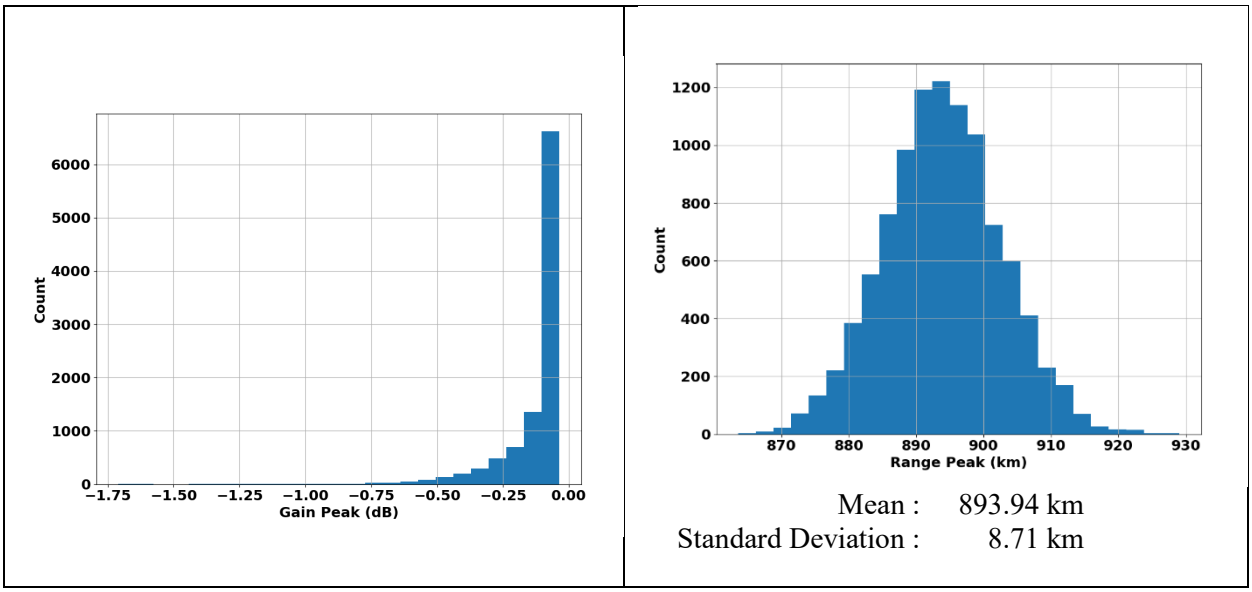

Figure A-21. DSS-26, pointing C

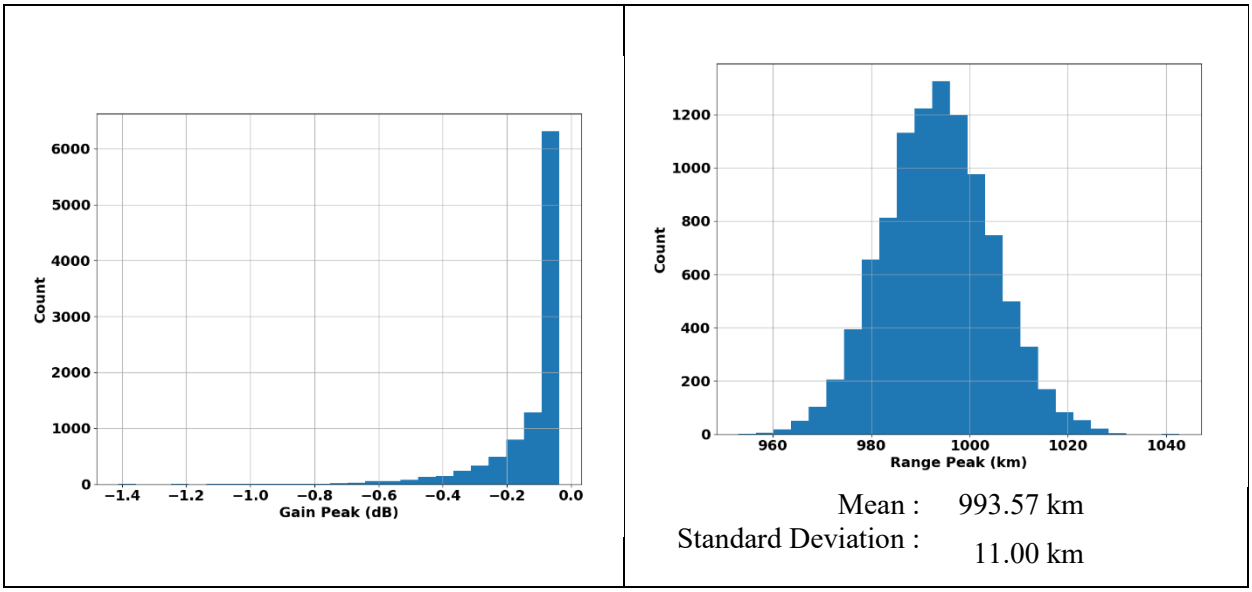

Figure A-22. DSS-25, pointing D

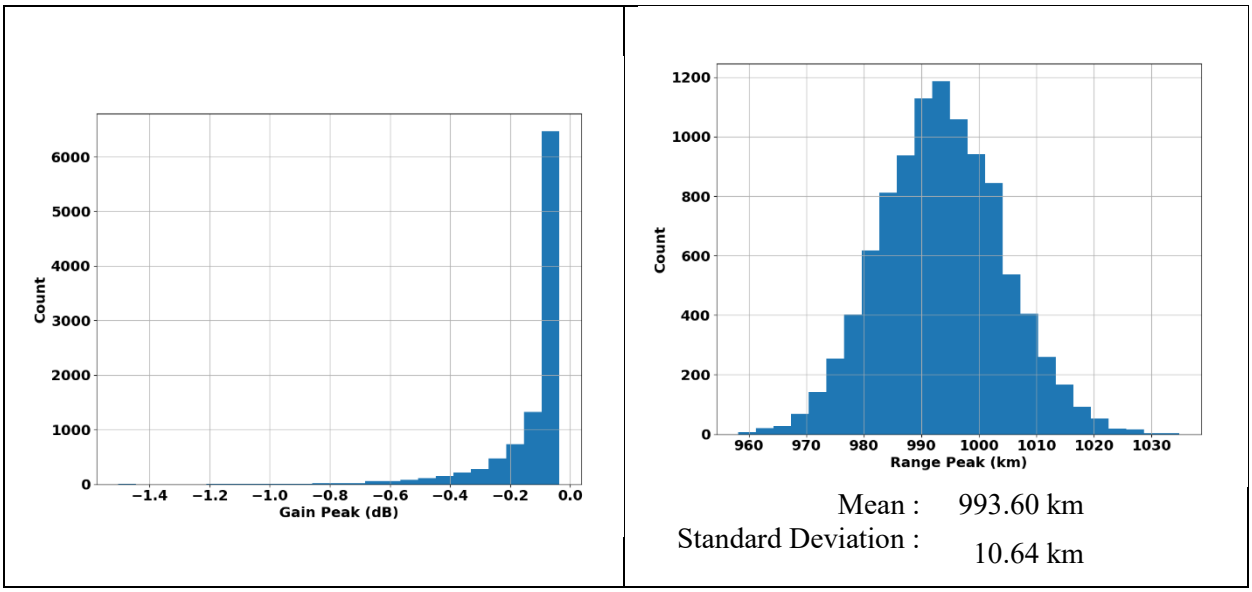

Figure A-23. DSS-26, pointing D

Appendix B: Range and Range-rate Residual Determination

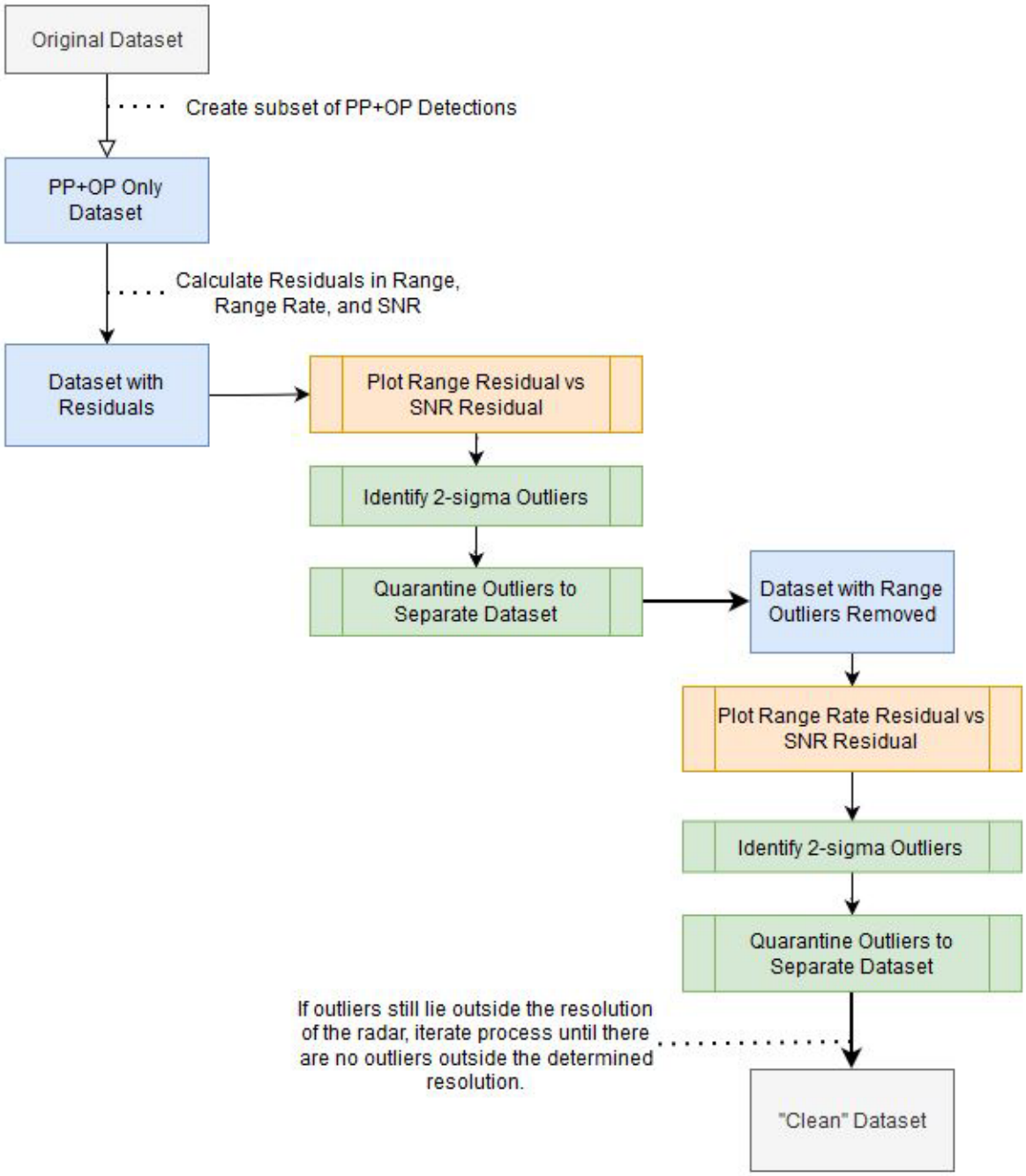

Figure B-1. Flow diagram of range and range-rate residual process.

Appendix C: CY2020- 2021 Pointing A

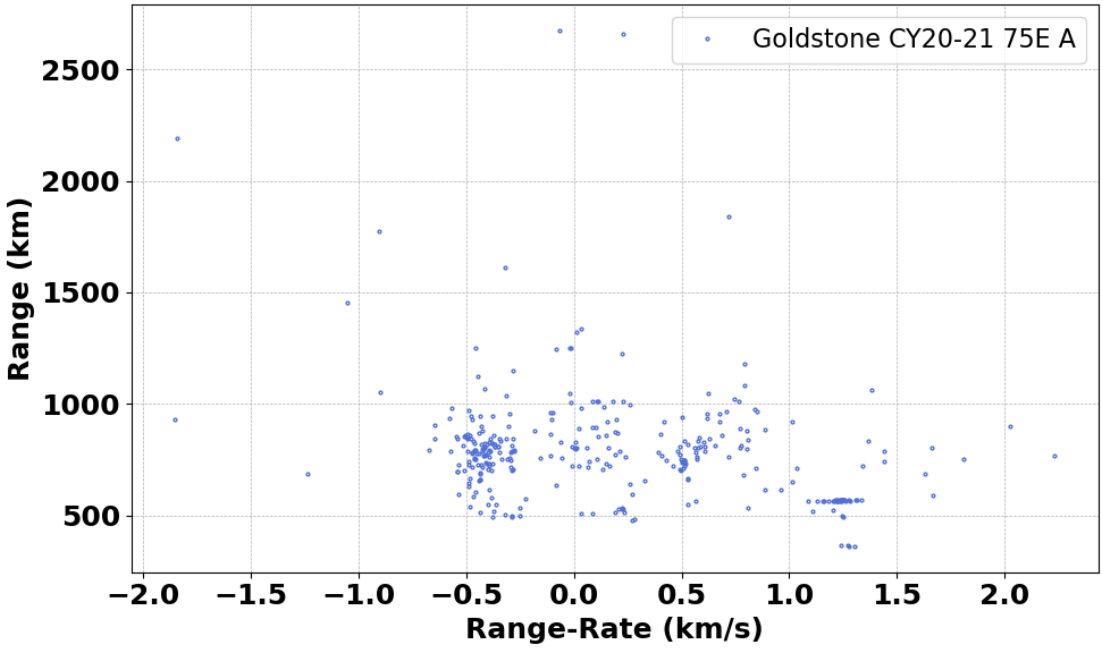

Figure C-1. Range versus range-rate of Goldstone CY2020–2021, pointing A.

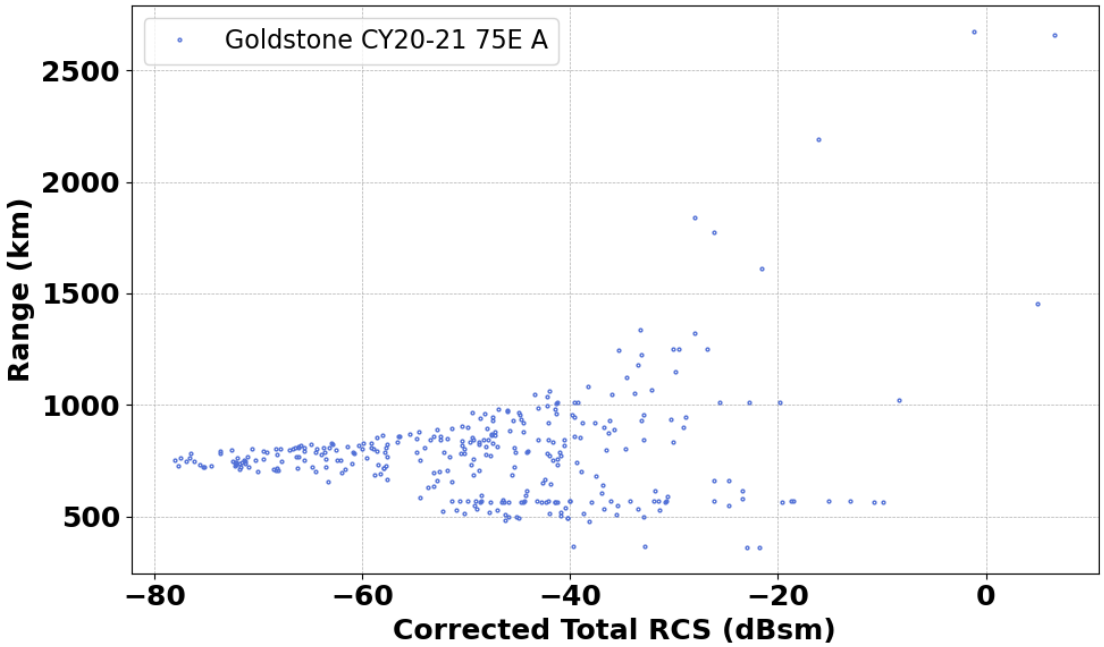

Figure C-2. Range versus total RCS of Goldstone CY2020–2021, pointing A.

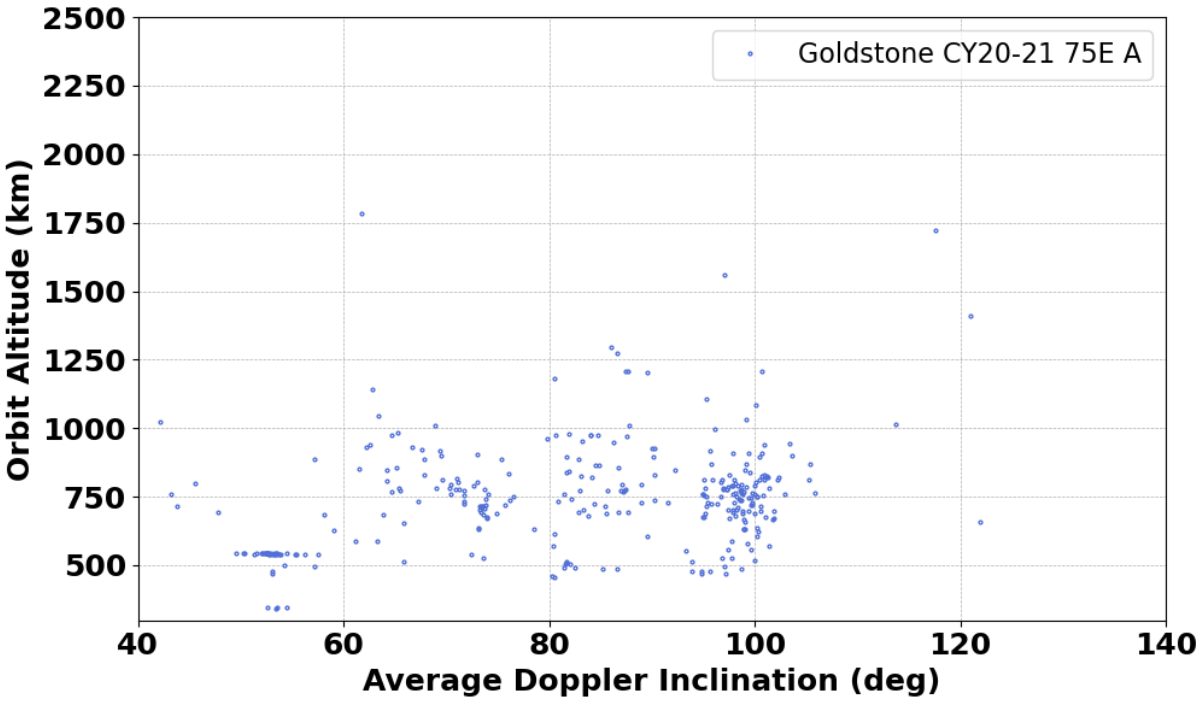

Figure C-3. Orbit altitude versus average Doppler inclination of Goldstone CY2020–2021, pointing A.

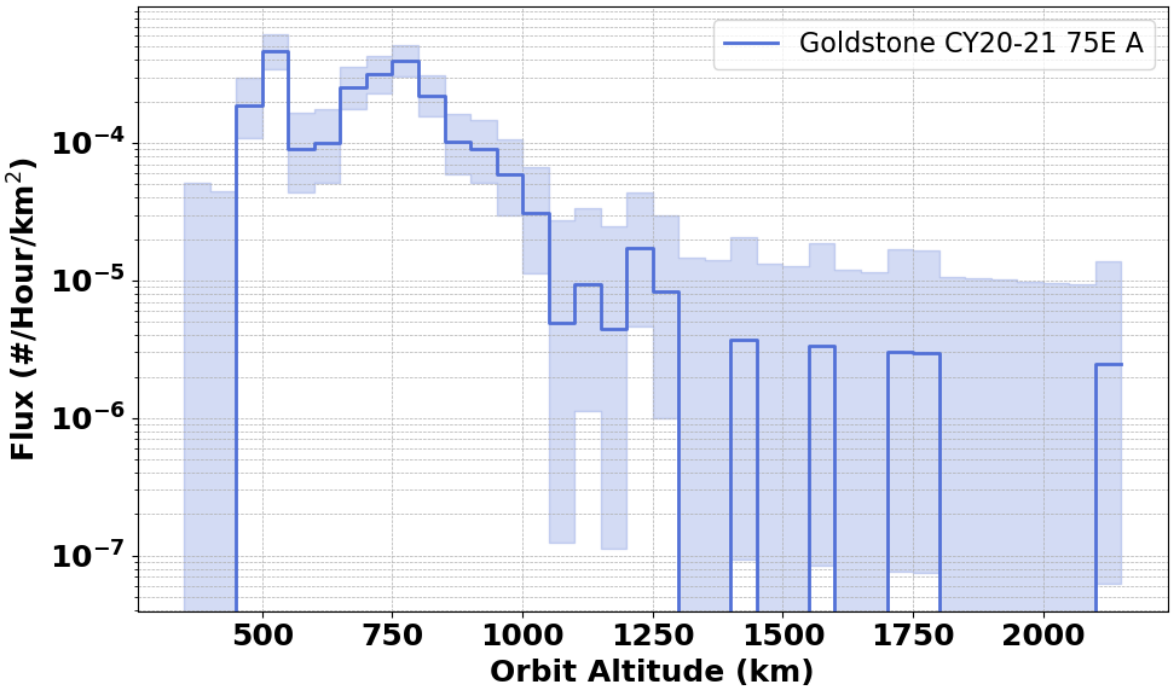

Figure C-4. Flux versus orbit altitude of Goldstone CY2020–2021, pointing A.

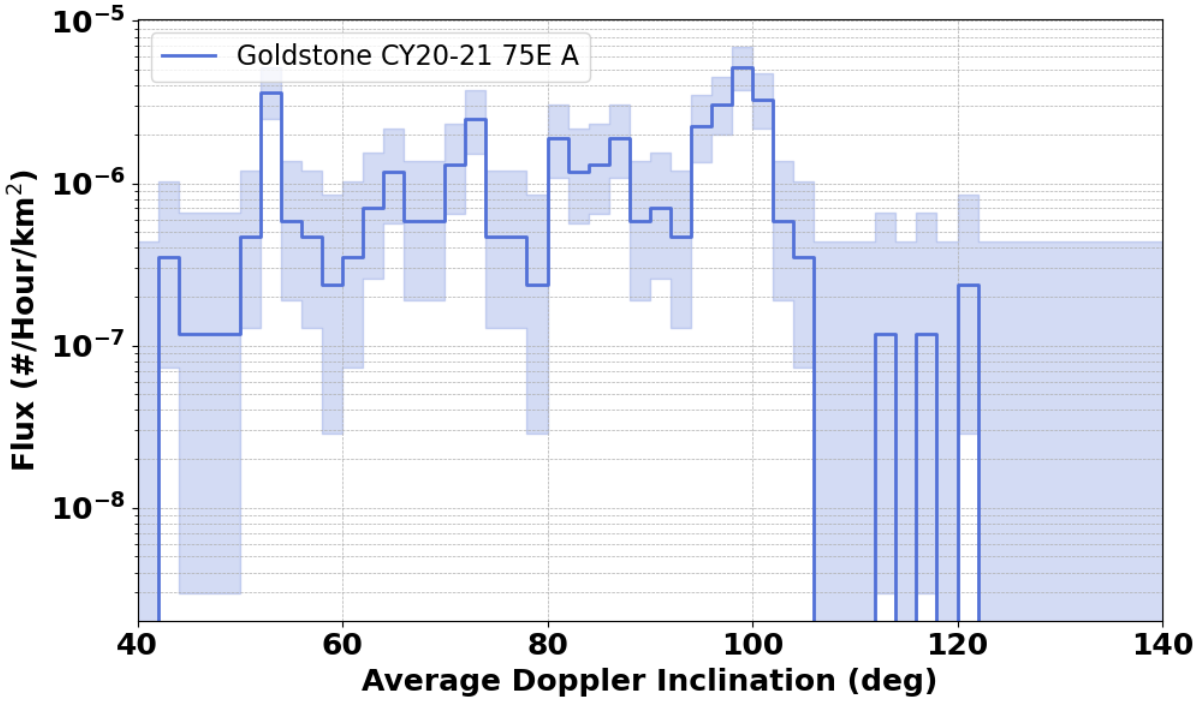

Figure C-5. Flux versus average Doppler inclination of Goldstone CY2020–2021, pointing A.

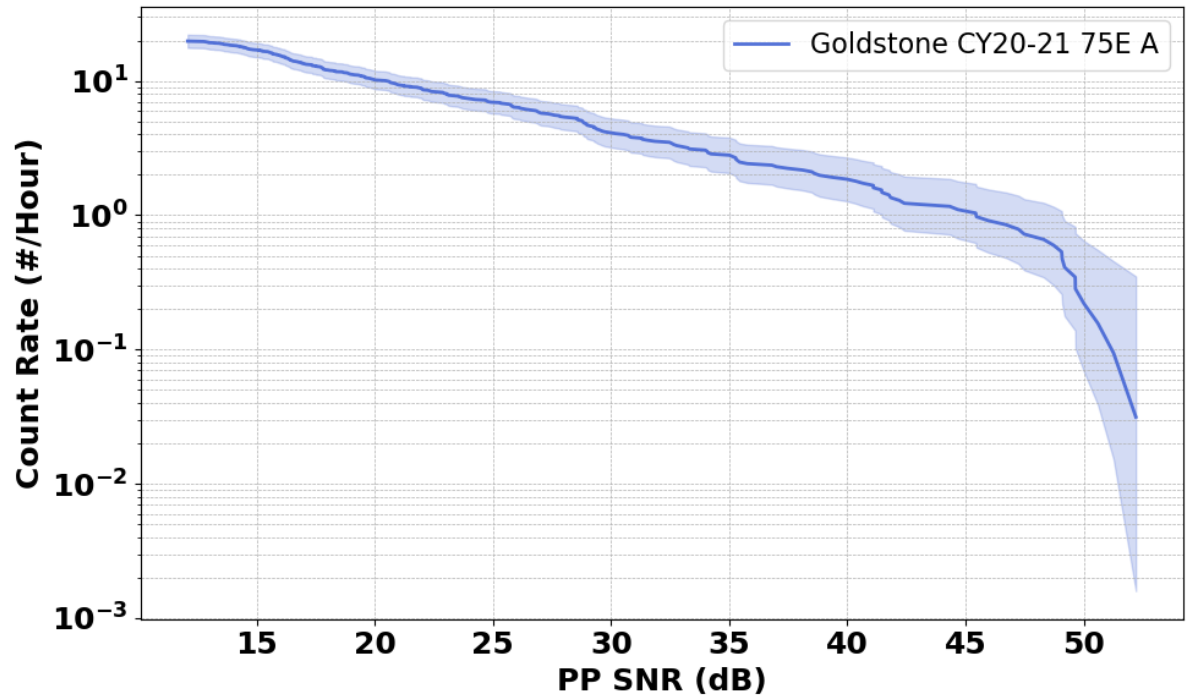

Figure C-6. Cumulative count rate versus PP SNR of Goldstone CY2020–2021, pointing A.

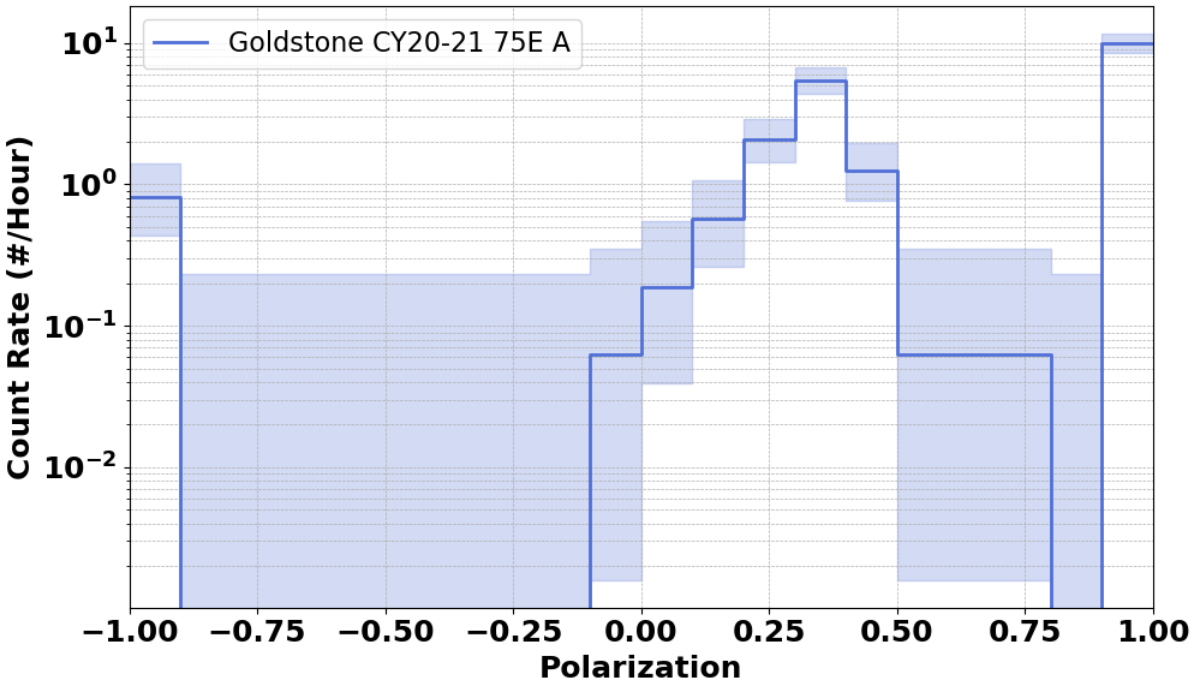

Figure C-7. Count rate versus polarization of Goldstone CY2020–2021, pointing A.

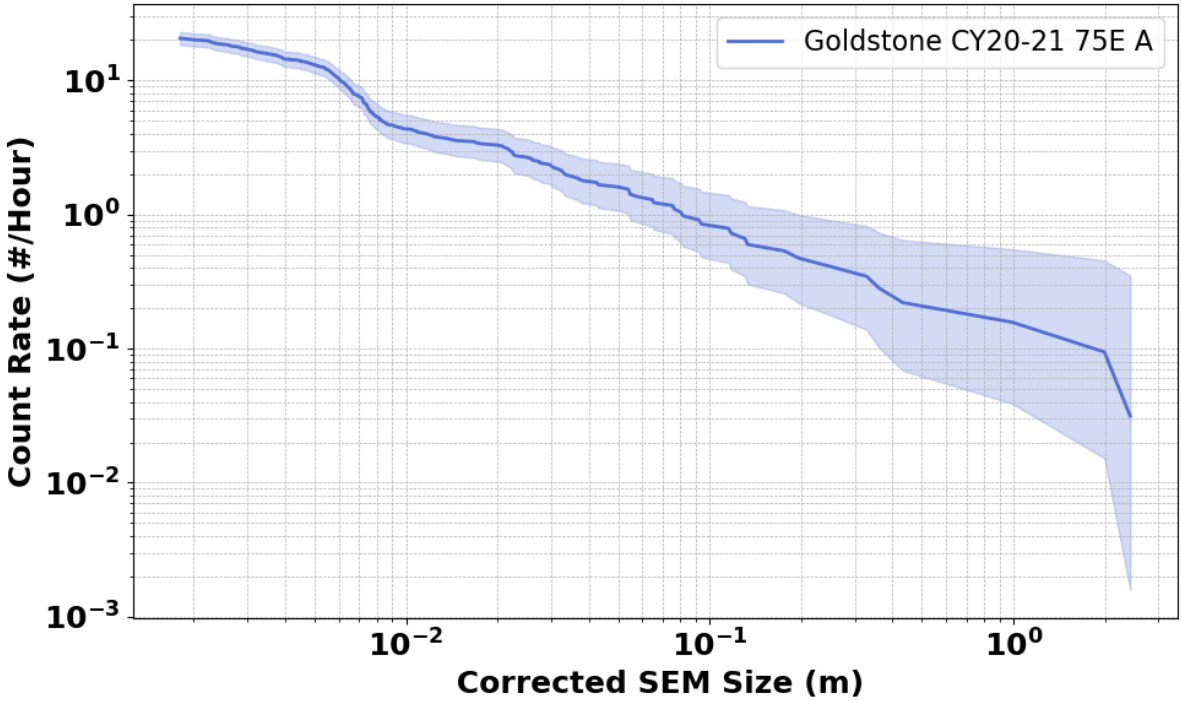

Figure C-8. Cumulative count rate versus SEM size of Goldstone CY2020–2021, pointing A.

Appendix D: CY2020–2021, Pointing B

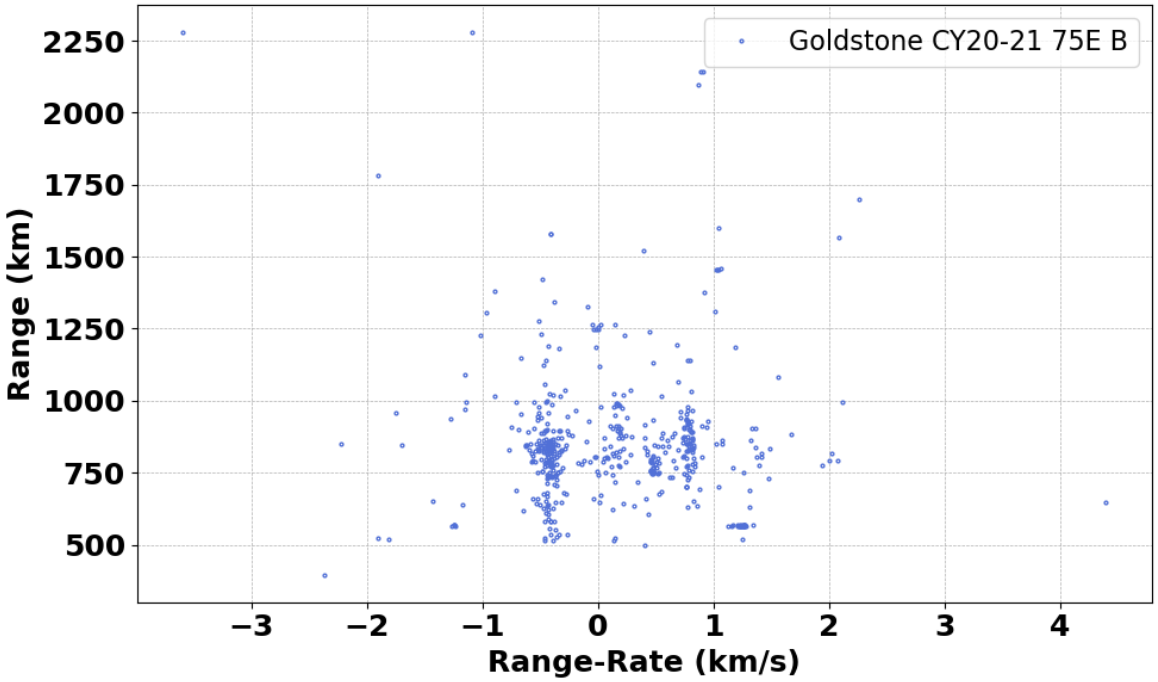

Figure D-1. Range versus range-rate of Goldstone CY2020–2021, pointing B.

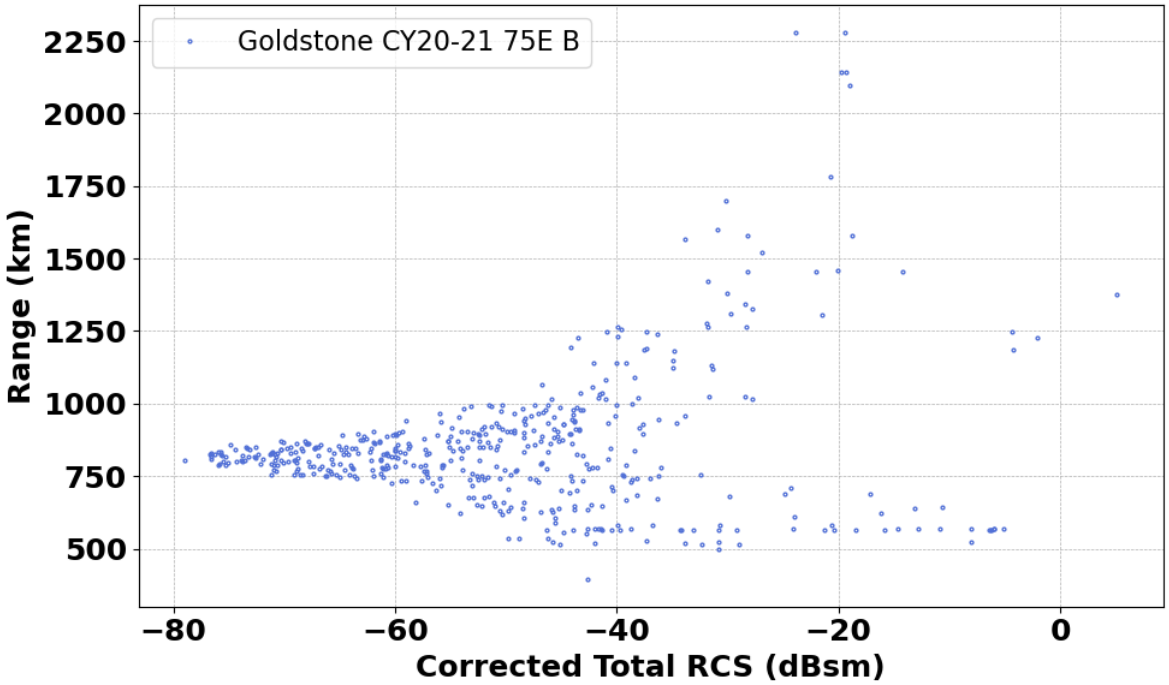

Figure D-2. Range versus total RCS of Goldstone CY2020–2021, pointing B.

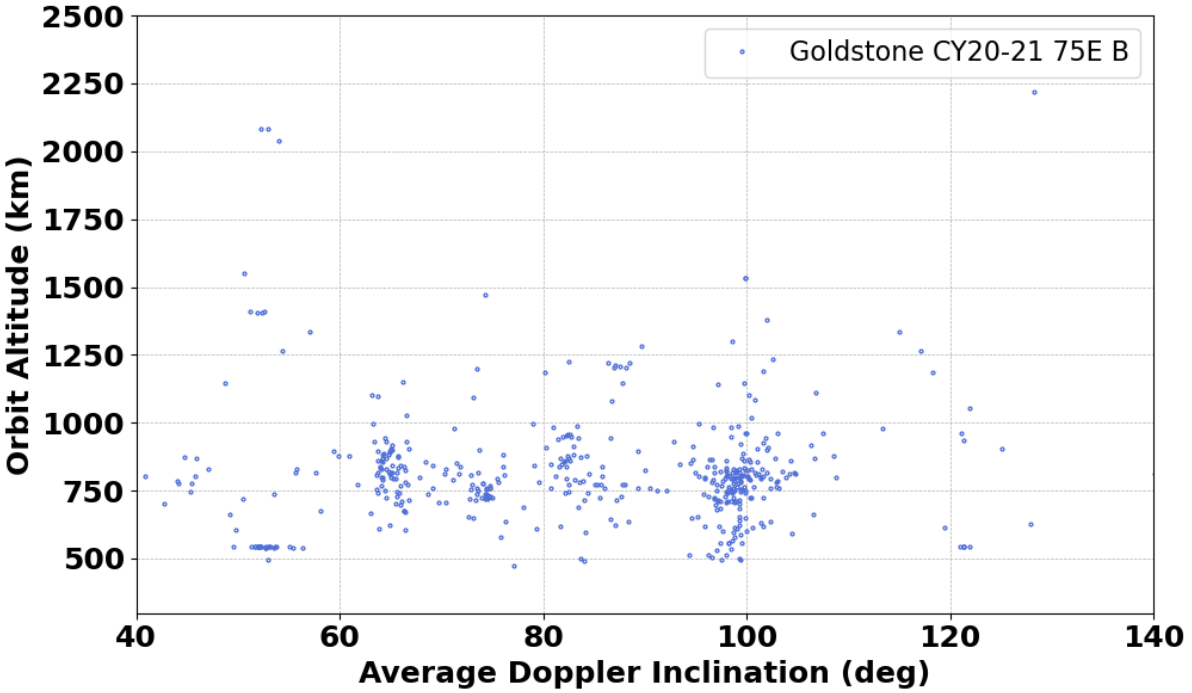

Figure D-3. Orbit altitude versus average Doppler inclination of Goldstone CY2020–2021, pointing B.

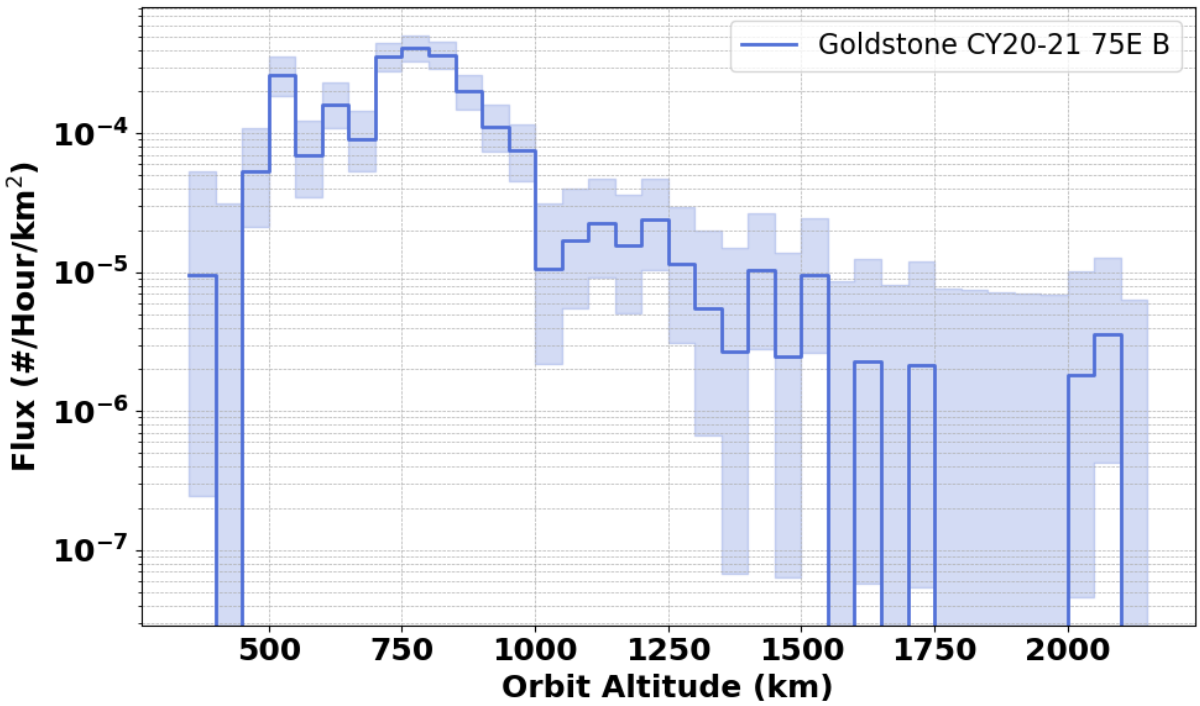

Figure D-4. Flux versus orbit altitude of Goldstone CY2020–2021, pointing B.

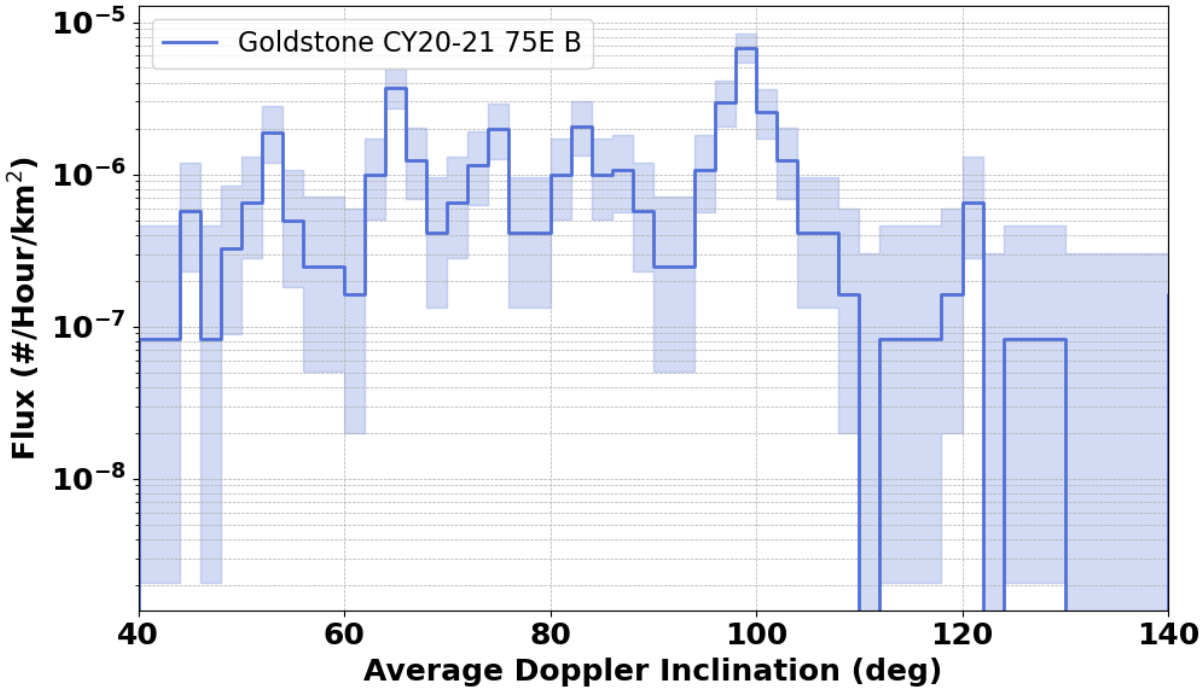

Figure D-5. Flux versus average Doppler inclination of Goldstone CY2020–2021, pointing B.

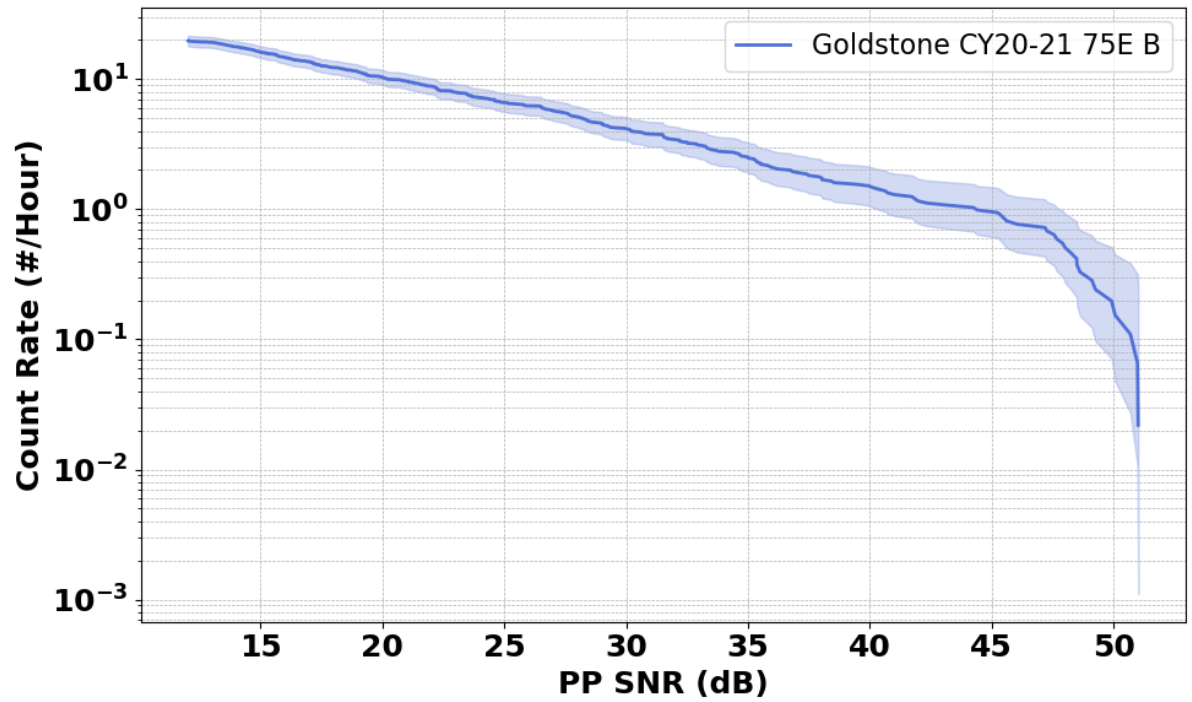

Figure D-6. Cumulative count rate versus PP SNR of Goldstone CY2020–2021, pointing B.

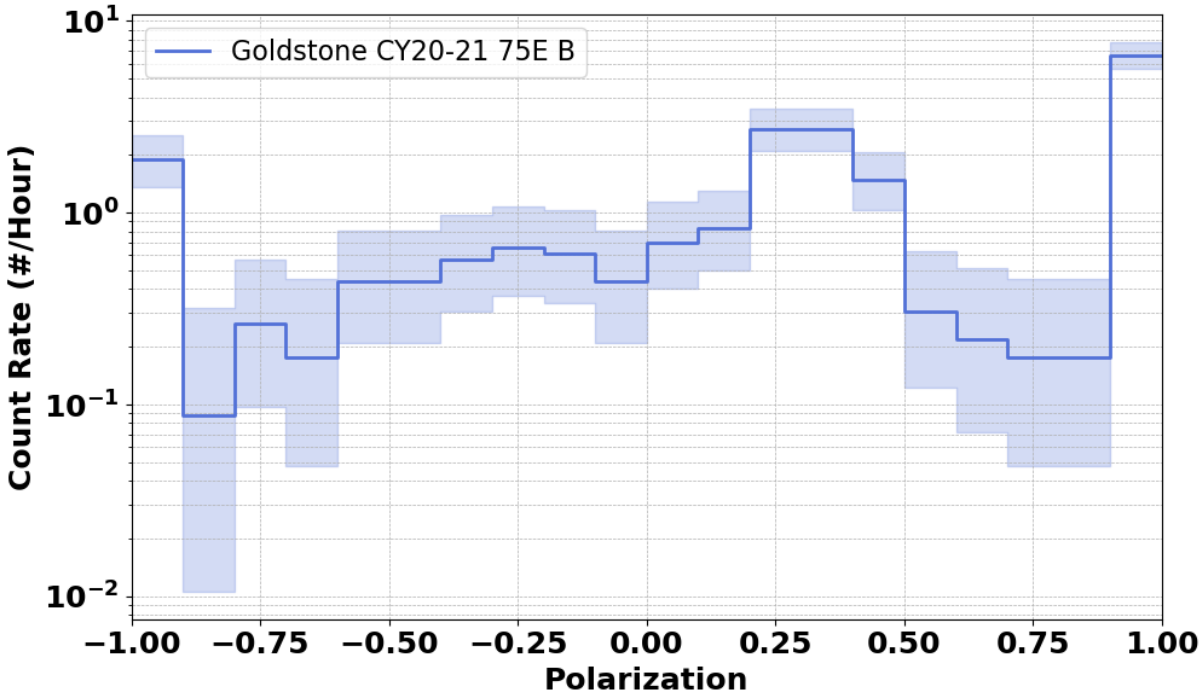

Figure D-7. Count rate versus polarization of Goldstone CY2020–2021, pointing B.

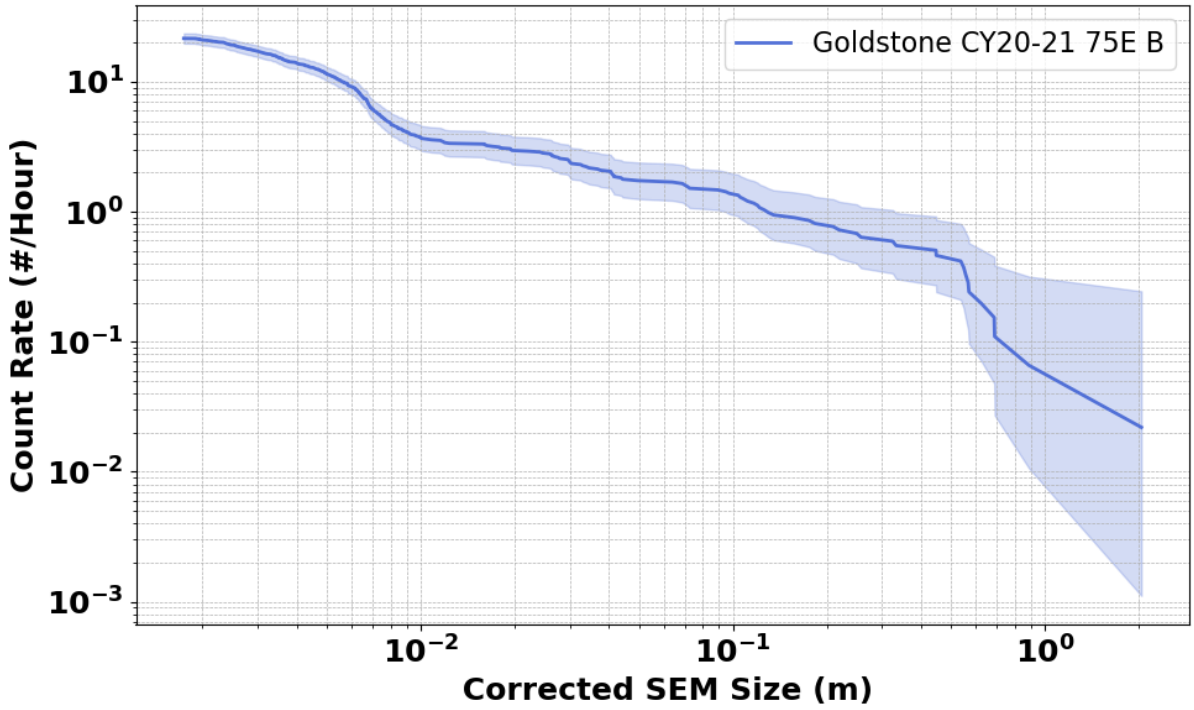

Figure D-8. Cumulative count rate versus SEM size of Goldstone CY2020–2021, pointing B.

Appendix E: CY2020–2021, Pointing C

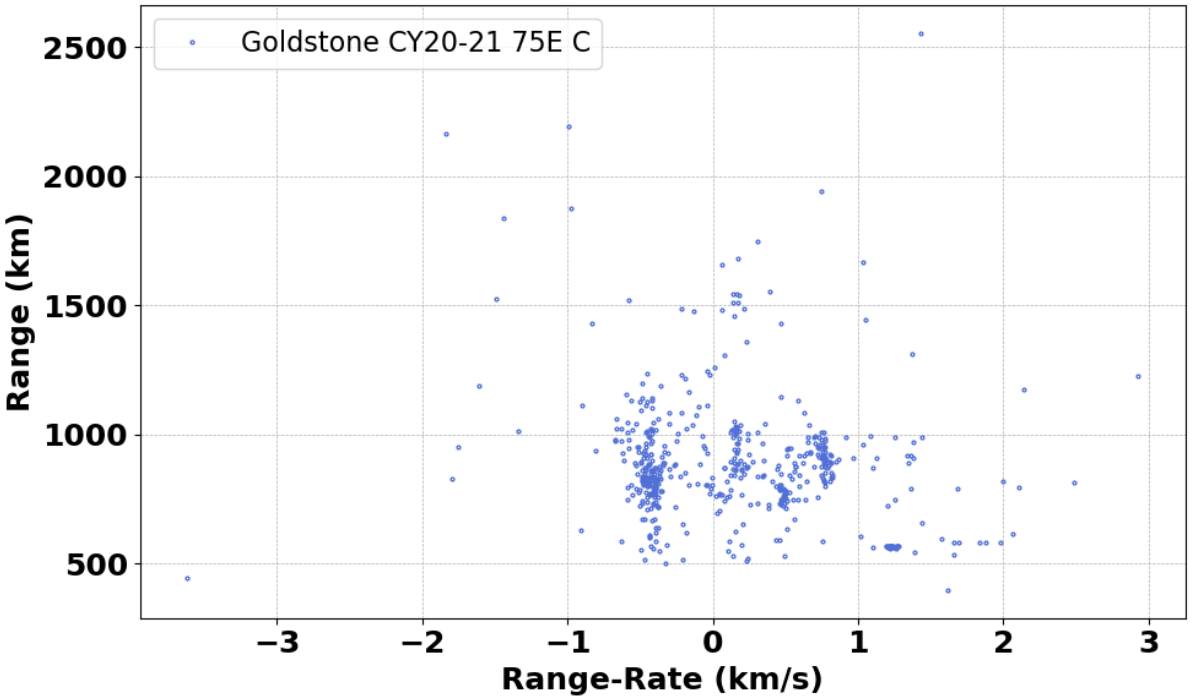

Figure E-1. Range versus range-rate of Goldstone CY2020–2021, pointing C.

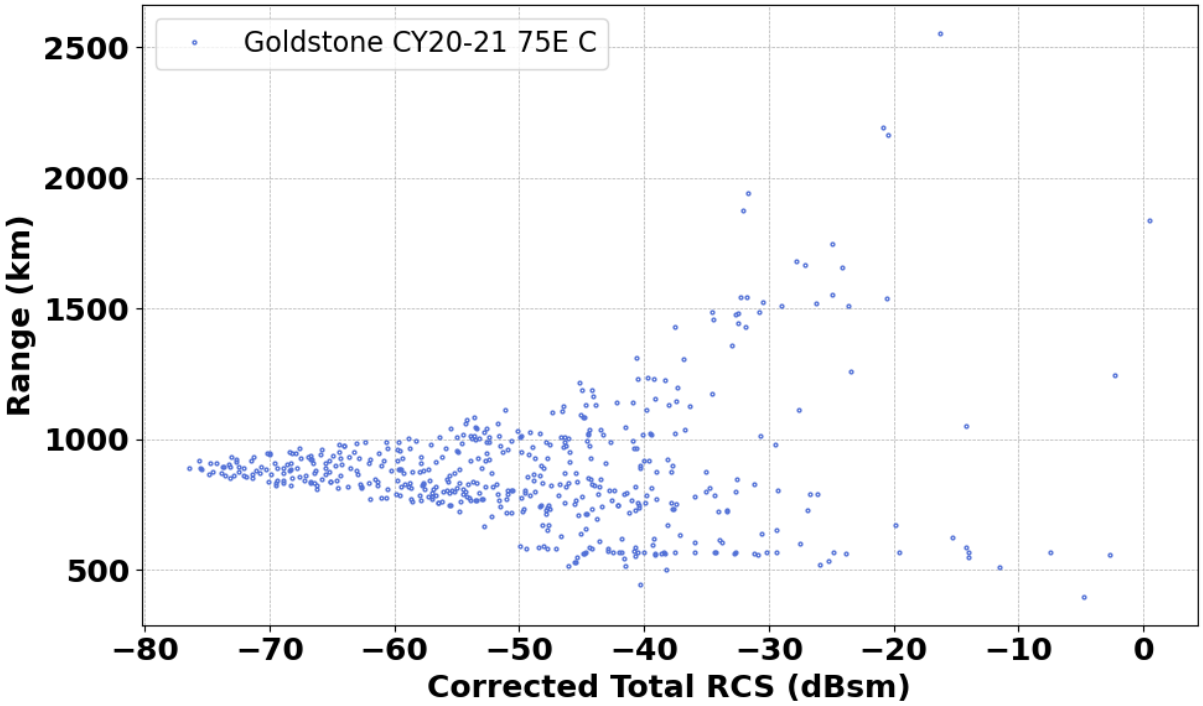

Figure E-2. Range versus total RCS of Goldstone CY2020–2021, pointing C.

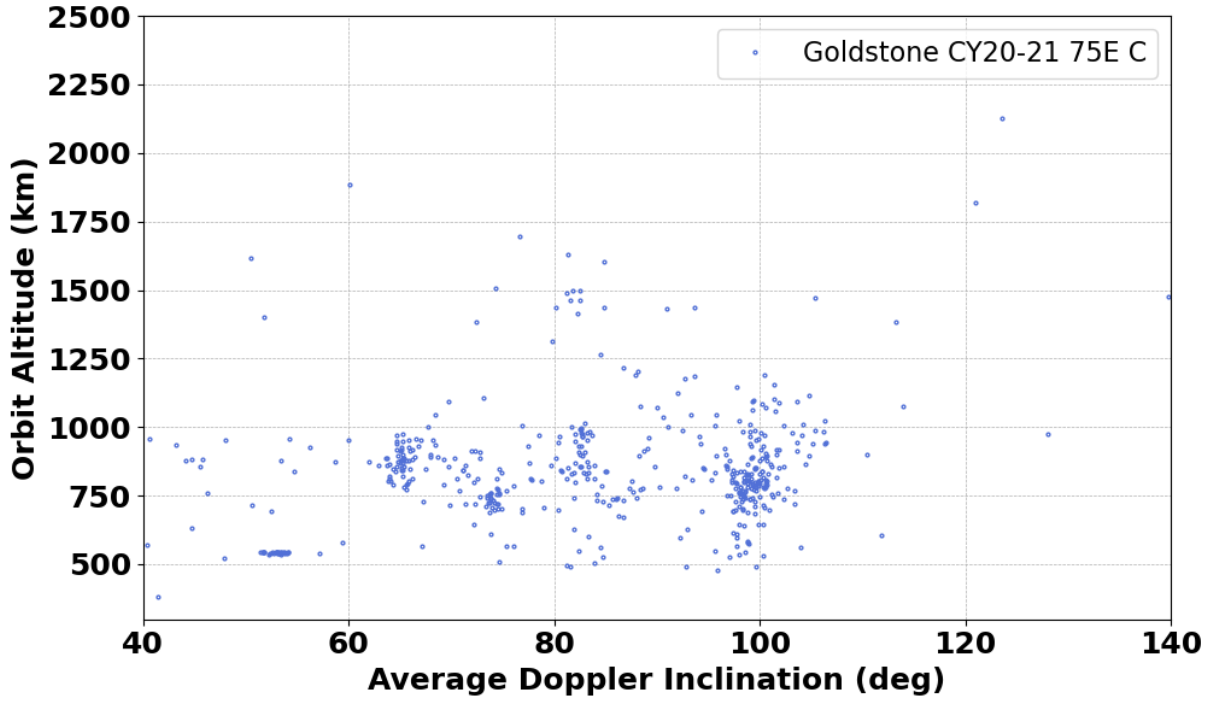

Figure E-3. Orbit altitude versus average Doppler inclination of Goldstone CY2020–2021, pointing C.

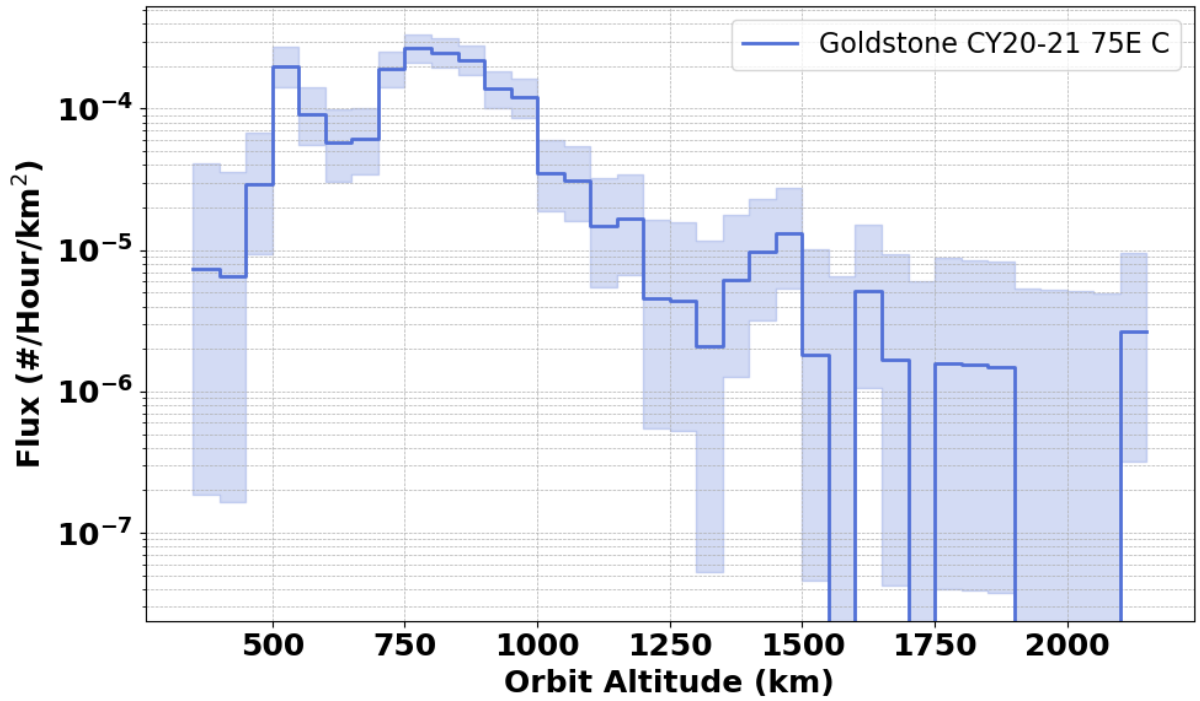

Figure E-4. Flux versus orbit altitude of Goldstone CY2020–2021, pointing C.

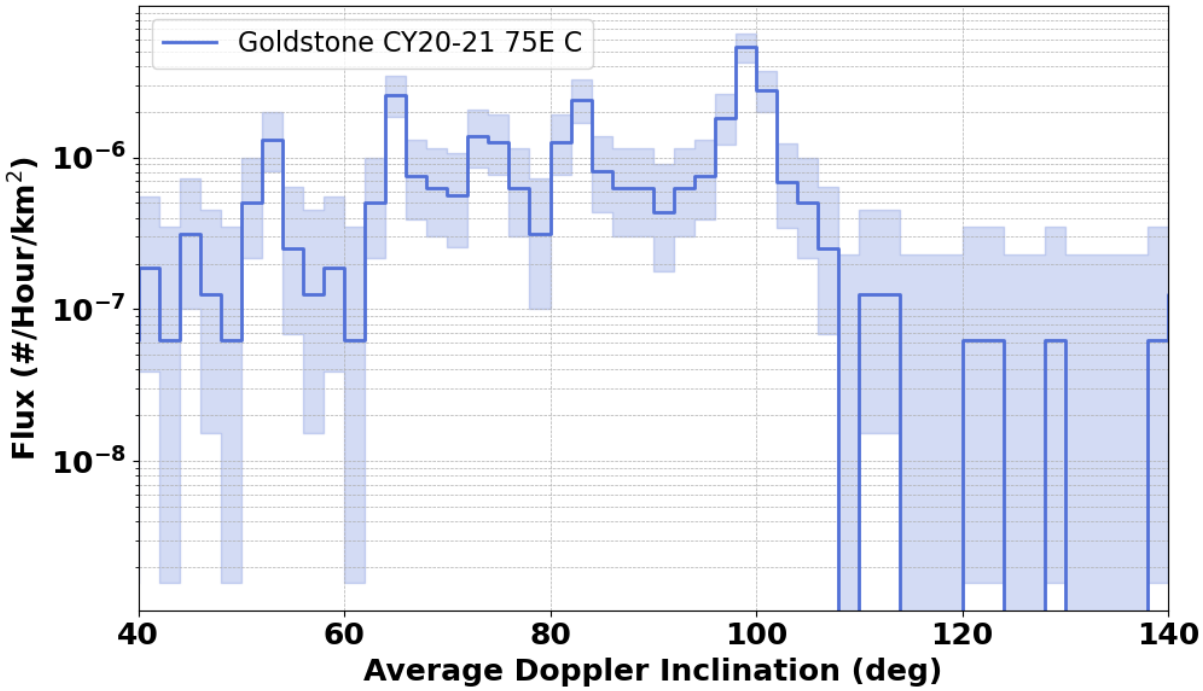

Figure E-5. Flux versus average Doppler inclination of Goldstone CY2020–2021, pointing C.

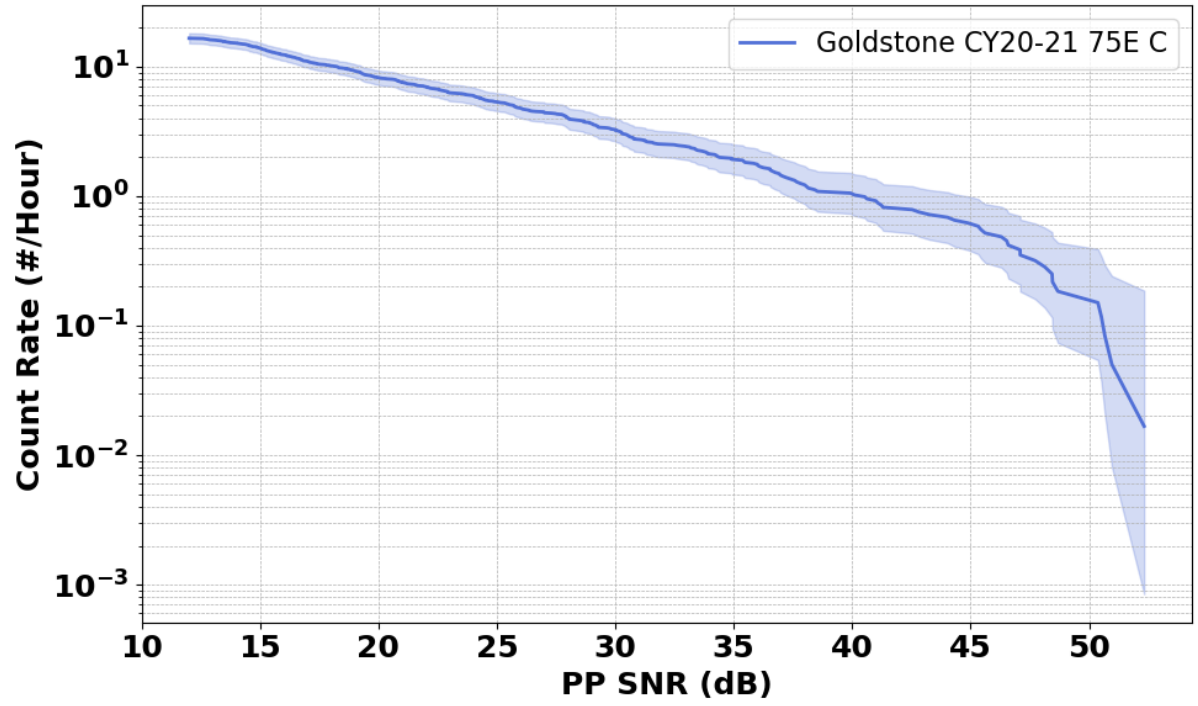

Figure E-6. Cumulative count rate versus PP SNR of Goldstone CY2020–2021, pointing C.

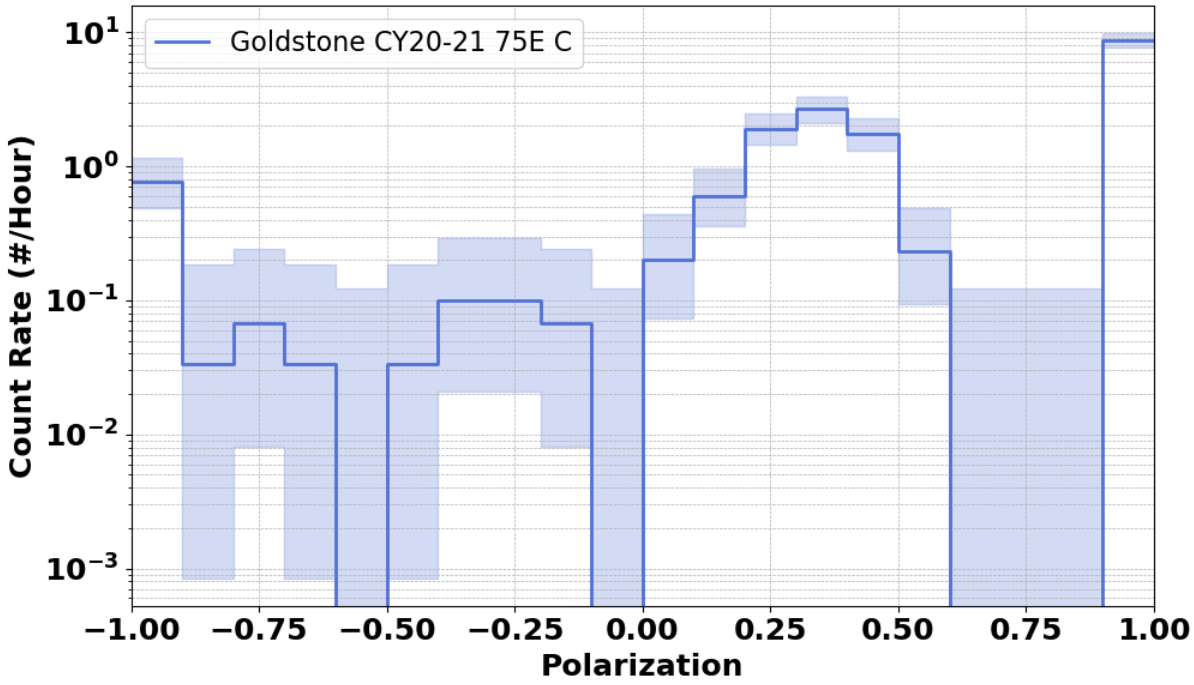

Figure E-7. Count rate versus polarization of Goldstone CY2020–2021, pointing C.

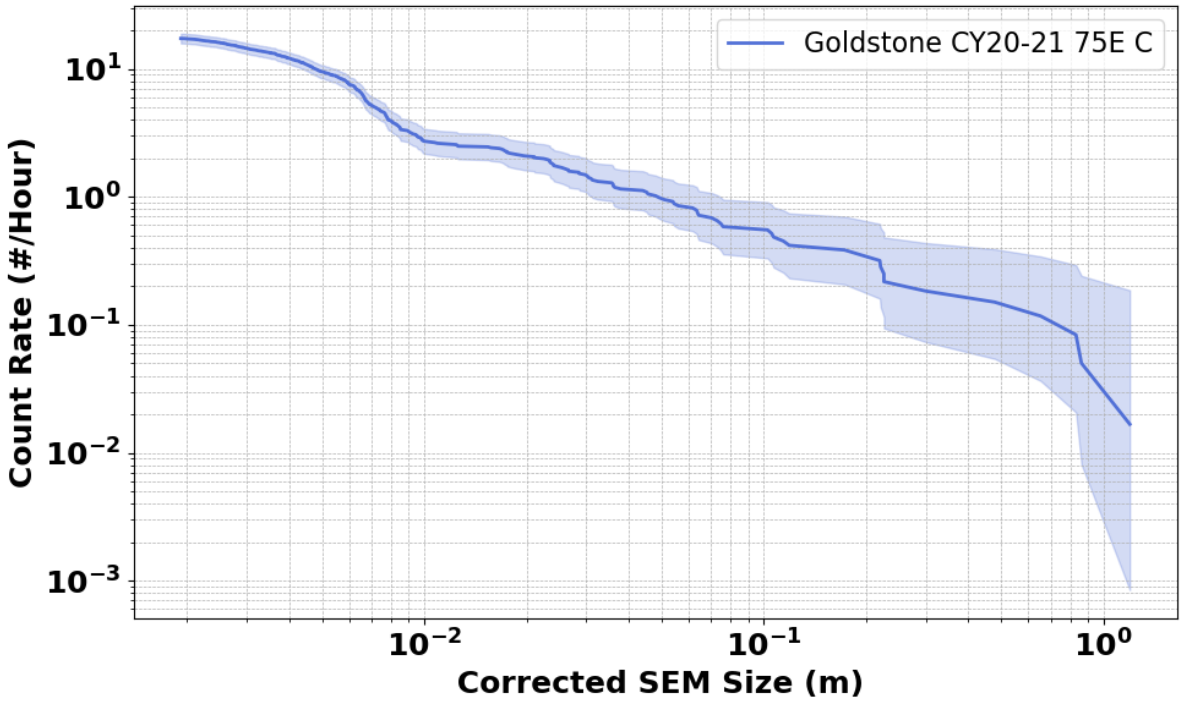

Figure E-8. Cumulative count rate versus SEM size of Goldstone CY2020–2021, pointing C.

Appendix F: CY2020–2021, Pointing D

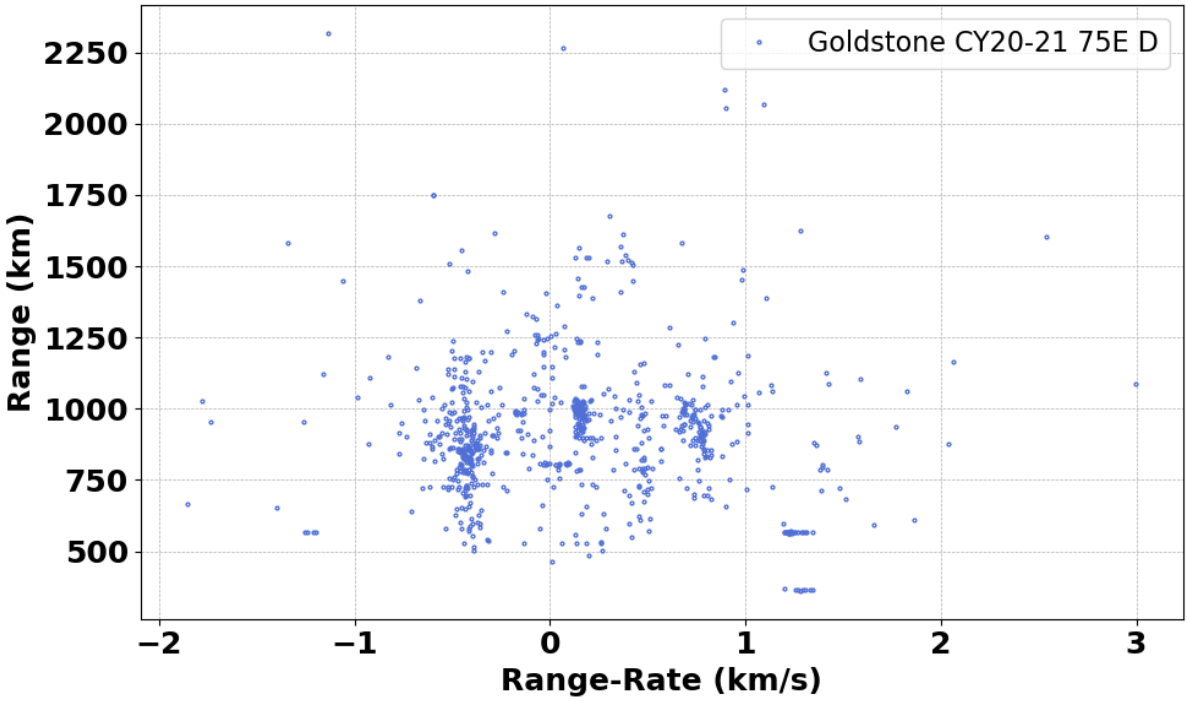

Figure F-1. Range versus range-rate of Goldstone CY2020–2021, pointing D.

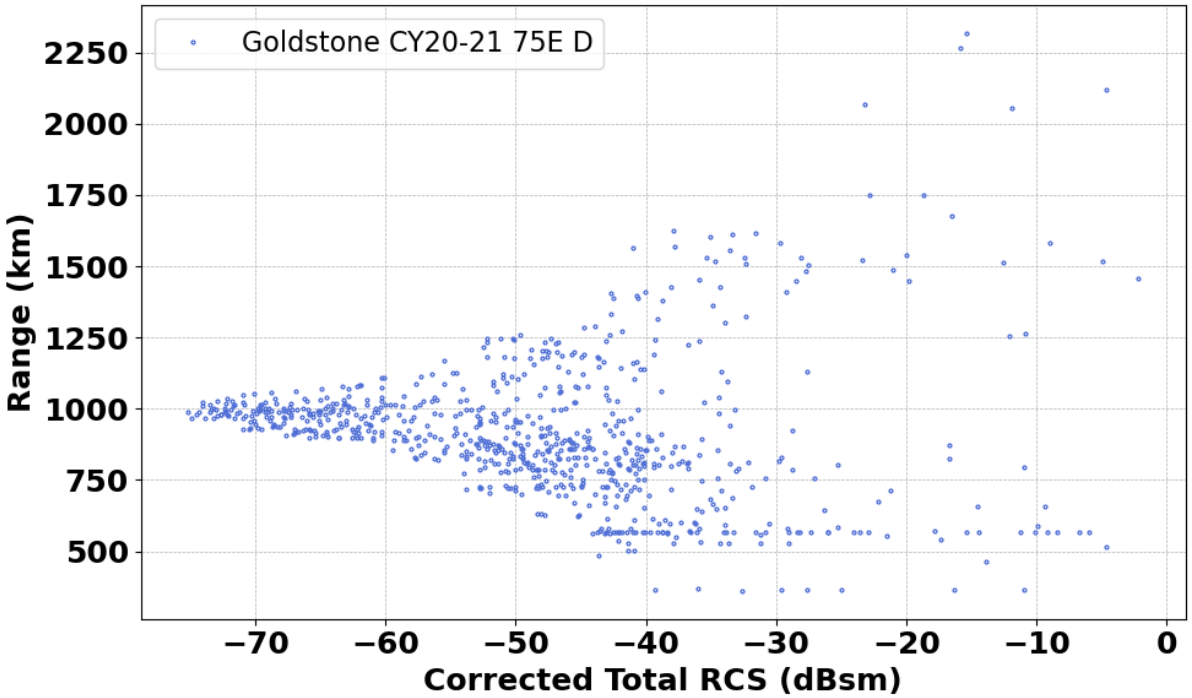

Figure F-2. Range versus total RCS of Goldstone CY2020–2021, pointing D.

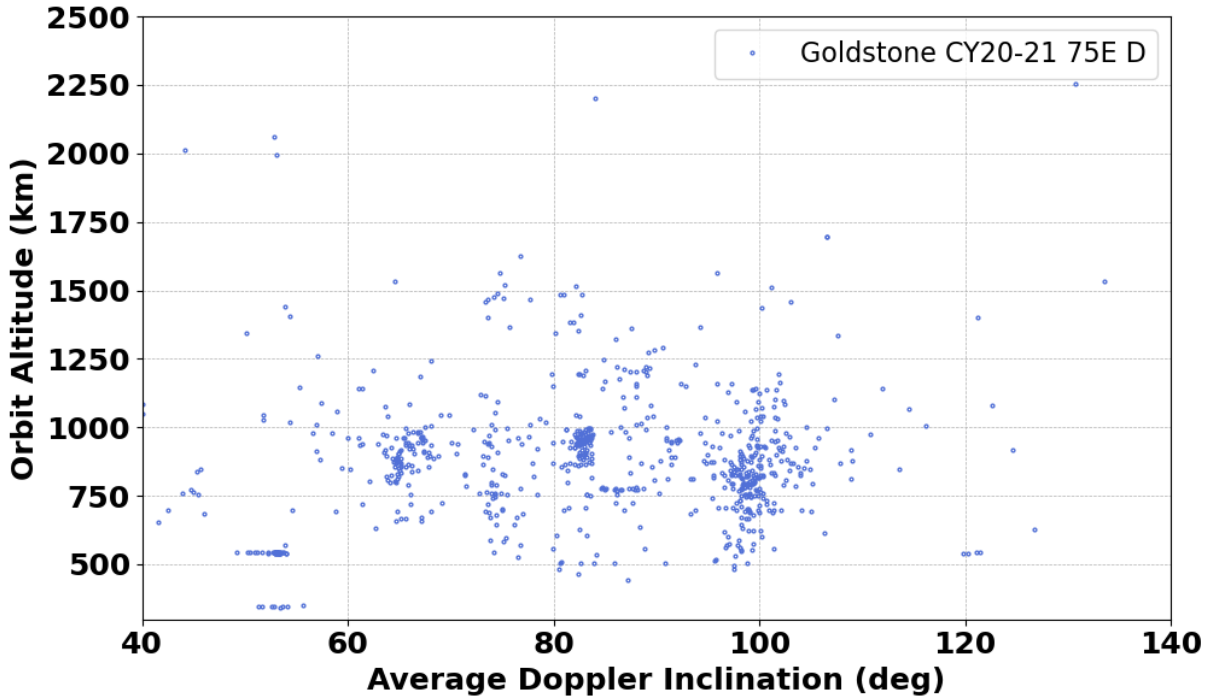

Figure F-3. Orbit altitude versus average Doppler inclination of Goldstone CY2020–2021, pointing D.

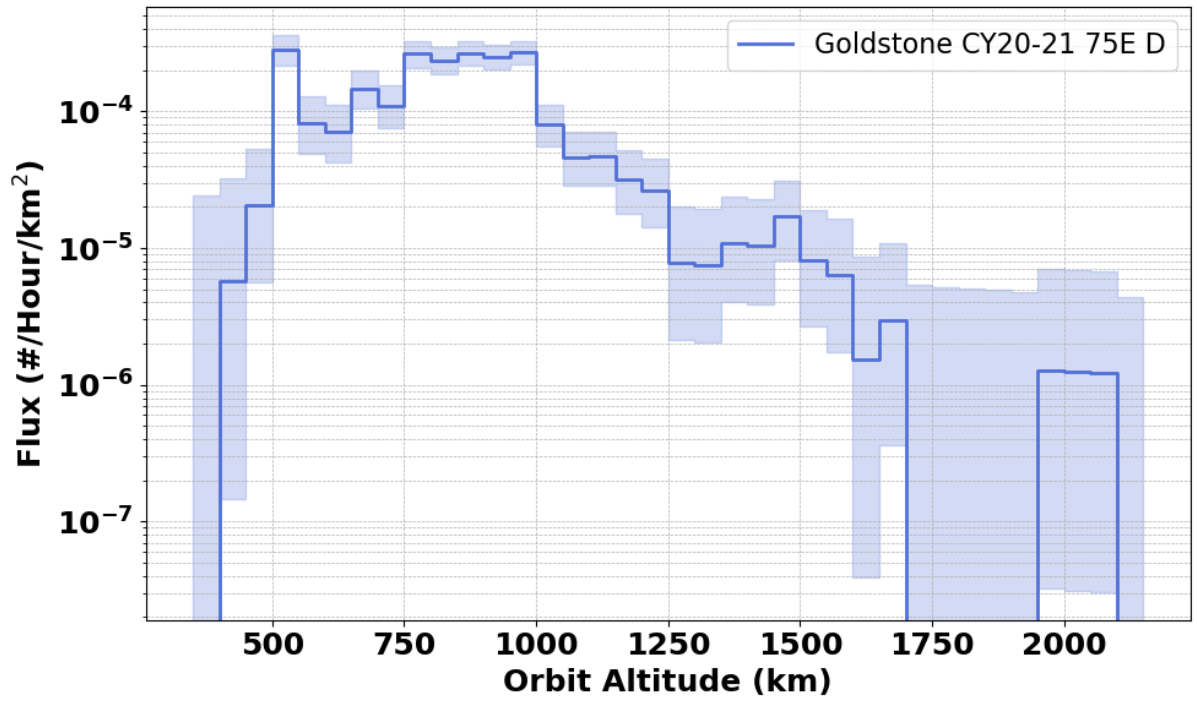

Figure F-4. Flux versus orbit altitude of Goldstone CY2020–2021, pointing D.

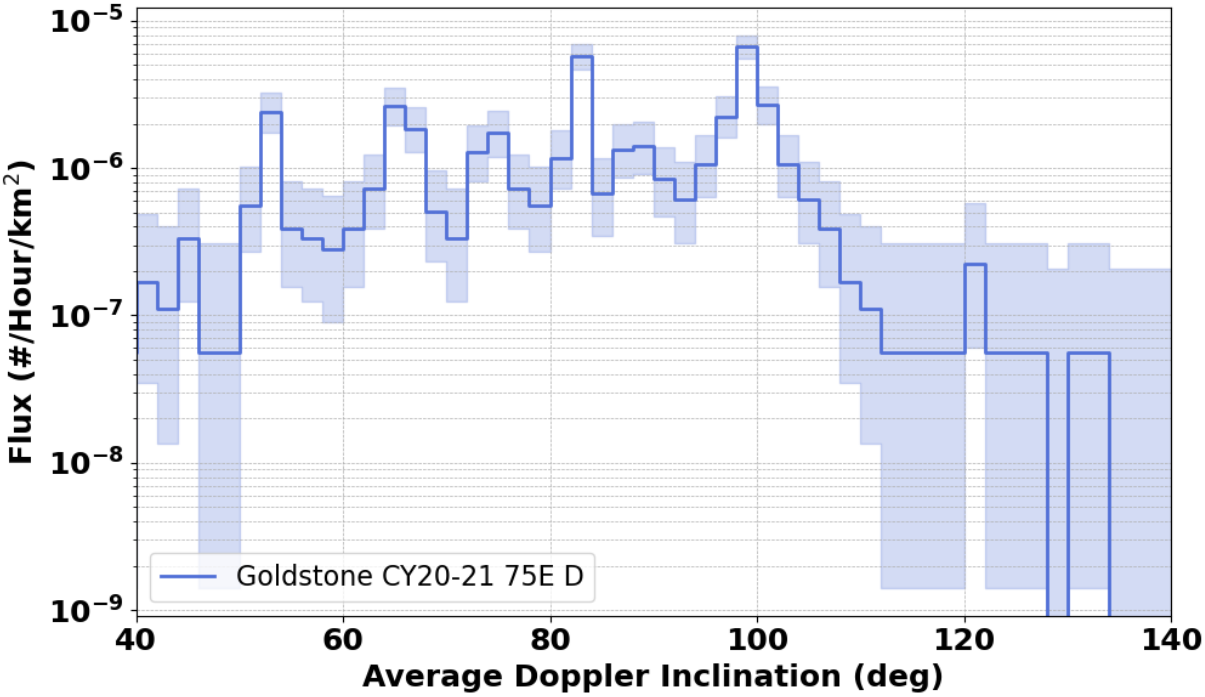

Figure F-5. Flux versus average Doppler inclination of Goldstone CY2020–2021, pointing D.

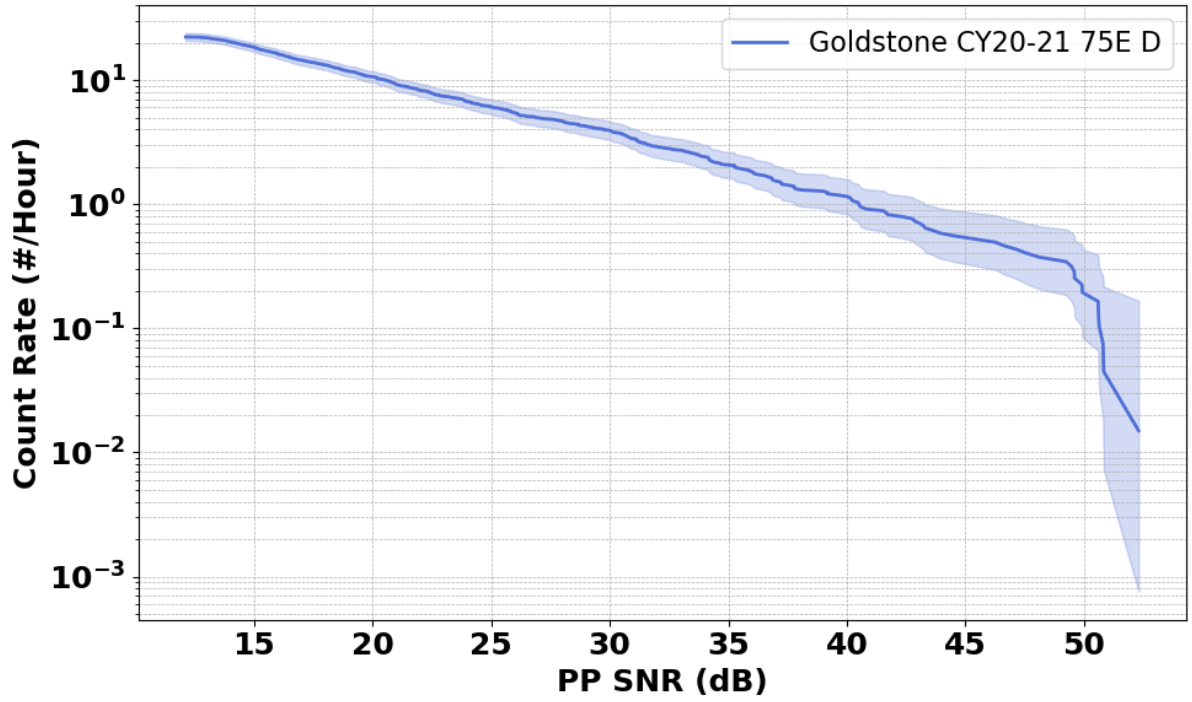

Figure F-6. Cumulative count rate versus PP SNR of Goldstone CY2020–2021, pointing D.

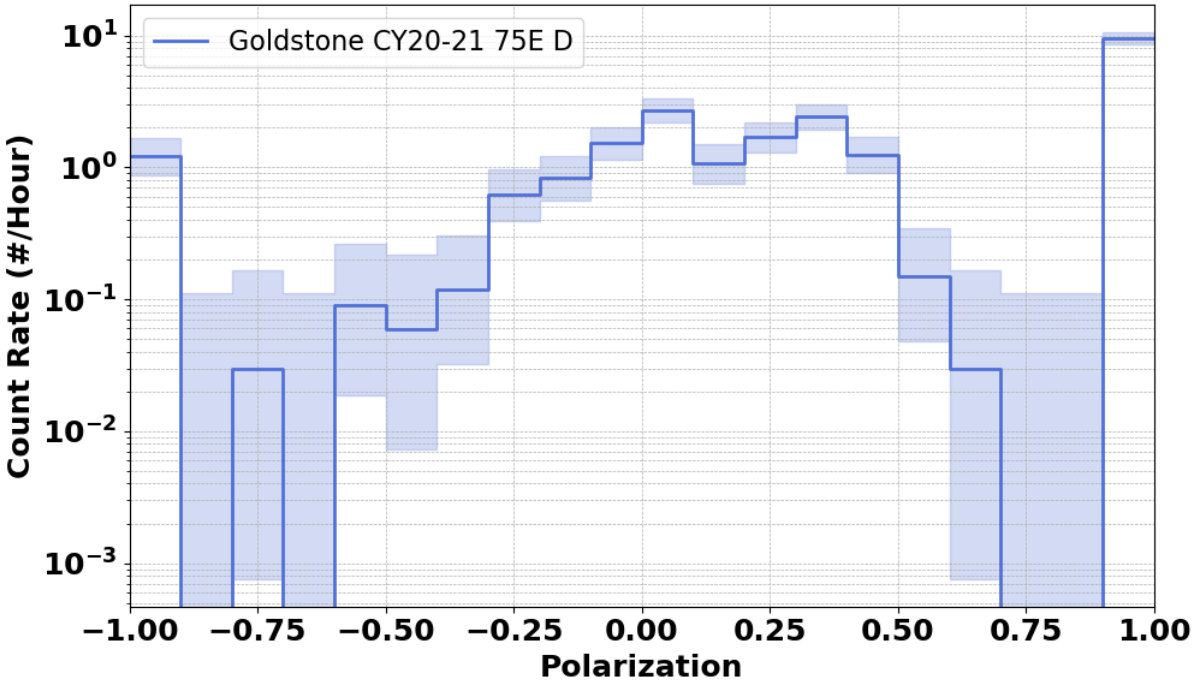

Figure F-7. Count rate versus polarization of Goldstone CY2020–2021, pointing D.

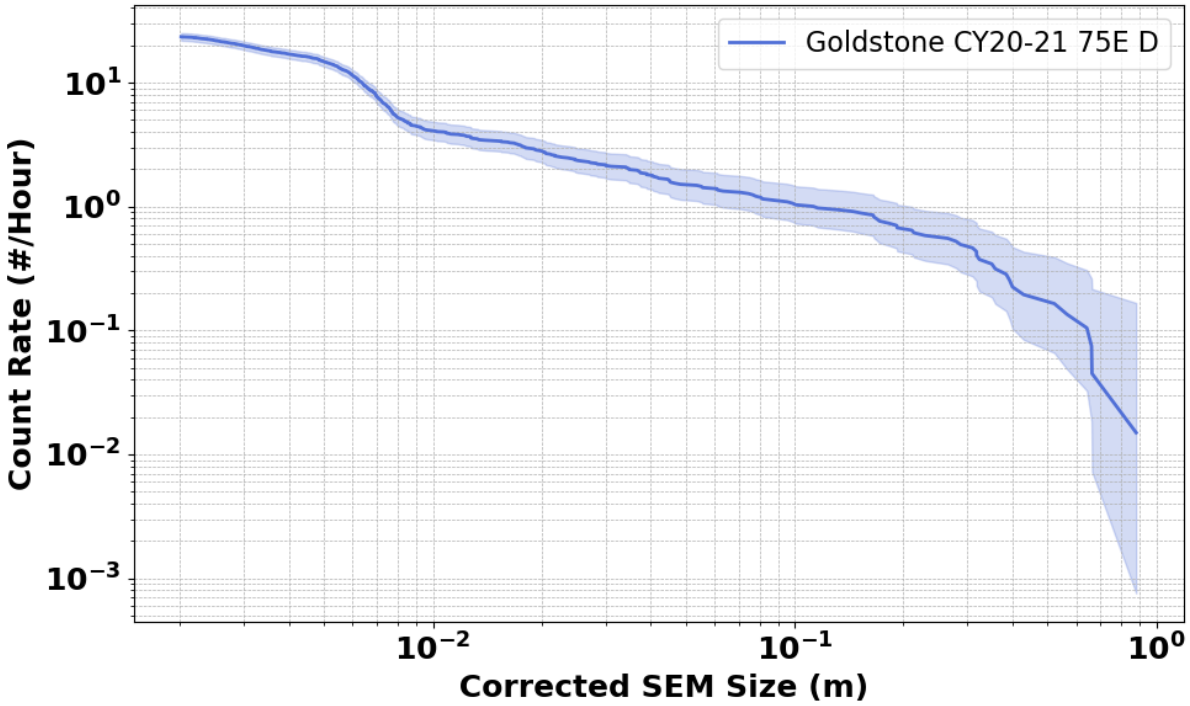

Figure F-8. Cumulative count rate versus SEM size of Goldstone CY2020–2021, pointing D.

Appendix G: CY2020–2021, 800 km

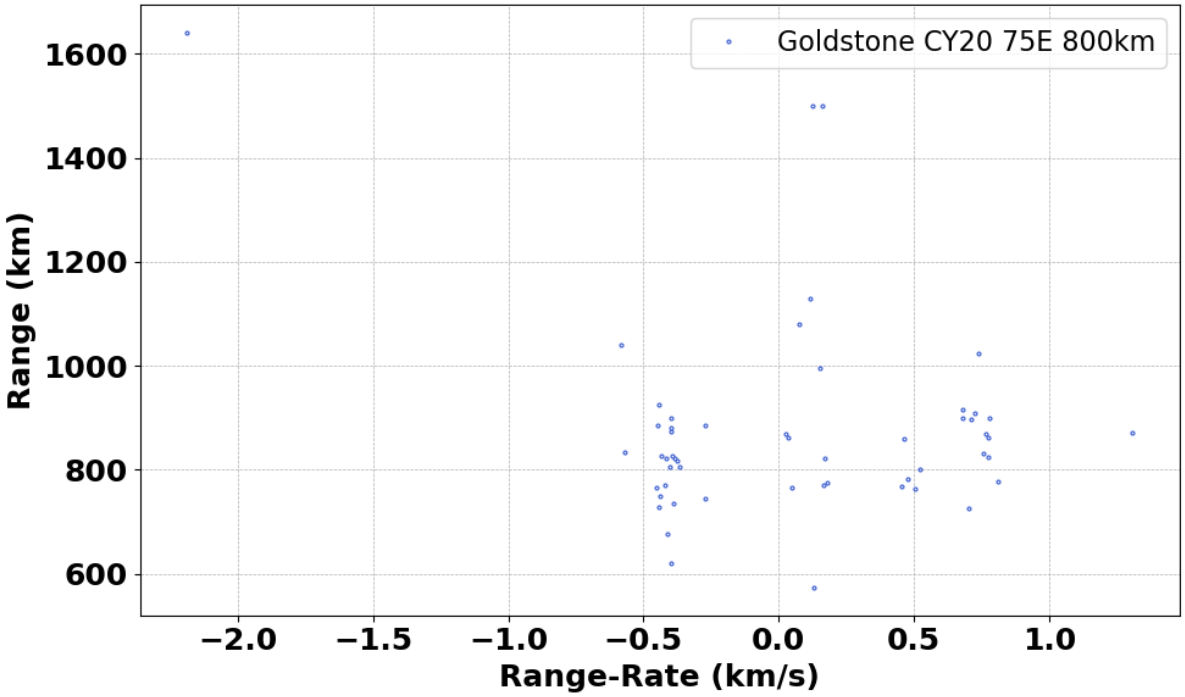

Figure G-1. Range versus range-rate of Goldstone CY2020–2021, pointing 800 km.

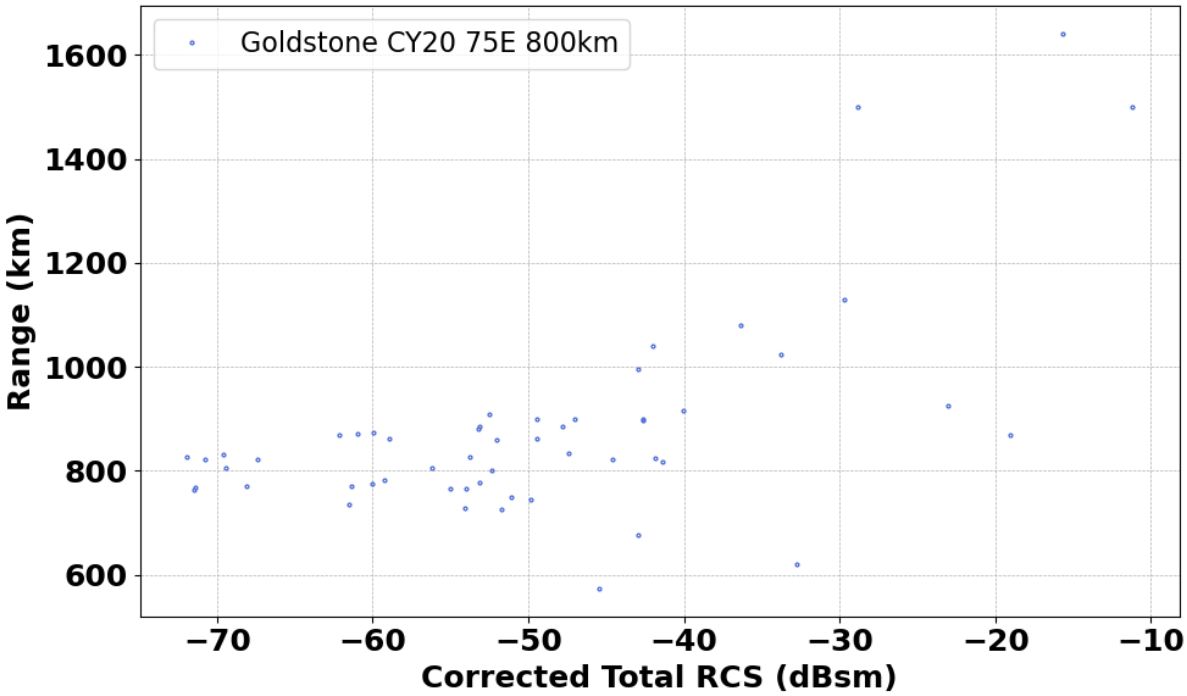

Figure G-2. Range versus total RCS of Goldstone CY2020–2021, pointing 800 km.

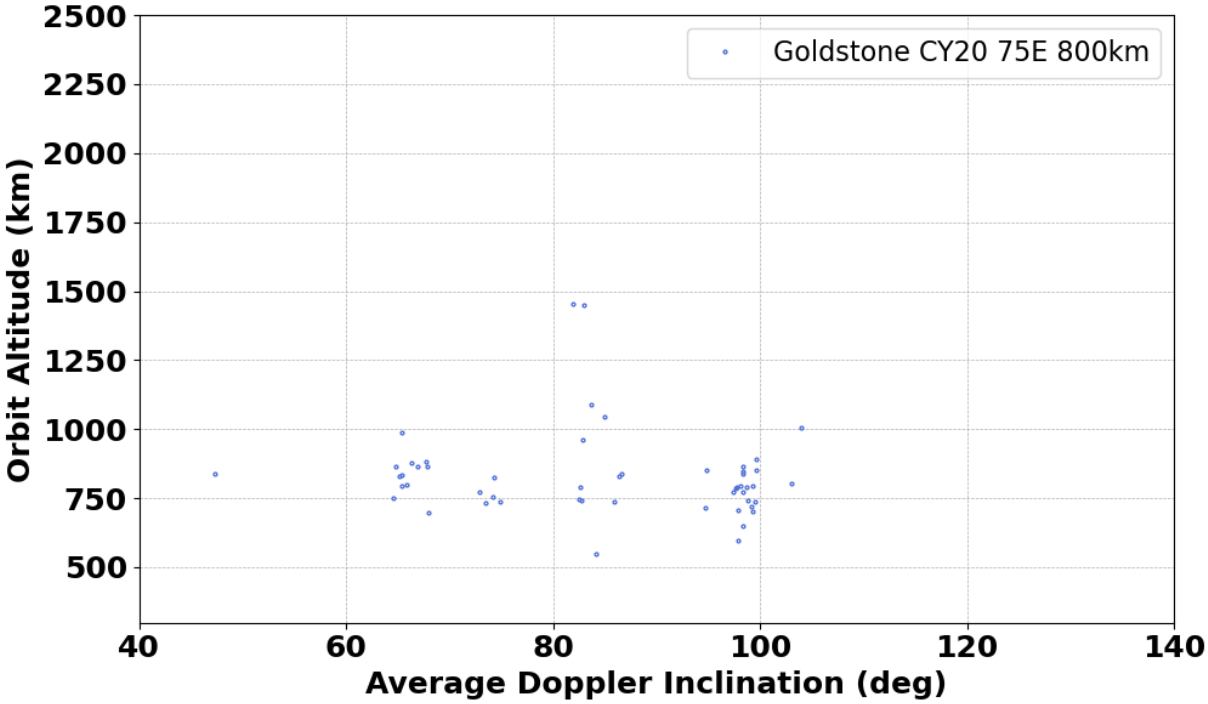

Figure G-3. Orbit altitude versus average Doppler inclination of Goldstone CY2020–2021, pointing 800 km.

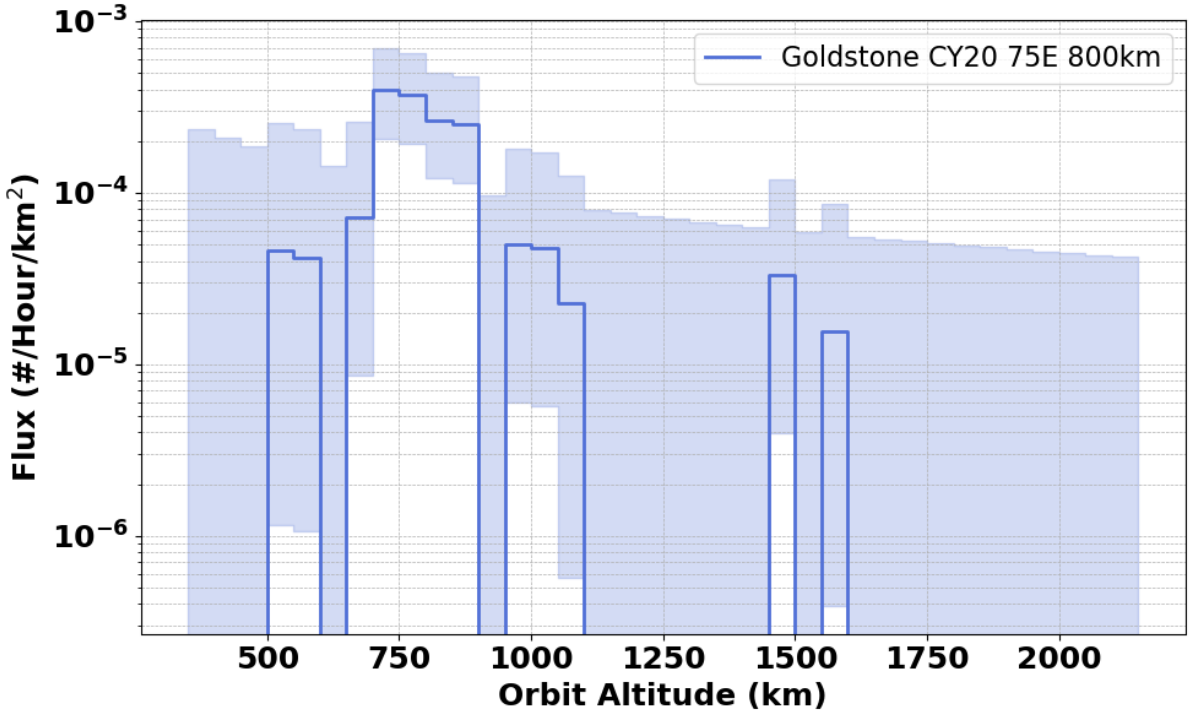

Figure G-4. Flux versus orbit altitude of Goldstone CY2020–2021, pointing 800 km.

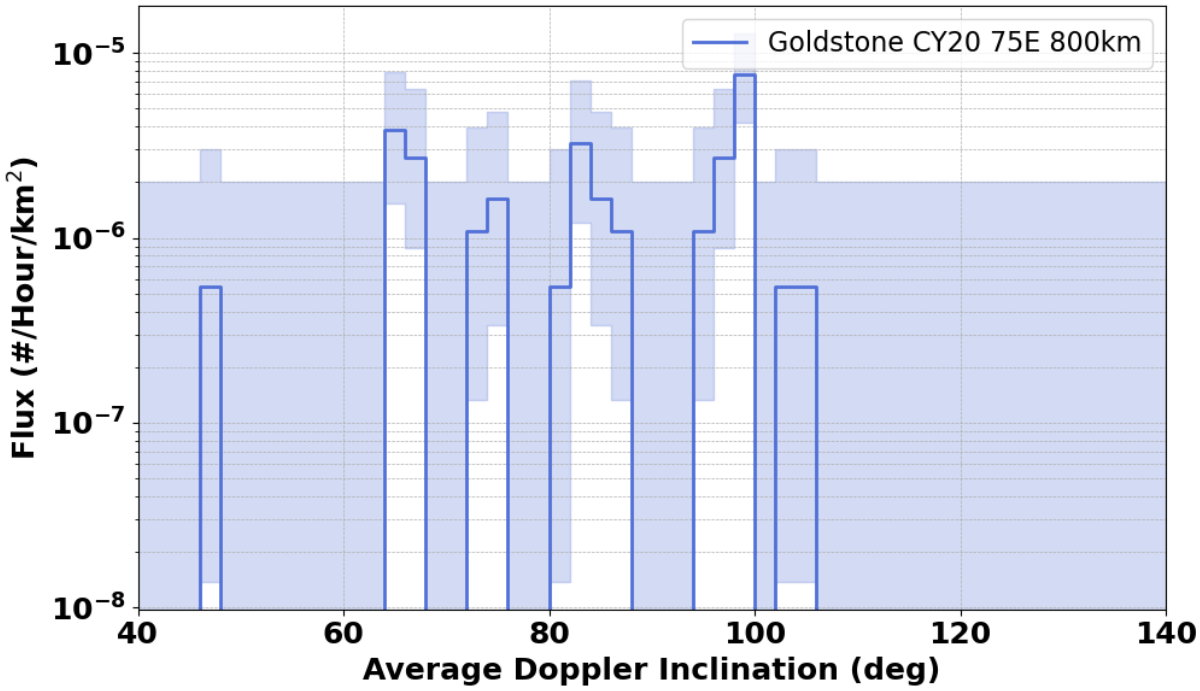

Figure G-5. Flux versus average Doppler inclination of Goldstone CY2020–2021, pointing 800 km.

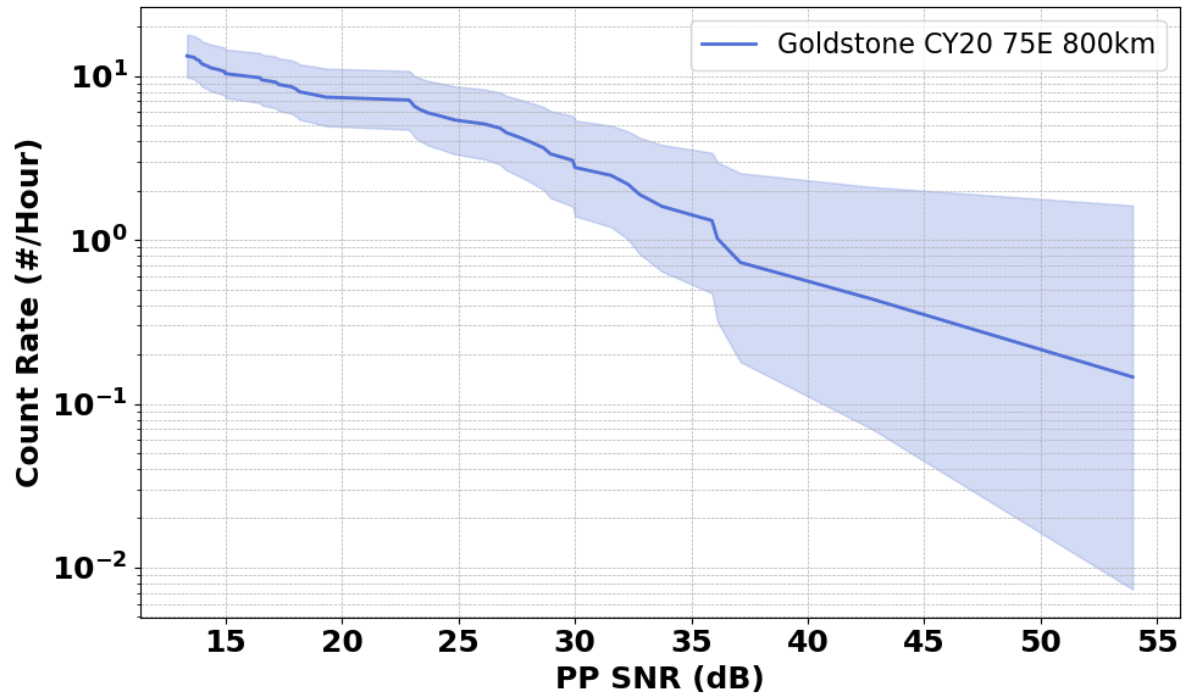

Figure G-6. Cumulative count rate versus PP SNR of Goldstone CY2020–2021, pointing 800 km.

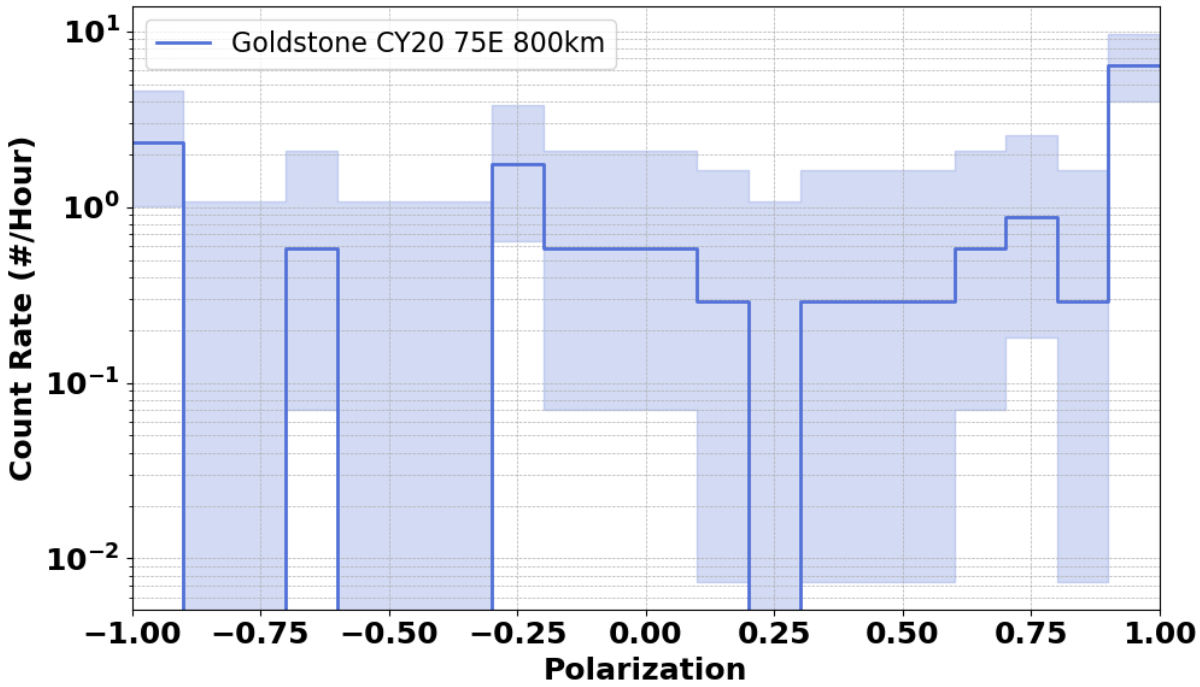

Figure G-7. Count rate versus polarization of Goldstone CY2020–2021, pointing 800 km.

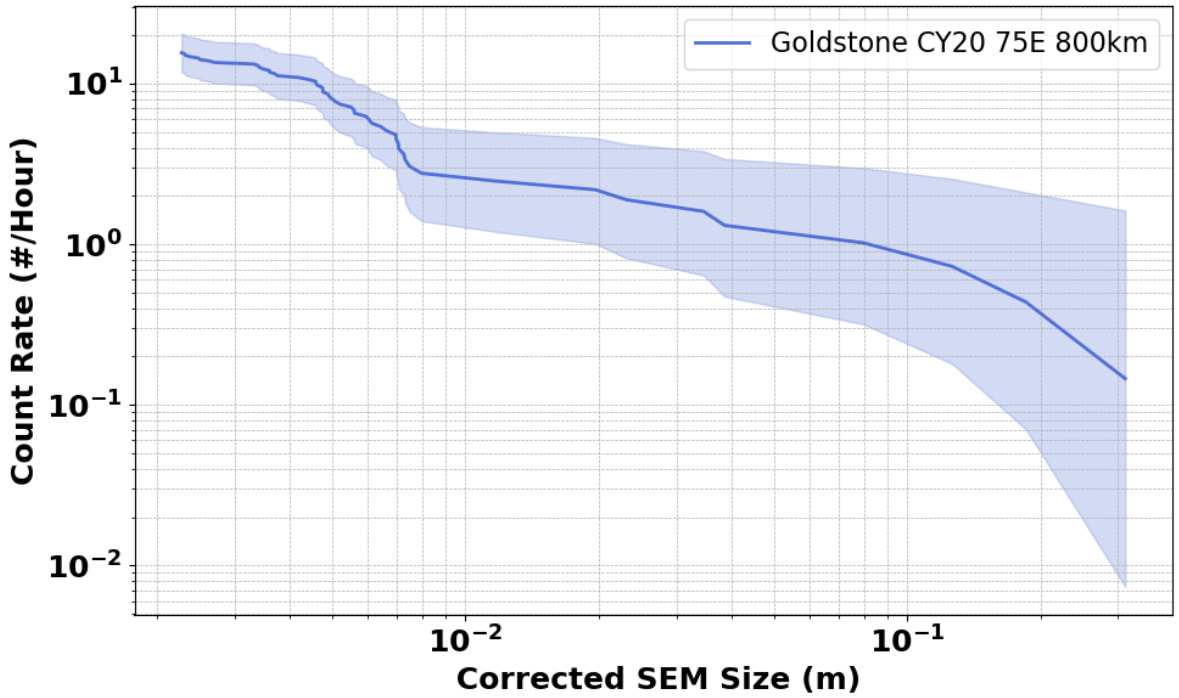

Figure G-8. Cumulative count rate versus SEM size of Goldstone CY2020–2021, pointing 800 km.

Appendix H: SNR-Weighted Range Estimator

The Goldstone radar provides two independent receiver channels for each measurement of an OD object that passes through the beam – a PP and OP channel. This section reviews a method for combining the range estimates from each channel to generate results that perform as well, and in many instances, better than a single channel estimate of the range.

The range estimates provided by measurements from the PP and OP channels may be modeled as a superposition of the true range, *R*, and a noise term. Each of the noise terms are assumed to be independent, zero mean, additive white Gaussian noise, although the noise variance or average noise power in each channel may be different. Including the noise terms, the estimated range for each channel may be written as shown in Equations H-1 and 2, where *R* is the true range and *W* is a normally distributed random variable representing the noise contribution to the range measured in each channel.

$$R_{PP} = R + W_{PP} \quad \text{H-1}$$

$$R_{OP} = R + W_{OP} \quad \text{H-2}$$

Verification of at least equal means for the noise terms in both channels is done by considering the difference between the range estimates or range residuals, which results in the true range to the object canceling out of the difference. Verifying that the mean for the underlying range residual distribution, $\mu_{diff} = 0$, is depicted in Equation H-3.

$$R_{PP} - R_{OP} = W_{PP} - W_{OP} \sim N(\mu_{diff} = 0, \sigma_{diff}^2) \quad \text{H-3}$$

Residuals for all the detections in CY2018 are distributed as shown in Figure H-1, with the sample mean = 0.0328 km. Using the assumption of normal distributed residuals; the sampling distribution for the sample mean is described in Equation H-4, where *n* is the number of range residuals observed. Using the sample variance as an estimate for the unknown variance, 95% confidence intervals are constructed using t-distribution based upper and lower bounds for the interval. The resulting 95% confidence interval is [0.0233, 0.0422] km, showing a slight positive bias between the range estimates produced between the 2 channels of about 33 meters. This may be the result of an occasional single sample timing slip in the synchronization between the PP and OP channels, a jitter in the clocks used by the respective receivers, or the actual peak of the radar return occurring between samples. Given that the DSN employs considerable effort to ensure frequency stability and timing synchronization, the latter rationale is most likely [20].

Goldstone uses a 1.5 MHz sample rate, which produces a 0.6667 μs time difference between samples. This translates into a slant range offset of 99.93 meters between samples, indicating that the bias is about one-third of the time between samples. The bias is very small compared to the range resolution of approximately 500 meters for the Goldstone waveform. Based on this result, the population mean of the range residuals is approximately zero.

$$\bar{X} \sim N\left(\mu_{diff}, \frac{\sigma_{diff}^2}{n}\right) \quad \text{H-4}$$

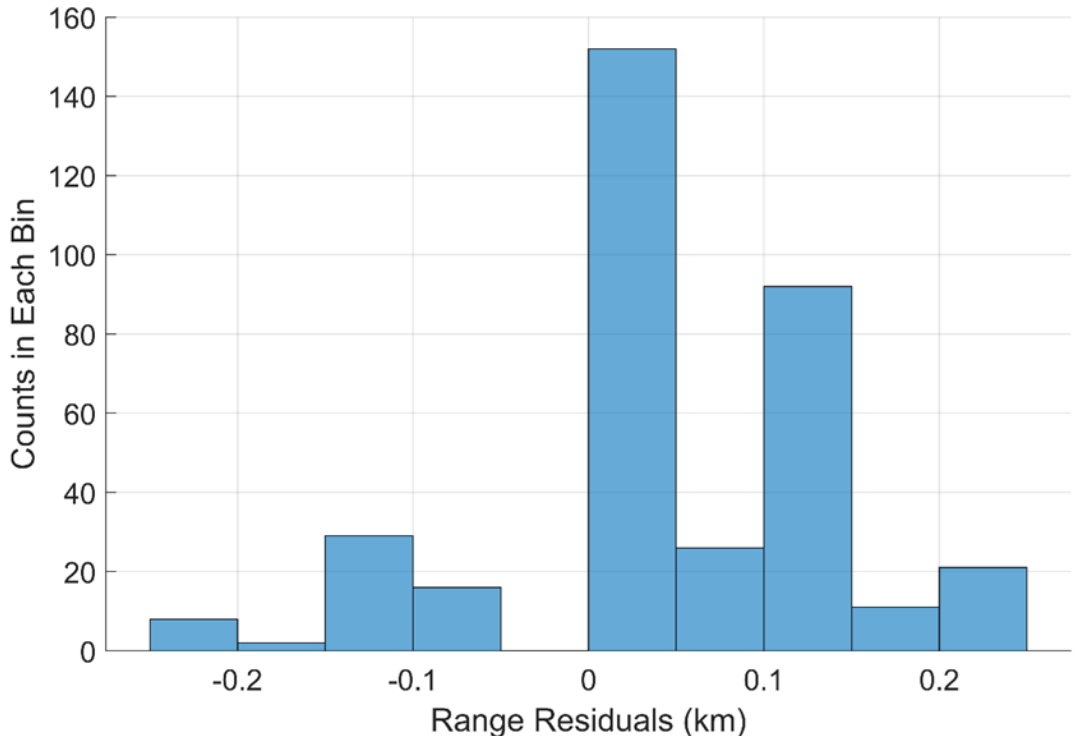

Figure H-1. Histogram of range residuals for the Goldstone CY2018 data.
Only detections having both a PP and OP channel response were used to form the range residuals shown.

Minimum Mean Square Error Estimator

Examining a simple average of the range estimates for both the PP and OP channels generates the estimator described in Equation H-5.

$$\hat{R} = \frac{1}{2}(R_{PP} + R_{OP}) \tag{H-5}$$

The expected value and variance for this estimator is described in Equations H-6 and H-7, where the independent estimates of the range with the PP and OP channels, *i.e.*, the covariance term in Equation H-7, is zero. The result is an unbiased estimator, as shown in Equation H-6, *e.g.*, the estimator produces the actual range on average. If the noise in the PP and OP channels is the same, the variance in the range estimate is reduced by one-half. The mean square error (MSE) is the sum of the estimator bias and variance, which for an unbiased estimator, is simply the variance of the estimator as described in Equation H-8 [21] [22].

$$E(\hat{R}) = \frac{1}{2}E(R_{PP} + R_{OP}) = R \tag{H-6}$$

$$Var(\hat{R}) = \frac{1}{4}[Var(R_{PP}) + Var(R_{OP}) + 2Cov(R_{PP}, R_{OP})] = \frac{1}{4}(\sigma_{PP}^2 + \sigma_{OP}^2) \tag{H-7}$$

$$MSE(\hat{R}) = Var(\hat{R}) + Bias(\hat{R}) = Var(\hat{R}) \tag{H-8}$$

The downside of using a simple average for the estimator is that if one of the estimates is significantly noisier, the result is an MSE that may be worse than if a single channel is used. As an alternative, the well-known inverse variance weighted average or simply SNR-weighted average estimator can be used to correct this. Consider a linear combination of range estimates as shown in Equation H-9 with the constraint that the coefficients sum to one. This estimator is unbiased, and the MSE is found by the variance of the estimator as shown in Equations H-10 and H-11. To find the ideal α, consider identifying an α that minimizes the MSE. This is a simple optimization problem, and the derivative with respect to α is taken and set to zero, resulting in the value for α shown in Equation H-12. A second derivative test may be used to verify that this value of α minimizes the MSE.

$$\hat{R} = \alpha R_{PP} + (1-\alpha) R_{OP} \tag{H-9}$$

$$E(\hat{R}) = \alpha E(R_{PP}) + (1-\alpha) E(R_{OP}) = R \tag{H-10}$$

$$MSE(\hat{R}) = Var(\hat{R}) + Bias(\hat{R}) = Var(\hat{R}) = \alpha^2 \sigma_{PP}^2 + (1-\alpha)^2 \sigma_{OP}^2 \tag{H-11}$$

$$\alpha = \frac{\sigma_{OP}^2}{\sigma_{PP}^2 + \sigma_{OP}^2} = \frac{SNR_{PP}}{SNR_{PP} + SNR_{OP}} \tag{H-12}$$

The last relation in Equation H-12 is a result of rewriting the noise variances in terms of the SNR as depicted in Equation H-13, where E_s is the total energy in the signal and σ^2 is the average noise power.

$$SNR = \frac{E_s}{\sigma^2} \tag{H-13}$$

Simulation Results

The Goldstone system was simulated using nominal parameters described in Section 2 to examine the performance of the SNR-weighted estimator for Goldstone's results. A nonfluctuating target at 800 km slant range was assumed, which for simulation purposes, was assumed to be stationary, *i.e.*, the range-rate or Doppler is zero. Goldstone transmits an up-chirp, followed by a down-chirp and the spectrogram for an up and down-chirp pair at the receiver from an object observed at 800 km is shown in Figure H-2 and Figure H-3. In both instances, the SNR is 35.76 dB.

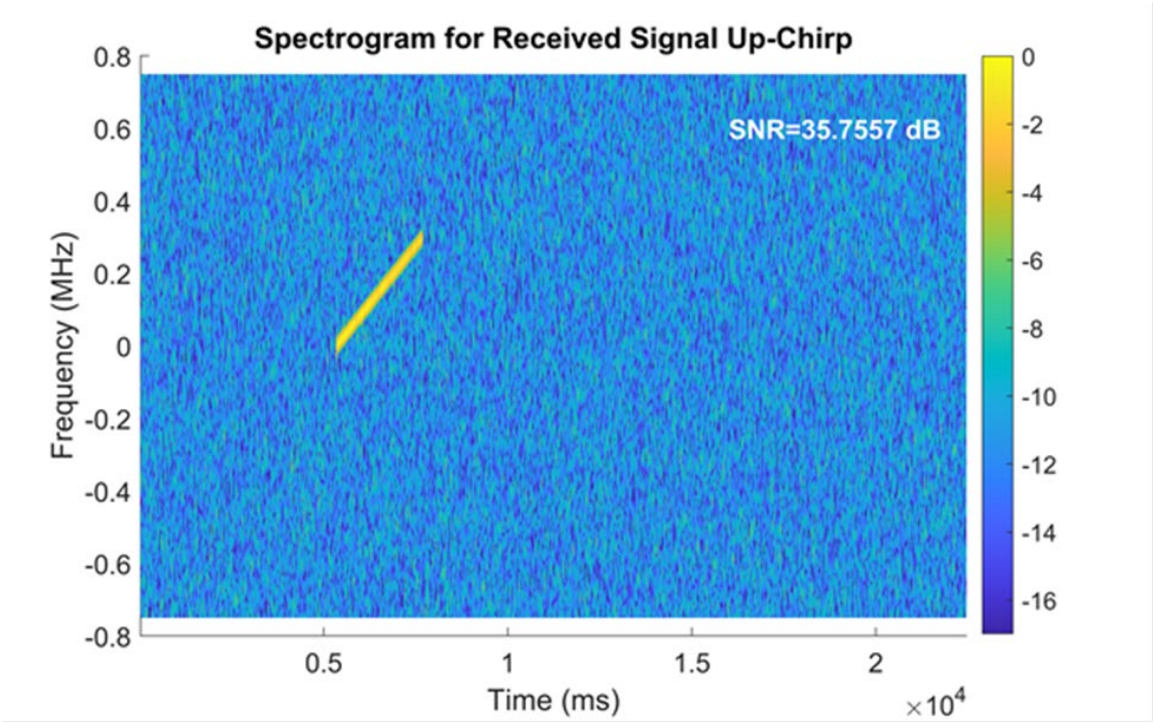

Figure H-2. Spectrogram for Goldstone up-chirp signal backscattered from an object at 800 km slant range.

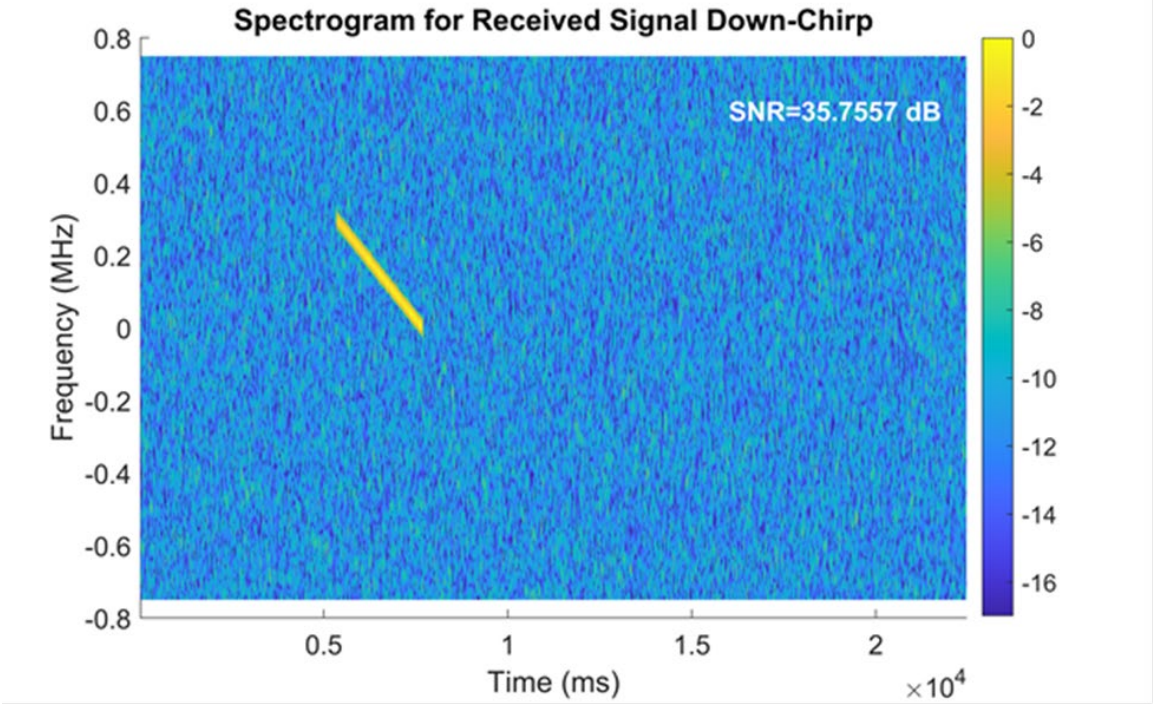

Figure H-3. Spectrogram for Goldstone down-chirp signal backscattered from an object at 800 km slant range.

The Goldstone receiver performed matched filtering for data received in both the PP and OP channels, and an example matched filter response for this system with an SNR of 35.76 dB is shown in Figure H-4. For simulation purposes, the response used was from a single pulse having the SNR stated.

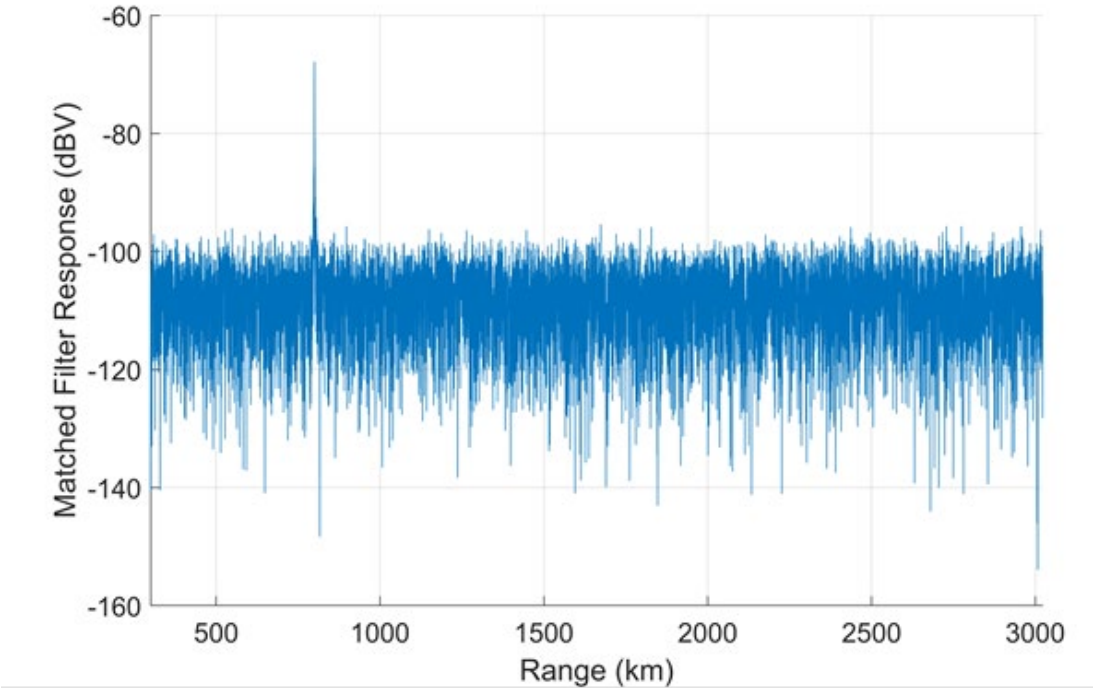

Figure H-4. Output of the matched filter for the received up-chirp backscattered from an object at 800 km slant range.

To examine the performance of the SNR-weighted range estimator, independent simulations from each of the PP and OP channels varied the SNR in each channel independently. The range error, normalized by the range resolution of the Goldstone waveform, for the PP channel range estimate under these conditions is shown in Figure H-5. The Cramer-Rao Lower Bound (CRLB) is also shown in Figure H-5 for reference purposes, since this provides the lower bound on the range error for a given SNR and the Goldstone chirp waveform [21] [22]. In general, the PP channel range estimate by itself performs well, until the SNR is less than 11.3 dB. At this point, the range estimate provided by the PP channel is no longer reliable as there is not enough SNR for an accurate measurement.

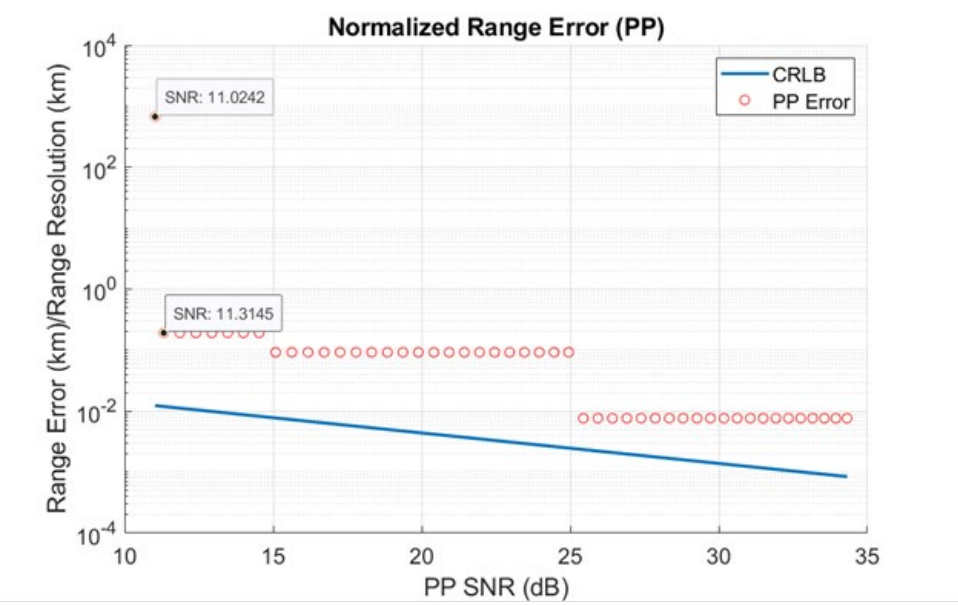

Figure H-5. Normalized range error in the PP channel.

As mentioned above, an independent OP channel estimate of the range is also available, which is plotted in Figure H-6. Also shown in Figure H-6 is the performance of the SNR-weighted range estimator, and the CRLB for the OP channel only. In all cases, the SNR for the PP channel was above that of the OP channel. For all cases above approximately 11.3 dB, the SNR-weighted range estimator provides a better range estimate than the OP channel alone. By combining the OP and PP channel estimates, better range estimates are possible than by using the OP channel alone. These are the cases where the SNR-weighted range estimator error is below the CRLB for a given OP channel SNR.

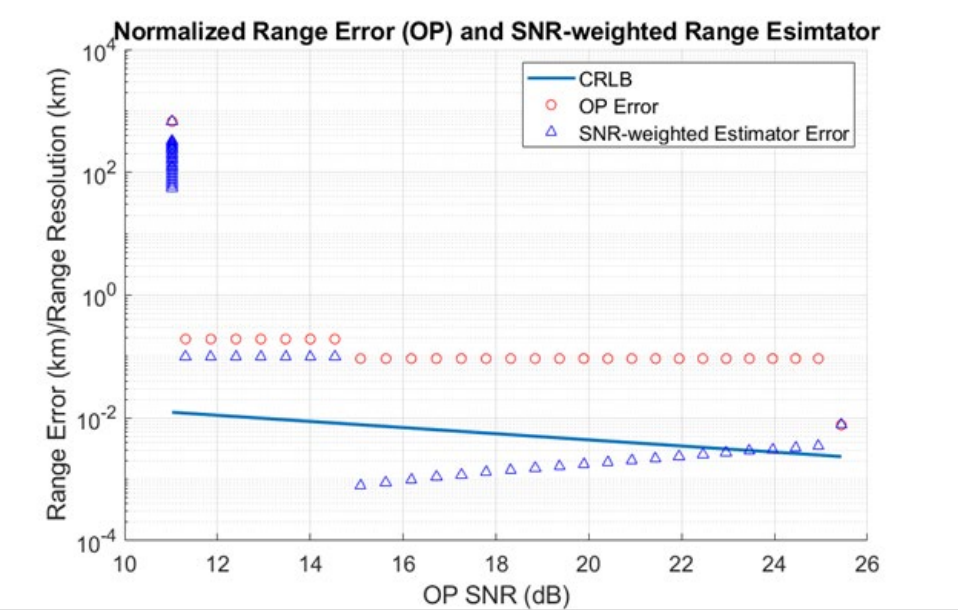

Figure H-6. Normalized range error in the OP channel, and the SNR-weighted estimator normalized range error.

Consider the performance of the SNR-weighted range estimator against the PP channel range estimate in Figure H-7. As was done in Figure H-6, the CRLB for just the PP channel is included in the plot. As observed for the OP channel, if the OP channel SNR is high enough, the SNR-weighted range estimator provides at least as good, and in many instances, better estimates for the range than the PP channel alone. Once the SNR in the OP channel is approximately 14.5 dB, there is no added benefit provided by the OP channel – though this statement is dependent on the PP channel SNR of approximately 24.9 dB. When the OP channel SNR falls below approximately 11.3 dB, including the OP channel degrades the overall range estimate. However, for Goldstone operations, the radar data analysts at JPL reject all detections from either the PP or OP channels if the SNR for a detection falls below 11.76 dB in that respective channel [23], therefore degradation of the overall range estimate due to low SNR in the OP channel will not occur.

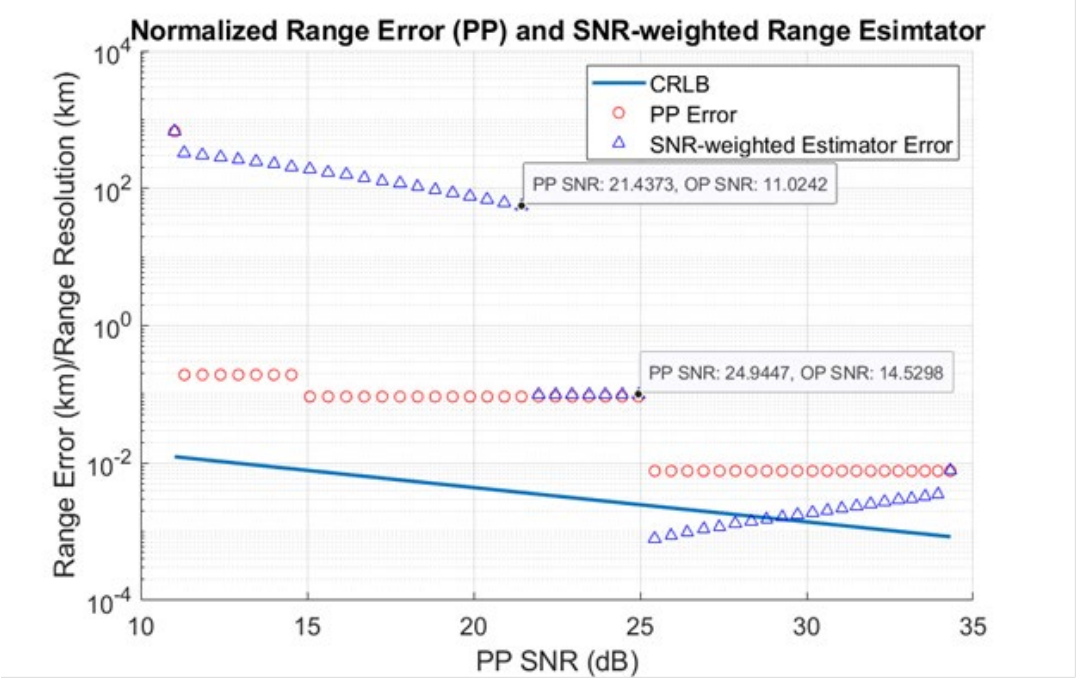

Figure H-7. Normalized range error in the PP channel, and the SNR-weighted estimator normalized range error.